

1-1-2003

Operation and modeling of a thermally-ballasted gasification system

Keith Richard Cummer
Iowa State University

Follow this and additional works at: <https://lib.dr.iastate.edu/rtd>

Recommended Citation

Cummer, Keith Richard, "Operation and modeling of a thermally-ballasted gasification system" (2003).
Retrospective Theses and Dissertations. 19937.
<https://lib.dr.iastate.edu/rtd/19937>

This Thesis is brought to you for free and open access by the Iowa State University Capstones, Theses and Dissertations at Iowa State University Digital Repository. It has been accepted for inclusion in Retrospective Theses and Dissertations by an authorized administrator of Iowa State University Digital Repository. For more information, please contact digirep@iastate.edu.

Operation and modeling of a thermally-ballasted gasification system

by

Keith Richard Cummer

A thesis submitted to the graduate faculty
in partial fulfillment of the requirements for the degree of
MASTER OF SCIENCE

Major: Mechanical Engineering

Program of Study Committee:
Robert C. Brown, Major Professor
Steven J. Hoff
Ron Nelson

Iowa State University

Ames, Iowa

2003

Graduate College
Iowa State University

This is to certify that the master's thesis of

Keith Richard Cummer

has met the thesis requirements of Iowa State University

✓ ✓

Signatures have been redacted for privacy

TABLE OF CONTENTS

LIST OF FIGURES.....	v
LIST OF TABLES.....	vii
ACKNOWLEDGEMENTS.....	viii
ABSTRACT.....	ix
1. INTRODUCTION.....	1
1.1. Statement of problem.....	1
1.2. Research objective.....	3
2. BACKGROUND.....	4
2.1. Hydrogen energy and hydrogen production processes.....	4
2.2. Biomass conversion processes.....	6
2.3. Gasification principles.....	9
2.3.1. History of gasification.....	9
2.3.2. Gasification reactions.....	10
2.3.3. Gasification reactors.....	11
2.4. Indirectly heated pyrolytic gasification.....	13
2.5. Ideal thermally-ballasted behavior.....	15
2.6. Previous ballasted gasification modeling.....	20
3. MODEL FORMULATION AND EXPERIMENTAL METHODS.....	22
3.1. Model formulation.....	22
3.1.1. Model assumptions.....	22
3.1.2. Lumped Capacitance model.....	23
3.1.3. Receding Interface model.....	27
3.2. Experimental methods.....	32
3.2.1. Experimental equipment.....	32
3.2.1.1. Fluidized bed reactor.....	32
3.2.1.2. Latent heat ballast.....	35
3.2.1.3. Fuel feeding system.....	36
3.2.1.4. Data acquisition and control system.....	39
3.2.1.5. Gas sampling and analysis system.....	40
3.2.2. Experimental procedures.....	42
4. RESULTS AND DISCUSSION.....	44
4.1. Validation of the Receding Interface model.....	44
4.2. Sensitivity analysis.....	46
4.2.1. Thermal conductivity of the external blanket insulation.....	46
4.2.2. Volumetric flowrate of the nitrogen purge gas.....	48
4.2.3. Inlet temperature of the cooling steam.....	49
4.2.4. Mass of phase-change material per tube.....	53
4.2.5. Thermal conductivity of lithium fluoride.....	54
4.2.6. Characteristic length of the ballast.....	56
4.2.7. Potential enhancement of the thermal ballast.....	58
4.3. Experimental results.....	60
4.3.1. Reactor cooling time and cooling temperature profiles.....	61

4.3.1.1. Steam cooling tests.....	62
4.3.1.2. Pyrolysis tests.....	65
4.3.2. Combustion temperature profiles.....	66
4.3.3. Gas composition.....	68
4.3.4. System efficiency considerations.....	73
5. CONCLUSIONS AND RECOMMENDATIONS FOR FUTURE STUDY.....	81
5.1. Conclusions.....	81
5.2. Recommendations for future study and process improvement.....	82
APPENDIX A: BALLASTED GASIFICATION MODEL CODE.....	84
APPENDIX B: CALCULATION OF H₂ ANALYZER INTERFERENCE.....	97
APPENDIX C: PREDICTION OF INTERNAL PRESSURES IN LiF BALLAST TUBE..	98
REFERENCES.....	101

LIST OF FIGURES

Figure 2.1—Operating regimes of combustion, gasification and pyrolysis.....	7
Figure 2.2—Diagram of downdraft gasifier (left) and updraft gasifier (right).....	12
Figure 2.3—Schematic diagram of a fluidized bed gasifier.....	12
Figure 2.4—Schematic of the Battelle/FERCO biomass gasification process.....	15
Figure 2.5—Ideal ballasted behavior.....	18
Figure 3.1—Ballasted gasification nodal network.....	24
Figure 3.2—Illustration of Receding Interface model applied to the ballast tubes.....	28
Figure 3.3—Schematic of the biomass gasification system.....	33
Figure 3.4—Gasification reactor.....	34
Figure 3.5—Ballast tubes prior to their insertion into the reactor.....	37
Figure 3.6—Layout of the ballast tubes within the reactor (top view).....	37
Figure 3.7—Temperature profile during ballasted gasification illustrating control strategy.....	43
Figure 4.1—Average bed temperature during steam cooling (no ballast present).....	45
Figure 4.2—Average bed temperature during steam cooling (ballast present).....	45
Figure 4.3—Bed temperature profiles for varied values of k_{ins}	48
Figure 4.4—Reactor cooling time as a function of k_{ins}	49
Figure 4.5—Bed temperature profiles for varied values of \dot{V}_{N_2}	50
Figure 4.6—Reactor cooling time as a function of \dot{V}_{N_2}	50
Figure 4.7—Bed temperature profiles for varied values of T_{steam}	51
Figure 4.8—Variation in reactor cooling time as a function of T_{steam}	52
Figure 4.9—Bed temperature profiles for varied values of m_{pc}	54
Figure 4.10—Variation in reactor cooling time as a function of m_{pc}	55
Figure 4.11—Bed temperature profiles for varied values of k_{LiF}	56
Figure 4.12—Bed temperature profiles for varied values of L_c	58
Figure 4.13—Comparison of current and lengthened ballast tube design.....	59
Figure 4.14—Comparison of honeycomb ballast and tube ballast.....	60
Figure 4.15—Illustration of biomass mixing zone within fluidized bed.....	61
Figure 4.16—Bed temperature profiles during steam cooling for various steam flowrates.....	62

Figure 4.17—Bed temperature profiles during steam cooling tests (flowrate = 81.8 kg/hr).....	63
Figure 4.18—Bed temperature profiles during steam cooling tests (flowrate = 90.9 kg/hr).....	64
Figure 4.19—Bed temperature profiles during steam cooling tests (flowrate = 100.0 kg/hr).....	64
Figure 4.20—Bed temperature profiles during pyrolysis phase of ballasted gasification.....	65
Figure 4.21—Bed temperature profiles during combustion phase of steam cooling tests.....	67
Figure 4.22—Bed temperature profiles during combustion phase of ballasted gasification.....	67
Figure 4.23—Bed temperature profiles illustrating phase-change during combustion.....	68
Figure 4.24—Raw gas composition as determined by CEM's during pyrolysis testing.....	69
Figure 4.25—Raw gas composition as determined by CEM's during cycle #4.....	70
Figure 4.26—Cycle #4 CEM data with selected Micro-GC data superimposed.....	71
Figure 4.27—Composite of Micro-GC data during pyrolysis testing.....	72
Figure 4.28—Composite of Micro-GC data during pyrolysis phase (adjusted to 0% N ₂).....	73
Figure 4.29—Average bed temperature and inlet temperature during steam cooling cycle.....	76
Figure 4.30—Average bed temperature and inlet temperature during ballasted gasification.....	77

LIST OF TABLES

Table 2.1—Fuel gas classifications, sources and energy contents.....	8
Table 2.2—Selected gasification-pyrolysis formation reactions at 1 atm.....	11
Table 3.1—Significant properties of lithium fluoride.....	36
Table 3.2—Energy stored as the bed temperature is raised from 922 K to 1172 K.....	37
Table 3.3—Proximate analysis and heating value of a biomass feedstock (dry basis).....	38
Table 3.4—Ultimate analysis of a biomass feedstock (as received).....	38
Table 3.5—Calibration gases used to calibrate Micro-GC.....	41
Table 3.6—Phase-switching control strategy during pyrolysis testing.....	43
Table 4.1—Parameters examined in sensitivity analysis of k_{ins}	47
Table 4.2—Parameters examined in sensitivity analysis of L_c	58
Table 4.3—Comparison of gas qualities for raw gas and gas adjusted to 0% N ₂	72
Table 4.4—Comparison of ballasted gasification cycle times.....	74
Table 4.5—Comparison of the fraction of fuel pyrolyzed.....	74
Table 4.6—Refractory and insulation thicknesses of previous and present reactors.....	74
Table 4.7—Thermal mass of the walls of the previous and present reactors.....	75
Table 4.8—Comparison of enthalpy of combustion for varying air inlet temperatures.....	77

ACKNOWLEDGEMENTS

The completion of this study was made possible by the efforts of many people. First, I would like to thank Dr. Robert Brown for his guidance and encouragement throughout my time at Iowa State. This opportunity has given me the chance to explore ideas and processes that were unique and exciting. I would like to thank Andy Suby and Jerod Smeenk for their tireless efforts and valuable counsel. They were always there to keep me on target, and I am extremely indebted. Jim Pollard, whose experience and expertise are immeasurable, was vital to the success of this project—thanks, Jim. I would like to thank my fellow graduate students, particularly Dave Falkowski and Daren Daugaard, who have served as my sounding boards and provided sound advice during my graduate experience. I also want to thank Nate Brown for all of his efforts to make the experimental portion of this work successful. I must also say thank you to Diane Love and Tonia McCarley, whose efforts and hard work behind the scenes make all this research possible. Finally, thanks to Dr. Steven Hoff and Dr. Ron Nelson for serving on my POS committee.

In addition to these people, I want to say a special thank you to my parents, Bob and Donna Cummer, who have supported me in every phase of my life, and without whom I would not have completed this journey.

ABSTRACT

The purpose of this study is to characterize the heat transfer and chemical processes that occur within the reactor of an indirectly-heated biomass gasification process. As opposed to conventional gasification processes, in which combustion and pyrolysis reactions occur simultaneously within the reactor, combustion and pyrolysis reactions occur sequentially in a cyclic fashion. The key to this system is employment of a thermal energy storage system. The thermal energy system, called a thermal ballast, is composed of lithium fluoride, a phase-change material, stored within stainless steel tubes. During the combustion process, thermal energy is stored as latent heat of the phase-change material, while this energy is released during the pyrolysis process to drive the endothermic reactions. The composition of the product gases varies throughout the process, however. Previous experiments were unable to resolve these changes in composition throughout the gasification cycle. Through the use of continuous emission monitors, experiments were conducted to quantify the composition of the product gases in this study. In addition to the experiments conducted, a previous model of the gasification process was modified to account for temperature gradients that arise in the thermal ballast tubes during the phase-change process. Following the modification of the model, sensitivity analyses were performed to identify the most significant parameters of the system. Recommendations for process improvement based on these analyses have been included.

1. INTRODUCTION

Man's mind, once stretched by a new idea, never regains its original dimensions.

—Oliver Wendell Holmes

1.1 Statement of problem

At the beginning of a new century, the world's energy demands continue to escalate at ever-increasing rates. Fossil fuels, such as coal, oil and natural gas, fueled the amazing technological and economic advances of the twentieth century. However, it is widely recognized that the use of these resources are detrimental to local and global ecologies. Around the world, concerns regarding potential global warming led to the development of the Kyoto Protocol, which challenged every country to reduce their levels of "greenhouse gas" emissions, released primarily through the consumption of hydrocarbon fuels. Many still debate whether the Greenhouse Effect and global warming are anything more than unsubstantiated theories, but there is no doubt that emissions from power plants, factories and automobiles (such as carbon dioxide, nitrogen oxides and sulfur species) do pollute [1-3]. Air quality issues such as smog, acid rain and high particulate matter concentrations plague many metropolitan areas, where demands for energy and automotive transportation are highest. The only way to remedy these issues is to substantially reduce the consumption of hydrocarbon fuels.

Even if environmental impacts of hydrocarbon fuels are not considered, the reserves and deposits are finite. While substantial amounts of coal, oil and natural gas remain, they are gradually dwindling. These resources will be unable to provide a safe, secure, economical energy in the coming years. Geologist Kenneth S. Deffeyes predicts world oil production will peak between 2003 and 2009 [4]. Deffeyes admits that his methods are just as speculative as any other estimates of world reserves, but regardless of which estimates are most accurate, oil will become more scarce and more expensive sometime during the next fifty years. Natural gas reserves, often found with or near oil reserves, are also likely to diminish, leaving coal, the dirtiest of conventional energy sources, as the only plentiful fossil fuel.

As developing countries around the world are progressing toward full-scale industrialization and greater energy requirements, post-industrial nations in North America and Europe are also increasing their consumption of natural resources. According to recent U.S. Department of Energy projections, total worldwide energy demand is expected to increase sixty percent over the next twenty years. Of this increase, sixty percent is attributable to developing

countries, while industrialized nations and the former Communist Bloc will account for thirty percent and ten percent, respectively [5].

The solutions to these problems require the integration of several emerging concepts and technologies, including hydrogen production processes and fuel cell systems. Fuel cells operated with pure hydrogen fuel emit only water and produce high-quality power. These devices have the potential to alleviate a great portion of the world's dependence on fossil fuels and provide the basis for a hydrogen-based energy economy. A large-scale demonstration of the potential of hydrogen systems is currently underway in Iceland. The island nation, which has a wealth of geothermal and hydroelectric resources, has developed a five-step plan with leading industrial partners, including DaimlerChrysler, Shell International and Norsk Hydro. The goal of the project is to gradually convert all buses, automobiles and the sizable Icelandic fishing fleet to fuel cell-powered systems and develop the corresponding hydrogen infrastructure [6]. If these goals are accomplished, Iceland will have the world's first true, full-scale hydrogen economy.

In order to achieve widespread application of fuel cell technology, methods must be developed that can produce the considerable quantities of hydrogen required. A variety of methods will be required to produce hydrogen in order to minimize environmental impacts and take advantage of every region's indigenous resources. Solar, wind, hydroelectric and geothermal sources can be harnessed to generate hydrogen. Another means of producing hydrogen from renewable resources is the thermal conversion of biomass, or gasification.

Currently, the most common method of biomass gasification is fluidized bed gasification. Conventional air-blown fluidized bed gasification employs a partial combustion process to provide the necessary process heat required for the endothermic gasification reactions. In this process, the producer gas, which contains hydrogen, carbon monoxide and other light gases, is generated simultaneously with the products of combustion. These products of combustion, including nitrogen from the air, dilute the producer gas, lowering the hydrogen content and the heating value. If an alternative energy source rather than partial combustion is utilized to drive the gasification reaction, steam can replace air as the fluidization medium, eliminating the dilution due to products of combustion.

One means of providing the required energy to convert biomass into gaseous products, including hydrogen, is known as thermally-ballasted gasification [7, 8]. The key to this concept is the placement of a thermal energy storage system within the reactor, also referred to as a thermal ballast. In ballasted gasification, combustion and gasification occur sequentially rather than simultaneously. Thermal energy is stored in the ballast as latent heat of a phase-change material during the exothermic combustion process, while the ballast releases this energy to drive

the endothermic gasification process. At the conclusion of the gasification process, the combustion process is repeated. Therefore, ballasted gasification is a cyclic process. During gasification, the flow of oxygen to the reactor is halted. When gasification occurs in the absence of oxygen, the process is termed pyrolysis. Thus, the ballasted gasification cycle is comprised of two phases: the combustion phase and the pyrolysis phase.

The behavior of ballasted gasification systems have been examined and modeled in two previous investigations [7, 8]. In the latter case, experiments were conducted to obtain reactor temperature profiles through the pyrolysis phase and average composition of the product gases during pyrolysis. This composition was determined by a gas chromatograph (GC) and an infrared (IR) spectrometer [8]. Because pyrolysis occurs as the reactor cools, however, the temperature-dependent chemistry is altered, and the gas composition varies throughout the process. Therefore, the average composition of the gases does not effectively describe the products of pyrolysis. In addition to the experimental research, a heat transfer model was developed to predict reactor temperature profiles throughout the pyrolysis phase [8]. This model was effective in the determination of reactor temperature profiles throughout much of the pyrolysis phase, but was unable to accurately predict the temperature profile of the reactor during the phase-change process.

1.2 Research objective

The objective of this research is to examine and characterize the dynamic processes associated with latent-heat ballasted gasification. This is accomplished in two stages. The first of these is the modification of the previous model to better describe the heat transfer processes that occur during the phase-change period of the pyrolysis phase. Following this modification, the model is used to identify key parameters of the heat transfer processes to optimize cycle efficiency. The second stage consists of the execution of experiments to identify the changes in gas composition through the pyrolysis phase. Continuous emission monitors are used to quantify the dynamic processes with supplemental data provided by a Micro-GC.

This thesis describes the nature of both the thermal and chemical processes that occur throughout the thermally-ballasted gasification cycle. A heat transfer model of the pyrolysis phase has been refined, and experimental data has been collected to verify the model and provide insight into the dynamic chemical processes. Based on model results, recommendations to improve systems performance are presented.

2. BACKGROUND

A shift toward renewable resources will require the application of many new energy concepts. Like any new product entering an established market, hydrogen energy systems face a number of challenges, as national energy policies currently favor the traditional energy sources: coal, oil and natural gas. Even if these hydrogen energy concepts are not competitive on the national scale, they provide an opportunity on the small scale to supply inexpensive, high-quality power. The application of these processes requires an understanding of basic hydrogen energy concepts, and, in the case of biomass-derived hydrogen processes, biomass gasification fundamentals.

2.1 Hydrogen energy and hydrogen production processes

In 1811, William Nicholson and Sir Anthony Carlisle discovered that the hydrogen and oxygen atoms that comprise a water molecule could be dissociated by passing an electrical current through the molecule. This process eventually became known as the electrolysis of water. After experimenting with electrolysis, William Grove, an English physicist, hypothesized that recombining hydrogen and oxygen would produce an electrical current. Grove built what he termed a “gaseous voltaic battery” in 1839, generating a small current. He made improvements to his system, but was unable to develop his “battery” as a practical energy source. In 1889, Ludwig Mond and Charles Langer adapted Grove’s “gaseous battery” to produce electricity by supplying coal gas and air. Mond and Langer called their device a fuel cell. Approximately fifty years later, the modern fuel cell was developed by Francis T. Bacon, a descendant of the seventeenth-century philosopher and scientist, and his design served as the basis for the on-board power generation systems used on the Mercury and Apollo spacecrafts [9]. Today, fuel cells have been proposed and developed for a variety of applications, from supplying energy for small portable electronic devices such as cellular phones to large stationary power applications, with ratings in excess of 2.5 MW. Fuel cells stand poised to become the key component of a potential hydrogen-based energy infrastructure.

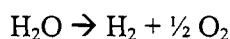
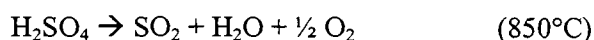
Despite the technical barriers that still must be overcome, hydrogen-based energy systems have advanced to the point that serious consideration must be given to the potential methods of producing hydrogen on a large scale. Currently, most hydrogen produced is derived from hydrocarbon sources, often natural gas, reformed with steam. Several processes exist which produce hydrogen by the electrolysis of water; the requisite electricity can be supplied by traditional fossil fuel power plants, or generated from renewable sources such as solar, wind and

geothermal energy; hydroelectric sources; and biomass. Substantial research has also been conducted investigating thermochemical processes, which involve a series of chemical reactions that sum to the dissociation of water into hydrogen and oxygen, and biological processes, which take advantage of certain microorganisms' ability to process gases into hydrogen.

Steam reforming of methane and other organic species is a well-established process in the petrochemical industry [11]. The products of this process are almost completely carbon dioxide (CO₂), carbon monoxide (CO) and hydrogen (H₂). Additional hydrogen is produced via the water-gas shift reaction, by which carbon monoxide and steam react to form carbon dioxide and hydrogen [11, 12]. In the case of natural gas reforming, a pre-treatment step occurs to remove any sulfur that may be present in the gas. While the reforming process is relatively simple, a great deal of carbon dioxide is produced as a byproduct. There are methods to mitigate the potential effects of this carbon dioxide production. For example, researchers in Norway have investigated sequestering the carbon dioxide and have also developed a method of pyrolyzing natural gas, producing only hydrogen and carbon black [13].

Efforts to harness the energy of solar radiation and the kinetic energy of the wind have been underway since the 1970s [14]. Solar collectors and wind turbines currently have the potential to efficiently produce electricity. However, these processes are unable to supply power continuously, and thus, a method of energy storage must be devised to bridge the intermittent supply with demand. The solution to this problem has been to utilize the electricity generated by solar and wind generators to drive an electrolysis process [15, 16]. Thus, the development of methods to produce hydrogen from these resources is relatively complete.

Thermochemical hydrogen production processes were developed as a result of a United States Army project, called the Energy Depot, which attempted to identify a method of producing fuels from earth, air or water [17]. It was recognized that thermolysis, or splitting water into hydrogen and oxygen by heating the water to extremely high temperatures, was impractical. The required temperature to efficiently achieve hydrolysis is 2500°C [18]. However, it has been shown that using intermediary elements and multiple reactions decreases the energy requirements [17]. By choosing the proper intermediaries and reactions, a thermal water-splitting cycle can be achieved. One such cycle is the General Atomic Sulfur-Iodine process [19], which is described as follows:



The process temperature requirements of the General Atomic Sulfur-Iodine cycle are much lower than direct thermolysis. The temperatures required are fairly compatible with the waste heat streams from a nuclear reactor, and researchers claim efficiencies near 60% are possible for systems co-generating hydrogen and electricity [20].

Efforts to utilize microorganisms to produce hydrogen have increased in the last decade. These microorganisms generally produce hydrogen through one of two processes, photosynthesis or fermentation. These biological processes are more environmentally-friendly and less energy intensive than methods mentioned above [21]. One example of the production of hydrogen by a biological microorganism is the bacteria *Rubrivivax gelatinosus* CBS2, which is able to convert carbon monoxide into hydrogen and carbon dioxide (the water-gas shift process). Under the proper conditions, this organism was able to convert 80% of the carbon monoxide in its environment into hydrogen [22].

The production of hydrogen from biomass is achieved primarily through gasification processes [23], which will be discussed in detail in the following section. An investigation of hydrogen production from biomass showed that increasing temperatures resulted in increasing hydrogen yield, but the variable with the greatest influence was equivalence ratio [24]. As less oxygen was present in the reactor, the hydrogen yield significantly increased, with hydrogen content greater than 40% of the total gas. This suggests that steam gasification would provide greater hydrogen yields than conventional air-blown gasification. Additional research showed that hydrogen content could be further increased to levels near 60% by including a catalytic tar cracking process following the steam gasification system [25].

2.2 Biomass conversion processes

Although biomass-derived energy currently constitutes an extremely small portion of the total energy consumed in the United States, this resource represents 14% of the world's energy. In developing countries, biomass provides approximately 35% of the energy consumed [23]. There is potential to increase the use of biomass in this country, especially in the midwestern United States, as there is an abundance of agricultural wastes in the region such as corn stover and oat hulls as well as the ability to develop crops specifically for energy production, such as switchgrass [26]. The conversion of biomass into a valuable energy source is accomplished via one of three processes: combustion, gasification or pyrolysis.

Combustion, gasification and pyrolysis are thermochemical conversion processes. That is, these processes alter the chemical composition of the fuels, which depending on the process, may be further utilized. All three of the processes can occur in a given reactor, but the factor that

determines which process proceeds is the equivalence ratio. The equivalence ratio, ER , is defined according to the following equation:

$$ER = \frac{AF_{actual}}{AF_{stoich}}, \quad (2.1)$$

where AF_{actual} and AF_{stoich} are actual and stoichiometric air-to-fuel ratios, respectively. At an equivalence ratio of one, complete combustion should occur, while at a equivalence ratio of zero, no oxygen is introduced into the reactor, and the process is termed pyrolysis. Gasification occurs between these cases [27]. The adiabatic reaction temperatures of the modes of thermochemical conversion of biomass are shown as a function of equivalence ratio in Figure 2.1. This figure also defines the regimes in which combustion, gasification and pyrolysis occur.

Combustion is defined as the complete oxidation of fuel, releasing heat as its useful product. This heat can either be used directly or transferred to a working fluid [8]. An example of a direct use of this heat is the application of process heat to dry grain, while the combustion of coal provides thermal energy to raise the steam required to drive turbines in conventional coal-

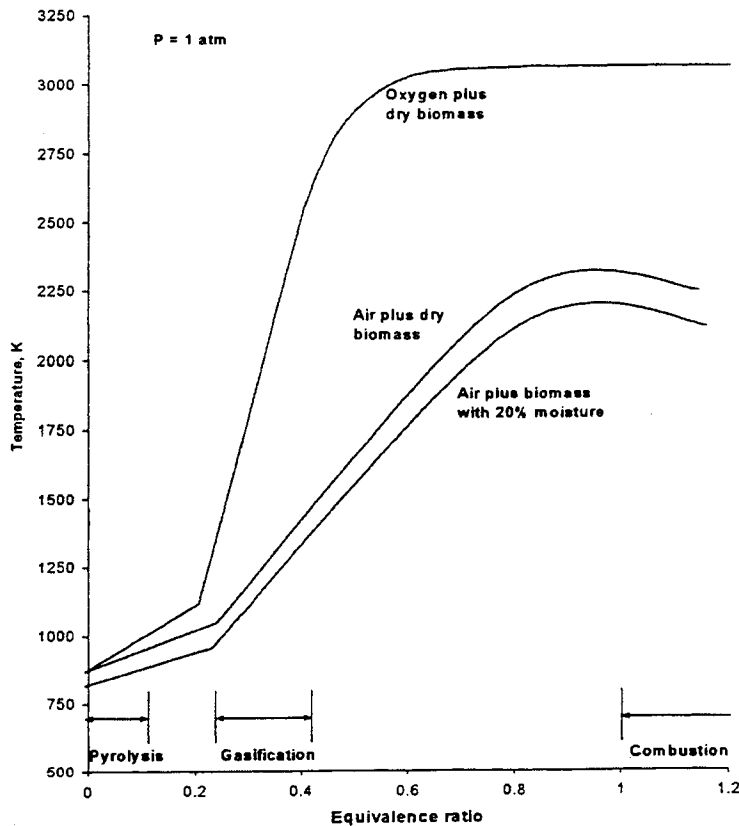


Figure 2.1—Operating regimes of combustion, gasification and pyrolysis [27]

fired power plants. The predominant products of combustion are carbon dioxide and water, although gaseous hydrocarbons, particulate and ash are usually produced as well.

Pyrolysis is the thermochemical conversion of a material in the absence of oxygen. Pyrolysis processes generally fall within one of three categories: slow pyrolysis, fast pyrolysis or flash pyrolysis. In slow pyrolysis, the rates at which the fuel is heated is low, generally less than 10°C/s. Temperatures are generally lower than 500°C, and the residence time of the gas exceeds five seconds. The predominant products of slow pyrolysis are char and tar. During fast pyrolysis, the temperatures are elevated in excess of 600°C, gas residence times are reduced to less than half a second, and the heating rates increase to 10-100,000°C/s. The primary products of fast pyrolysis are gaseous products rather than char and tar. Flash pyrolysis processes have the high heating rates of fast pyrolysis, but have operating temperatures nearer to those of slow pyrolysis, approximately 400-600°C. The residence time of the fuel is roughly 2 seconds, with products of liquid tar and oils [28]. The gaseous products of fast pyrolysis are considered to be a medium energy gas, with heating values between 11,000 kJ/m³ (300 Btu/ft³) and 19,000 kJ/m³ (500 Btu/ft³) [8]. The heating values of a variety of processes are shown in Table 2.1.

Gasification is defined as “a thermal process which involves the heating of a feedstock by partially combusting it with less than the necessary stoichiometric air requirement and driving off the combustible volatiles” [29]. Thus, gasification is a combination of combustion and pyrolysis. The stoichiometric ratio of oxygen to biomass is typically 0.3 for gasification reactions [30]. When air is used to provide the required oxygen for gasification, the process is termed air-blown gasification.

Table 2.1—Fuel gas classifications, sources and energy contents [27]

Name	Source	Energy range	
		kJ/m ³	Btu/ft ³
Low energy gas (LEG) (producer gas)	Blast furnace, water gas process	3,000-3,700	80-100
Low energy gas (LEG) (generator gas)	Air gasification	5,600-7,500	150-200
Medium energy gas (MEG) (producer gas)	Oxygen or indirectly- heated gasification	11,000-19,000	300-500
Biogas	Anaerobic digestion	22,000-26,000	600-700
High energy gas (HEG) (Natural gas)	Oil/gas wells	37,000	1,000
Synthetic natural gas (SNG)	Further processing of MEG and biogas	37,000	1,000

Gasification takes place in two stages, volatilization and char burning. Volatilization is the release of organic species from the fuel, or feedstock, and char burning is the combustion of the remaining solids following the release of the gases. Most of the gases are produced during the volatilization stage, while the char burning stage produces the heat to perpetuate the gasification process [29]. The reactions that occur during gasification are described in Section 2.3.2.

The resulting products of air-blown gasification, termed producer gases, have a relatively low heating value, approximately 5,600-7,500 kJ/m³ (150-200 Btu/ft³), or 15-20% that of natural gas [27]. The low heating value of the gas is primarily due to the dilution of the gas by the products of the combustion process. These products include the nitrogen that comprises the majority of the air used to partially oxidize the feedstock.

2.3 Gasification principles

2.3.1 History of gasification

The history of gasification can be traced back to eighteenth-century England, where the process was first used to produce combustible gases from coal. British engineer William Murdock is credited with the invention of the first coal gas production process in 1792, first lighting his home and eventually lighting a large cotton mill in Manchester [31]. The use of coal gas spread across the Atlantic, and the first United States patent for a gas production process was granted in 1813 to Newport, Rhode Island, inventor David Melville. Melville produced gas in a backyard plant and began providing gas to local factories for lighting. In 1816 Baltimore artist Rembrandt Peale used coal gas to provide light during an exhibit at his gallery. The public marveled at the new lighting technology, and Peale organized a group of investors to charter the first gas company in the United States, the Gas Light Company of Baltimore. Originally used only for lighting homes and streets, mills and factories were quick to discover the potential of gas-powered engines that drove many nineteenth-century industrial processes. By 1859, almost three hundred manufactured gas companies operated “gas works” within the United States, providing gas to a wide variety of customers [32].

Early methods of producing coal gas consisted of placing coal in anaerobic vessels called retorts. When the retorts were heated, the volatile components of the coal were released, leaving the retort as a gas. This volatile-derived gas represented approximately forty percent of the coal’s original mass, leaving sixty percent of the original mass as coke. The volatile vapors were then drawn into another vessel known as the hydraulic main. A portion of the vapors condensed in the hydraulic main, forming liquors, combinations of coal tar and water. The vapors leaving the

hydraulic main were coal gas. The coal gas was passed through a condenser to remove additional tars. Additional steps were used to remove ammonia and sulfur species, and the gas was stored for use [32].

A major improvement was made in gas production when a Pennsylvanian professor named Lowe developed the carbureted water gas process in 1875, increasing the caloric value of the gas to 300-350 Btu per cubic foot (approximately thirty percent of the value of natural gas). A volatile gas was produced in the presence of steam in the generator. The vapors were then directed to a carburetor, where oils were mixed with the coal vapors, and then through a superheater, where the oils thermally cracked into light gases [32]. Thus, the carbureted process produced a gas comprised of coal and oil vapors.

Following the emergence of electricity and natural gas, gas works began to disappear from the American landscape. The last utility gas manufacturer ceased operation in 1966, although some factories continued to use on-site gasifiers to produce gas for industrial processes [33]. Even if these processes could have competed with electricity and natural gas, it was recognized that these processes took a tremendous toll on their local environments due to the production of cokes, tars and sludges. Many former gas works became Environmental Superfund sites, with cleanup continuing today.

Gasification technologies lay dormant for decades until the energy crises during the 1970s provided the impetus for their revival. The gasification of coal and, subsequently, biomass was investigated throughout the 1980s and 1990s. The result of this research was the development of a wide range of fluidized bed gasification processes, including fluidized bed biomass gasification.

2.3.2 *Gasification reactions*

Multiple reactions occur within the reactor during the gasification process. These reactions are varied and complex. For conventional gasification in which partial combustion of the fuel drives the pyrolysis reactions, both exothermic and endothermic reactions occur. It is extremely difficult to determine all of the reactions that occur during the process, but the most significant of these reactions are listed in Table 2.2.

The gas produced during conventional gasification consists of hydrogen, carbon monoxide, methane, carbon dioxide and nitrogen. Typically, hydrogen comprises approximately 6-8 vol-% of the producer gas. In addition to these organic compounds, producer gas also contains tars, alkali and particulate matter, which must be eliminated prior to the use of the product gas for energy production or industrial use. Ideally, the producer gas would largely be

Table 2.2—Selected gasification-pyrolysis formation reactions at 1 atm [34]

Reaction name	Equation	Δh at 298 K (kJ/mol)	Relative rate at 1073 K
Combustion	$C + O_2 \rightarrow CO_2$	-394	10^5
Combustion of CO	$CO + \frac{1}{2} O_2 \rightarrow CO_2$	-110	—
Water-gas	$C + H_2O \rightarrow CO_2 + H_2$	+131	3
Boudouard reaction	$C + CO_2 \rightarrow 2 CO$	+173	1
Methane reaction	$C + 2 H_2 \rightarrow CH_4$	-75	10^{-3}
Water-gas shift	$CO + H_2O \rightarrow CO_2 + H_2$	-41	—

composed of hydrogen and carbon monoxide, with little carbon dioxide and nitrogen. From a hydrogen production standpoint, carbon monoxide is beneficial in that it can be combined with steam to form additional hydrogen and carbon dioxide, by the water-gas shift reaction.

2.3.3 Gasification reactors

Currently, there are three types of gasification reactors that are commonly used for biomass gasification: updraft gasifiers, downdraft gasifiers and fluidized bed gasifiers [35]. Updraft and downdraft gasifiers (see Figure 2.2) are fixed bed reactors, meaning that the bed consists solely of biomass. Updraft gasifiers, also called counter-current or counter-flow gasifiers, are designed so that air or oxygen is directed up through grates into the fixed bed, while the fuel (biomass) falls down toward the bed. The fuel at the bottom of the bed undergoes a combustion process, producing carbon dioxide and water vapor. As these products rise in the reactor, they react with char, forming carbon monoxide and hydrogen gas; this reaction is termed reduction of the char. Near the top of the reactor, these product gases pyrolyze the entering biomass at temperatures between 200-500°C, producing gases and the char necessary for the reduction reactions and then exit the bed [27].

Downdraft gasifiers, also called co-current or co-flow reactors, are designed so that both air and fuel pass down through a moving bed of biomass. These reactors were specifically designed to reduce the amount of tars and oils in the product gases. In these reactors, the product gases do not pass through the pyrolyzing biomass. Instead, the carbon dioxide and water vapor descend with the char from pyrolysis through a reduction zone, where carbon monoxide and hydrogen gas are formed and pyrolysis oils are “cracked,” forming light hydrocarbon vapors. These product gases and hydrocarbon vapors immediately exit the reactor. Product gas from downdraft gasifiers generally contain less than 10% percent of the tars produced in updraft gasifiers.

Fluidized bed gasifiers (see Figure 2.3) contain an inert bed of granular particles, typically sand or limestone, through which a high velocity stream of gas (air, oxygen, steam or

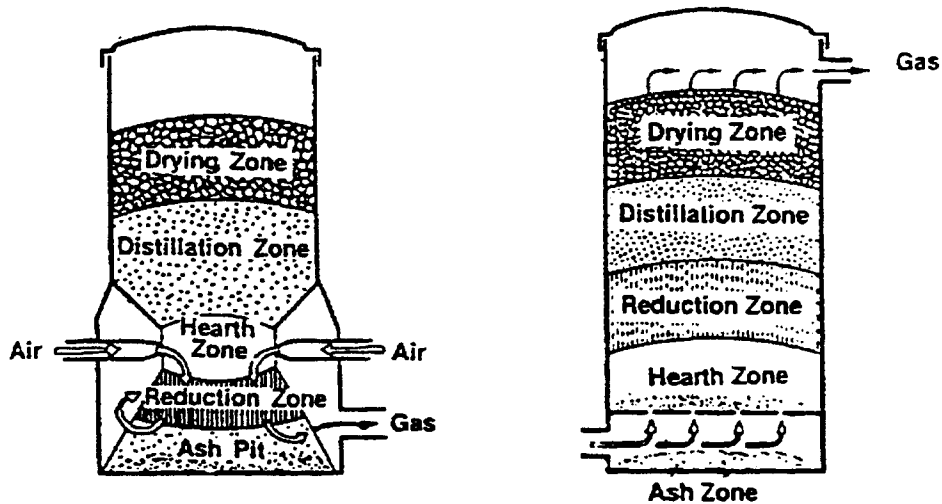


Figure 2.2—Diagram of downdraft gasifier (left) and updraft gasifier (right) [35]

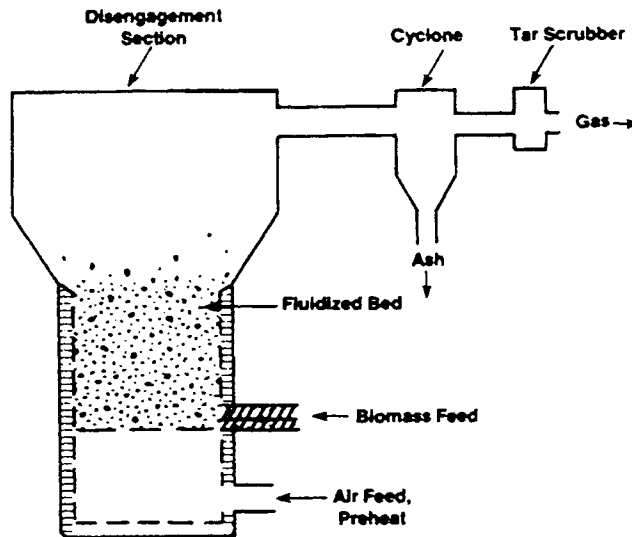


Figure 2.3—Schematic diagram of fluidized bed gasifier [35]

producer gas) is directed. The gas, called the fluidizing medium, suspends the particles, and when the gas passing through the bed achieves a certain velocity, the bed material behaves in a manner resembling that of a boiling fluid. There is a turbulent, churning motion of the bed particles. The bed is said to be “fluidized” at this state, and the minimum gas velocity needed to produce this state is termed the “fluidizing velocity” [29].

Fuel is introduced above or below the bed, and gasification occurs in the bed. The producer gases exhaust above the bed, and there may be char and bed material caught, or entrained, in the flow of the product gases. The product gas and the entrained particles are directed through a cyclone, which separates the particles from the product gas. The product gas is allowed to continue downstream, and the char/bed material is either collected or sent back to the gasifier.

Fluidized bed reactors have many advantages over fixed bed reactors. These beds can be scaled to virtually any size with relative ease and provide excellent fuel flexibility, allowing wide variations in fuel type, size and moisture content. The fluid action of the bed also provides extremely high heat and mass transfer capabilities when compared with fixed bed reactors. This characteristic allows the bed to operate in a manner that is nearly isothermal. Isothermal operation improves product gas quality and reduces the amount of tars. Fluidized bed also allow for the addition of bed additives such as limestone that reduce the chance of bed agglomeration, which is the congealing of the bed [8]. Due to the wide use of fluidized beds for gasification processes, the remainder of this paper will deal with fluidized bed gasification.

2.4 Indirectly-heated gasification

Gasification methods can be separated into two categories: air-blown gasification processes and indirectly-heated gasification processes. In air-blown gasification methods, biomass is partially oxidized by substoichiometric amounts of oxygen to provide energy for thermal conversion of the remaining biomass to gases and organic vapors. In indirectly-heated gasification processes, an external heat source, rather than oxygen-supported combustion, provides the energy for high-temperature gasification of the organic fraction of biomass to vapors and gases. Rather than air (and the corresponding oxygen), steam is often used to fluidize the bed during indirectly-heated gasification. The thermal destruction of organic materials in the absence of oxygen is called pyrolysis, so by definition indirectly-heated gasification is pyrolysis [27].

The actual method of gasification greatly affects the hydrogen content and the heating value, also known as the caloric value, of the producer gas. The heating value is a measure of the energy potential of the gas per unit of standard volume, and is often expressed in MJ/m³ or Btu/ft³. In air-based gasification, air or pure oxygen is used as the fluidizing medium. When air is used as the fluidizing medium (air-blown gasification), the heating value is low, in the range of 4.9-5.9 MJ/m³ (135-160 Btu/ft³). The hydrogen content during air-blown gasification is on the order of 6-8 vol-%. These low values are due to the dilution of the product gas by the nitrogen from the air and products of combustion. During indirectly-heated gasification, this dilution is

eliminated, and hydrogen content exceeds 20 vol-% with heating values in excess of 14.0 MJ/m^3 (380 Btu/ft^3).

Indirectly-heated gasification processes are distinguished by the thermal energy source they use to provide the energy required for pyrolysis to go on. External heat sources such as resistance heaters or burners can be used in this capacity, but these methods are only useful on small, research-scale reactors where system efficiency is irrelevant. Two indirectly heated gasification methods have been commercially developed by MTCI [36] and Battelle Columbus Laboratory [37, 38]. A third method has been developed on a pilot scale at Iowa State University [7, 8].

MTCI has developed a fluidized bed steam reformer to recover energy from two waste streams of the paper industry, mill refuse and black liquor. To supply the required thermal energy, MTCI has developed the Pulse-Enhanced™ indirect heater, which consists of heating tubes immersed within the bed. The tubes pass completely through the bed. This process combusts either natural gas or recycled producer gas, and the flow through the tubes is oscillated, causing turbulent mixing within the tubes, a continuously scrubbed boundary layer, and high rates of heat transfer. A medium energy gas has been observed from this process, with heating values ranging from $12,000$ to $16,500 \text{ kJ/m}^3$ (330 to 450 Btu/ft^3) [36].

An indirect gasification process has been developed by Battelle Laboratories and licensed to Future Energy Resources Corporation (FERCO). Now known as the FERCO SilvaGas Process, the process couples two reactors, one a gasifier and the other a combustor. The gasifier, operating with steam as the fluidizing medium, generates producer gas and char. The char and sand entrained in the flow is separated through a cyclone and sent to the combustor, which combusts the char in order to heat the sand. The hot sand is then sent back to the gasifier to provide heat for the gasification reactor [37]. The system, shown in Figure 2.4, is currently being demonstrated at the McNeil Generating Station in Burlington, Vermont. Heating values of 16.75 MJ/Nm^3 (455 Btu/ft^3) have been achieved with wood as the feedstock. The process has been incorporated into an IGCC system, and the researchers claim electrical efficiencies of 25% [38].

Rather than providing thermal energy from a source external to the fluidized bed, researchers at Iowa State University have developed a means of storing thermal energy within the bed to produce a medium energy gas [7, 8]. The key to this system is a thermal ballast, which is a collection of tubes containing lithium fluoride. Lithium fluoride has a melting point of 1121 K (1560°F) and a high latent heat of fusion. The process operates in two phases: combustion and pyrolysis. During combustion, air is injected into the bed to fluidize the steam and oxidize the

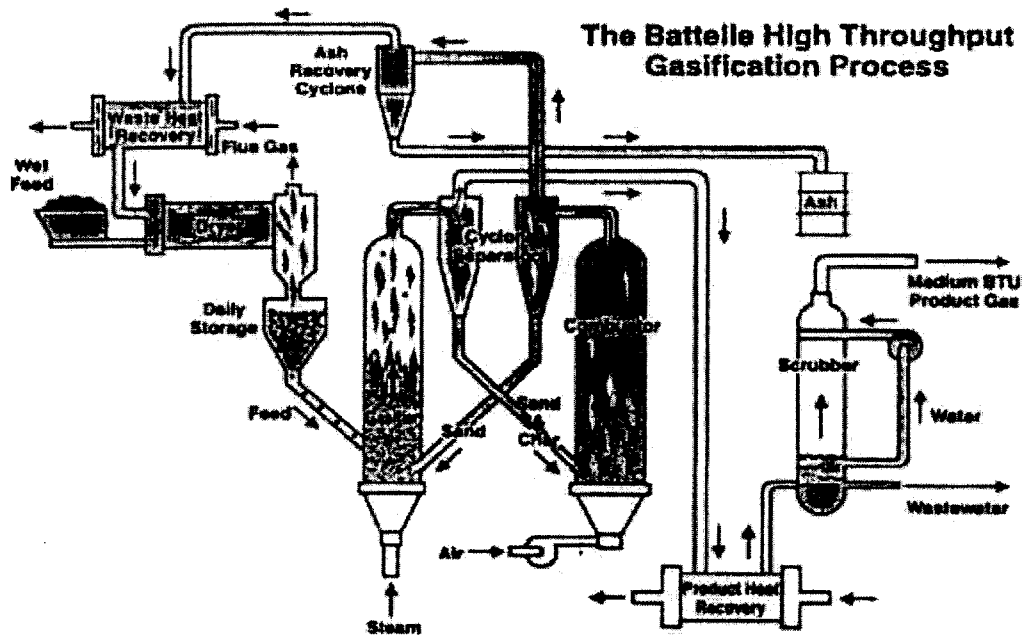


Figure 2.4—Schematic of the SilvaGas biomass gasification process [38]

feedstock. Sensible heat is stored in the sand, and latent heat is stored in the lithium fluoride as it melts. During pyrolysis, the air is removed and steam is used to fluidize the bed. The stored heat is released during pyrolysis as the bed cools and the lithium fluoride solidifies. This process need not suffer wide temperature swings; ideally, this process could operate at very small temperature differences between the combustion and pyrolysis phases.

2.5 Ideal thermally-ballasted behavior

The turbulent mixing seen in fluidized beds (see Section 2.2.3) offers these reactors two distinct advantages. First, this provides spatially-isothermal operation of the bed. More specifically, only very small temperature gradients exist within the bed. This allows a greater amount of reactants to be processed, as gasification (or any other reaction) takes place in nearly all of the bed rather than a small reaction zone. This also leads to a more consistent product of the reaction, as there should not be any dramatic differences in residence time or reaction temperature for a given reaction. The isothermal nature also facilitates the prediction of bed behavior. Second, the heat transfer rates between the fluidized bed and objects immersed within the bed are extremely high, which allows reactions normally limited by heat transfer to be processed very efficiently.

Latent heat storage also provides two important advantages. The first of these advantages is that the change in phase of a homogeneous material occurs at a defined and constant temperature. Thus, a phase change process is a constant temperature (temporally-isothermal) process. The second advantage of latent heat storage is a large amount of energy can be stored in a relatively small volume. These spatial considerations are important for any application, but are especially critical in extremely endothermic processes, such as the pyrolysis of biomass.

Considering the pyrolysis of biomass in a fluidized bed with latent heat storage, the ideal behavior would be spatially-isothermal and nearly temporally-isothermal operation. During the pyrolysis of biomass at a constant bed temperature, the heat transfer rate required for the chemical reactions of pyrolysis is matched by the latent heat transfer rate from the phase-change material to the bed as the phase-change material solidifies. The stored energy of the bed itself, \dot{E}_{bed} , does not change as there is no change in bed temperature, and the First Law of Thermodynamics states:

$$\dot{E}_{bed} = \dot{m}_{biomass} \cdot h_{pyr} + h_{bed-pc} \cdot A_{surf} \cdot (T_{pc} - T_{bed,pyr}) = 0 \quad (2.1)$$

where,

- \dot{E}_{bed} = rate of change of stored energy within the fluidized bed
- $\dot{m}_{biomass}$ = mass flowrate of biomass into the reactor
- h_{pyr} = energy required to complete pyrolysis reactions per unit mass of biomass
- h_{bed-pc} = heat transfer coefficient between fluidized bed and phase-change material
- A_{surf} = surface area of phase-change material
- T_{pc} = phase-change temperature of phase-change material
- $T_{bed,pyr}$ = bed temperature during constant temperature pyrolysis process.

Similarly, during combustion of biomass at a constant bed temperature, the thermal energy released in the bed due to the combustion process is matched by the latent heat transfer from the bed to the phase-change material as the phase-change material melts. Again, the stored energy of the bed does not change, and the First Law holds:

$$\dot{E}_{bed} = \dot{m}_{biomass} \cdot HHV + h_{bed-pc} \cdot A_{surf} \cdot (T_{pc} - T_{bed,comb}) = 0 \quad (2.2)$$

where,

- HHV = higher heating value per unit mass of biomass
- $T_{bed,comb}$ = bed temperature during constant temperature combustion process.

While both pyrolysis and combustion can ideally proceed at a constant temperature, it must be noted that a slight temperature gradient must exist between the fluidized bed and the phase-change material to prompt the transfer of thermal energy. Only an infinitely large heat transfer coefficient between the fluidized bed and the phase-change material, h_{bed-pc} , would allow negligible temperature gradient to exist between the bed and the phase-change material. Requiring a finite value of h_{bed-pc} also requires a non-negligible temperature gradient. The rates of thermal energy transfer from the phase-change material to the fluidized bed during pyrolysis and combustion, $\dot{Q}_{bed,pyr}$ and $\dot{Q}_{bed,comb}$, respectively, are determined by the following equations:

$$\dot{Q}_{bed,pyr} = h_{bed-pc} \cdot A_{surf} \cdot (T_{pc} - T_{bed,pyr}) \quad (2.3)$$

$$\dot{Q}_{bed,comb} = h_{bed-pc} \cdot A_{surf} \cdot (T_{pc} - T_{bed,comb}) \quad (2.4)$$

Establishing the convention that heat transfer into the bed is positive in value while heat transfer out of the bed is negative in value, it is understood that heat transfer during pyrolysis, when the bed absorbs thermal energy from the phase-change material, is positive and heat transfer during combustion, when the bed provides thermal energy to the phase-change material, is negative:

$$\dot{Q}_{bed,pyr} > 0 \quad (2.5)$$

$$\dot{Q}_{bed,comb} < 0 \quad (2.6)$$

From these equations it follows:

$$\dot{Q}_{bed,pyr} > \dot{Q}_{bed,comb} \quad (2.7)$$

$$h_{bed-pc} \cdot A_{surf} \cdot (T_{pc} - T_{bed,pyr}) > h_{bed-pc} \cdot A_{surf} \cdot (T_{pc} - T_{bed,comb}) \quad (2.8)$$

$$T_{bed,pyr} < T_{bed,comb} \quad (2.9)$$

Thus, even though the fluidized bed can ideally operate at a constant temperature during pyrolysis and at a constant temperature during combustion, these two temperatures are not the same, and the bed cannot remain at a constant temperature throughout the entire gasification cycle. From the manipulation of Equation 2.2 and Equation 2.3, the fluidization temperatures during pyrolysis and combustion, respectively, can be shown to be:

$$T_{bed,pyr} = T_{pc} + \frac{\dot{m}_{biomass} \cdot h_{pyr}}{h_{bed-pc} \cdot A_{surf}} \quad (2.10)$$

$$T_{bed,comb} = T_{pc} + \frac{\dot{m}_{biomass} \cdot HHV}{h_{bed-pc} \cdot A_{surf}} \quad (2.11)$$

Following the completion of the pyrolysis phase, which would ideally be marked by the solidification of all of the phase-change material, and the combustion phase begins, there must be a short time during which the combustion process raises the bed temperature from $T_{bed,pyr}$ to $T_{bed,comb}$, as there must be a corresponding period at the beginning of the pyrolysis period in which the bed temperature returns to $T_{bed,pyr}$ following the melting of all of the phase-change material. This behavior is illustrated in Figure 2.5.

The length of time that the fluidized bed would remain at constant temperature during pyrolysis would be determined by the amount of latent heat storage capacity, i.e. the product of the mass of phase-change material contained within the bed and the latent heat of fusion of the material, $m_{pc} \cdot h_{pc,fus}$, and the rate of heat transfer rate required by the pyrolysis of the biomass, i.e. the product of the mass flowrate of biomass and the enthalpy of pyrolysis, $\dot{m}_{biomass} \cdot h_{pyr}$. The maximum time, t_{pyr} , the bed could remain at a constant temperature would be calculated according to the following equation:

$$t_{pyr} = \frac{m_{pc} \cdot h_{pc,fus}}{|\dot{m}_{biomass} \cdot h_{pyr}|} \quad (2.12)$$

while the maximum time the bed could remain at constant temperature during combustion, t_{comb} , would be determined by the latent heat storage capacity of the ballast and the heat energy required to drive the pyrolysis process replaced by the energy production rate of the combustion process, $\dot{m}_{biomass} \cdot HHV$:

$$t_{comb} = \frac{m_{pc} \cdot h_{pc,fus}}{\dot{m}_{biomass} \cdot HHV} \quad (2.13)$$

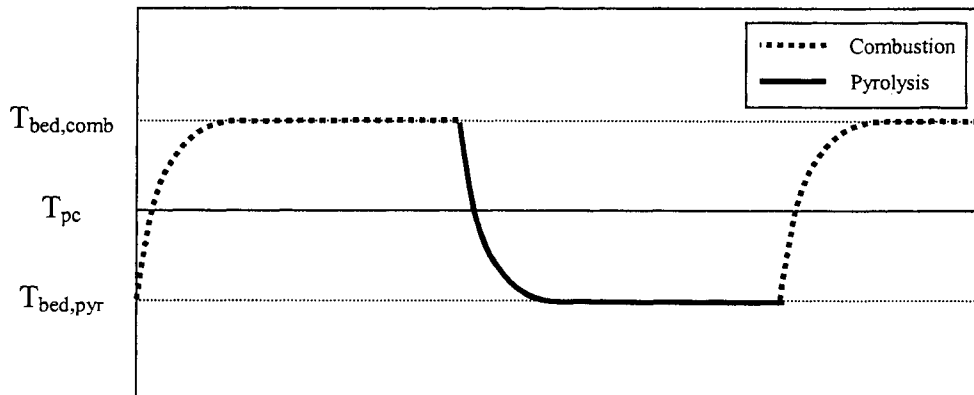


Figure 2.5—Ideal ballasted behavior

These times do not consider the time required to raise the fluidized bed to the appropriate temperatures for constant bed temperature behavior determined above, during which at least a small portion of the phase-change material would either melt or solidify. The extent to which this phase-change would occur would be based upon the heat transfer coefficient between the fluidized bed and phase-change material, h_{bed-pc} .

This treatment does not consider several aspects of ballasted gasification in a fluidized bed that are significant during actual operation. In the idealization, neither temperature gradients nor phase gradients exist within the phase-change material. The material is treated as infinitesimal “packets” circulating within the bed, and the change in phase occurs instantaneously. This is not the case in practical applications as the phase-change material is segregated in some fashion from the fluidized bed. This is usually accomplished by enclosing the phase-change material within tubes or spheres. Within these vessels, both liquid and solid phases of the material exist to some extent, causing temperature gradients within the phase-change material itself. Conduction through the walls of the vessels also plays a very important role in the heat transfer between the phase-change material and the bed.

Another important factor neglected in the previous treatment is the requirement to raise the fluidizing medium, such as air or steam, to the temperature of the bed. This can be a significant heat sink, particularly if the fluidizing medium is not pre-heated prior to its introduction into the bed or the biomass feedrates during combustion and pyrolysis are relatively low. If the fluidizing medium is not pre-heated, a large temperature gradient exists between the medium and the bed, resulting in high heat transfer rates to the fluidizing medium and robbing energy that could be applied to the phase-change material or the pyrolysis process. If the reactor or its ancillary systems are not large enough to accommodate high biomass feedrates, the amounts of time required for pyrolysis and combustion, t_{pyr} and t_{comb} , respectively, are extended, requiring larger quantities of the fluidizing medium to be passed through the bed. From this standpoint, it would be advantageous to operate short ballasted gasification cycles with a fluidizing media pre-heated to the phase-change temperature, T_{pc} , which is the approximate average bed temperature.

Finally, the reactor was considered to be adiabatic in the ideal treatment. This may or may not be the case in actual practice, depending upon the amount of insulation applied to the reactor. The high temperatures required for efficient combustion and gasification (greater than

900 K, or 1200°F) lead to a large potential for heat losses to the environment. Obviously, any such losses should be minimized to the greatest extent possible.

2.6 Previous ballasted gasification modeling

Models of the ballasted gasification process were developed during the work of Oatley [7] and Pletka [8]. Oatley developed a one-dimensional finite difference method to predict the fluidized bed temperature profile as the bed was cooled by a flow of air. The diameter of the fluidized bed was 0.203 m (8.0 in.), while the phase-change material, a 60% copper—40% zinc alloy, was contained within stainless steel tubes with a diameter of 0.127 m (0.5 in.). Oatley's model was very accurate during cooling tests with no phase-change material in the bed, with a temperature difference between the experimental and model data less than 5 K (9°F) throughout the entire cooling period. There was slightly less agreement between the data during cooling tests with phase-change material present, but the difference between the experimental and model data was less than 30 K (54°F) throughout the entire cooling period.

Pletka refined the one-dimensional model developed by Oatley and applied it to a fluidized bed reactor with an internal diameter of 0.457 m (18 in.) with a phase-change material, lithium fluoride (LiF), contained within stainless steel tubes with a diameter of 0.254 m (1.0 in.). Pletka performed bed cooling tests as Oatley had, but Pletka used steam to cool the bed rather than air. He also attempted to model the chemistry occurring during the pyrolysis phase of ballasted gasification. Attempts to model the steam cooling tests, in which no pyrolysis occurred within the reactor, were fairly successful, with temperature differences of less than 25 K (45°F) during tests with phase-change material present as well as tests without phase-change material present in the bed. Attempts to model the pyrolysis phase of ballasted gasification based on thermodynamic predictions of the gas composition were less successful as it was shown that the pyrolysis reactions did not proceed to thermodynamic equilibrium. Modeling of the pyrolysis phase was improved by using an average of the measured gas composition, but the resulting profile still did not match the behavior seen in the experimental data.

While the model developed by Pletka provided fairly accurate temperature profiles through steam cooling tests as a whole, the largest differences between the model and experimental data occurred during the phase-change period of the phase. The model predicted a brief period of isothermal behavior in the reactor, which was not seen in experimental data. Pletka attributed the inconsistency between the model and experimental data during phase-change to the development of temperature gradients within the ballast tubes as the phase-change material cooled [8]. As the lithium fluoride nearest the wall solidified, it would form an insulating barrier

between the tube surface and the remaining liquid-phase material. This hypothesis was not investigated during previous research.

3. MODEL FORMULATION AND EXPERIMENTAL METHODS

3.1 Model formulation

A model was developed to predict gasifier behavior during the pyrolysis phase of ballasted gasification. Based on initial reactor temperatures and mass flowrates of biomass and steam entering the reactor, the model can predict average bed temperature throughout the cycle. The average bed temperature is indicative of the stored thermal energy within the bed, which is essential to supply energy to the endothermic pyrolysis reactions. An accurate bed temperature profile throughout the pyrolysis cycle will allow construction of accurate energy balances and optimization of operational parameters without requiring changing the current gasifier configuration. Following the establishment of optimal parameters, future configurations will be selected.

The motivation for the development of this model is to improve the predictions of fluidized bed temperature profiles during the phase-change portion of the pyrolysis phase of ballasted gasification. This is accomplished by considering the effects of the insulating layer of solid lithium fluoride that accumulates inside the walls of the ballast tubes as the phase-change process proceeds. This layer of solid lithium fluoride increases the thermal resistance between the liquid-phase lithium fluoride and the fluidized bed, inhibiting the heat transfer process. Previous models of the heat interactions between the ballast tubes and the fluidized bed assumed each ballast tube behaved as a lumped capacitance, which ignored the temperature gradients that existed within the tubes. In order to effectively consider these gradients, a new model was developed that recognized the effect of the solid-phase lithium fluoride as the solid/liquid interface receded from the wall toward the center of the tube. This model is known as the Receding Interface model.

3.1.1 *Model assumptions*

The development of this model was based on a small number of essential assumptions. These assumptions, established during the work of Oatley and Pletka [7, 8], are as follows:

- Heat transfer is one-dimensional and occurs only in the radial direction.
- The internal heat transfer coefficient is constant. The bed-to-wall heat transfer coefficient and the bed-to-tube heat transfer coefficient are assumed to have the same value.
- The bed is isothermal, and the fluidizing gas is raised to the bed temperature.

- The phase-change material melts at a constant temperature, and completely releases its latent heat of fusion.

Previous models altered the height of the bed, H_{bed} , to account for axial conduction in the reactor wall. The value of this variable was increased to mimic the effect of axial conduction. In the updated version of the model, this variable was set to the actual value that exists within the reactor, 0.61 m (24 in.). Should it be desired to consider axial conduction, the model should be expanded to a two-dimensional representation.

In order to establish the initial conditions within the reactor, the following assumptions were established:

- The inner refractory wall temperature is 30 K less than the average bed temperature. This assumption is based on observations from previous research [8].
- The temperatures of the inner and outer surface of the steel shell are equal due to the relatively high thermal conductivity of the steel.
- The temperature gradients are linear across any refractory and insulation.
- Ballast temperature is initially equal to the bed temperature.

Using these assumptions, the initial temperatures within the reactor can all be determined with knowledge of the bed temperature and the outer steel shell temperature.

3.1.2 Lumped capacitance model

The Lumped Capacitance (LC) model was composed of a 12-point nodal network, as illustrated in Figure 3.1, with additional nodes representing the ballast, steam and nitrogen flow into the reactor and ambient conditions. The model considered a reactor with 2.54 cm (1.0 in.) of internal refractory and 2.54 cm (1.0 in.) of external blanket insulation. The nodes are connected via their thermal resistances, and equations can be written to represent the network. The equations for the simpler case, unballasted gasification, are shown below. For node 1, representing the fluidized bed, the equation is as follows:

$$\frac{dT_1}{dt} = \frac{1}{m_1 \cdot c_{p,1}} \left[\dot{Q}_{steam} + \dot{Q}_{N_2} + \dot{Q}_{wall} + \dot{Q}_{pyr} \right] \quad (3.1)$$

with

$$\dot{Q}_{steam} = \dot{m}_{steam} \cdot c_{p,steam} \cdot (T_{steam} - T_1) \quad (3.2)$$

$$\dot{Q}_{N_2} = \dot{m}_{N_2} \cdot c_{p,N_2} \cdot (T_{N_2} - T_1) \quad (3.3)$$

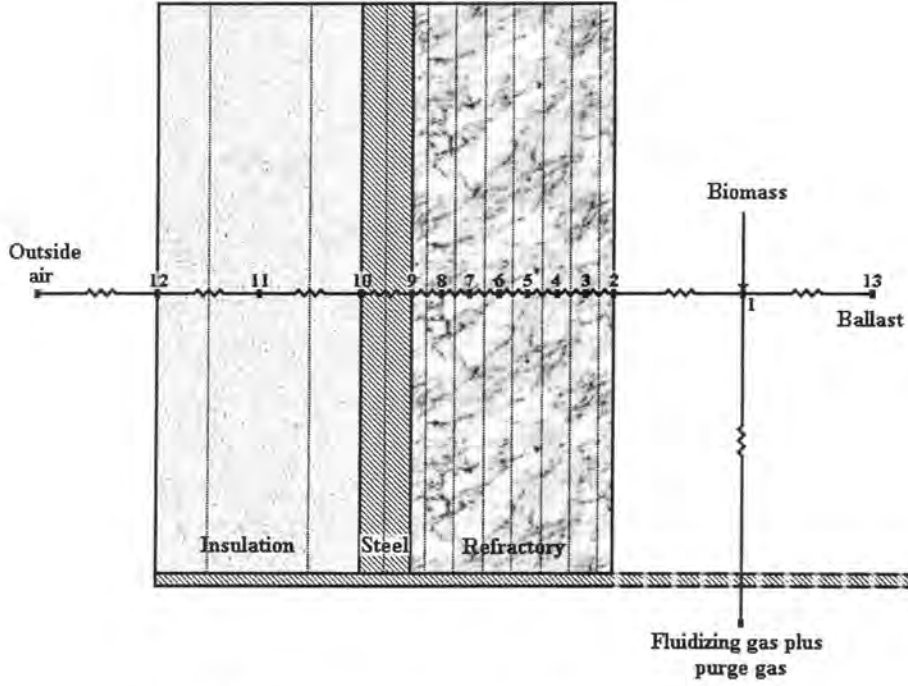


Figure 3.1—Ballasted gasification nodal network

$$\dot{Q}_{wall} = 2 \cdot \pi \cdot r_2 \cdot H_{bed} \cdot h_{wall} \cdot (T_2 - T_1) \quad (3.4)$$

$$\dot{Q}_{pyr} = \dot{m}_{biomass} \cdot \Delta h_{pyr} \quad (3.5)$$

For node 2, representing the bed/refractory wall interface, the equation is:

$$\frac{dT_2}{dt} = \frac{1}{m_2 \cdot c_{p,2}} \cdot \left[2 \cdot \pi \cdot r_2 \cdot H_{bed} \cdot h_{wall} \cdot (T_1 - T_2) + \frac{2 \cdot \pi \cdot k_2 \cdot l}{\ln(r_3 / r_2)} \cdot (T_3 - T_2) \right] \quad (3.6)$$

For node 3 through node 11, the nodes not exposed to convection and limited to heat transfer via conduction, the equations are of the form:

$$\frac{dT_i}{dt} = \frac{1}{m_i \cdot c_{p,i}} \cdot \left[\frac{2 \cdot \pi \cdot k_{i-1} \cdot l}{\ln(r_i / r_{i-1})} \cdot (T_{i-1} - T_i) + \frac{2 \cdot \pi \cdot k_i \cdot l}{\ln(r_{i+1} / r_i)} \cdot (T_{i+1} - T_i) \right] \quad (3.7)$$

Finally, for node 12, representing the blanket insulation/environment interface, the equation is:

$$\frac{dT_{12}}{dt} = \frac{1}{m_{12} \cdot c_{p,12}} \cdot \left[\frac{2 \cdot \pi \cdot k_{11} \cdot l}{\ln(r_{12} / r_{11})} \cdot (T_{11} - T_{12}) + 2 \cdot \pi \cdot r_{12} \cdot l \cdot h_{ext} \cdot (T_{amb} - T_{12}) \right] \quad (3.8)$$

For all of the above equations,

T_i	= temperature of node i, K
T_{steam}	= inlet temperature of fluidizing steam, K
T_{N_2}	= inlet temperature of nitrogen purge gas, K
t	= time variable, sec
m_i	= mass of node i, kg
$\dot{m}_{biomass}$	= mass flowrate of biomass, kg/s
\dot{m}_{steam}	= mass flowrate of fluidizing steam, kg/s
\dot{m}_{N_2}	= mass flowrate of nitrogen purge gas, kg/s
$c_{p,i}$	= specific heat of node i, J/kg-K
$c_{p,steam}$	= specific heat of fluidizing steam, J/kg-K
c_{p,N_2}	= specific heat of nitrogen purge gas, J/kg-K
r_i	= radial position of node i, m
H_{bed}	= height of bed, m
k_i	= thermal conductivity of node i, W/m-K
Δh_{pyr}	= enthalpy of pyrolysis (reaction), J/kg of biomass
h_{wall}	= heat transfer coefficient at the refractory wall, J/m ² -K
h_{ext}	= external heat transfer coefficient, J/m ² -K

During ballasted gasification, the equations describing nodes 2-12 still apply. However, the equation describing node 1 must be reformulated to consider the heat transfer rate due to the ballast, $\dot{Q}_{ballast}$:

$$\frac{dT_1}{dt} = \frac{1}{m_1 \cdot c_{p,1}} \cdot [\dot{Q}_{steam} + \dot{Q}_{N_2} + \dot{Q}_{wall} + \dot{Q}_{ballast} + \dot{Q}_{pyr}] \quad (3.9)$$

$$\dot{Q}_{steam} = \dot{m}_{steam} \cdot c_{p,steam} \cdot (T_{steam} - T_1) \quad (3.10)$$

$$\dot{Q}_{N_2} = \dot{m}_{N_2} \cdot c_{p,N_2} \cdot (T_{N_2} - T_1) \quad (3.11)$$

$$\dot{Q}_{wall} = 2 \cdot \pi \cdot r_2 \cdot H_{bed} \cdot h_{wall} \cdot (T_2 - T_1) \quad (3.12)$$

$$\dot{Q}_{ballast} = n_{tubes} \cdot [2 \cdot \pi \cdot r_{13} \cdot l_{tube} \cdot h_{tube} \cdot (T_{13} - T_1)] \quad (3.13)$$

$$\dot{Q}_{pyr} = \dot{m}_{biomass} \cdot \Delta h_{pyr} \quad (3.14)$$

where,

- n_{tubes} = number of ballast tubes within fluidized bed
- r_{13} = radius of ballast tube, m
- l_{tube} = length of ballast tube, m
- h_{tube} = heat transfer coefficient at the tube surface, W/m²-K

The ballast is modeled by a single node point, Node 13. Prior to the period of phase change (solidification of the molten lithium fluoride), the following equation applies:

$$\frac{dT_{13}}{dt} = \frac{1}{m_{13} \cdot c_{p,13}} \cdot [2 \cdot \pi \cdot r_{13} \cdot l_{tube} \cdot h_{tube} \cdot (T_{13} - T_1)] \quad (3.15)$$

During the isothermal solidification, Equation 3.15 is replaced by the following equation:

$$\frac{dT_{13}}{dt} = 0, \quad (3.16)$$

and an equation is introduced to account for the latent heat dissipated:

$$\frac{dQ_{latent}}{dt} = 2 \cdot \pi \cdot r_{13} \cdot l_{tube} \cdot h_{tube} \cdot (T_{13} - T_1), \quad (3.17)$$

where Q_{latent} , integrated from Equation 17, is the total latent heat dissipated during the solidification process. Following the completion of the phase change, the behavior of the ballast is described once again by Equation 15. To predict the temperature profiles, a fourth-order Runge-Kutta numerical integration method is employed.

The LC model predicts behavior consistent with ideal ballasted gasification operation. In this model, the phase-change material, lithium fluoride, is assumed to behave as a two-phase mixture during the transition from liquid to solid, and the stainless steel tube that contains the phase-change material is assumed to be transparent to the energy flows. The isothermal phase-change process creates a period of thermal equilibrium, where thermal energy losses in the bed are matched by stored thermal energy released by the ballast. During this period, the temperature of the bed remains constant. Following the solidification of all of the phase-change material within the ballast, the temperature of the bed falls dramatically, as there is no more stored energy to counterbalance the energy losses from the reactor.

Ideal behavior is not seen in the experimental data of previous research, however [8]. There are no periods of isothermal operation and the temperature profile is smooth. This smooth

profile suggests that the transfer of thermal energy from the ballast tubes to the fluidized bed is inhibited during actual ballasted gasification operation. To explain this inhibition of heat transfer, it is hypothesized that the solid lithium fluoride would present a significant resistance to latent heat transfer as the remaining liquid material changed phase. If this insulating nature of the solidified lithium fluoride is considered, temperature gradients must exist within the ballast tube itself, and the stainless steel shell is no longer transparent to the heat transfer. The stainless steel surface of the tube, with which the fluidized bed is in contact and exchanging heat, is always lower in temperature than the lithium fluoride undergoing phase change. Thus, a lumped capacitance model is inadequate to describe the behavior of the phase-change process, and a more sophisticated model was developed to account for the temperature gradients within the each tube.

3.1.3 *Receding interface model*

A second model, termed the Receding Interface (RI) model, was established to accurately predict the effect of the ever-increasing layer of solid-phase lithium fluoride during solidification. In the Receding Interface model, the liquid and solid phases of the lithium fluoride are treated as distinct entities. This model is illustrated in Figure 3.2. The phase change material is contained within a stainless steel shell, with an outer radius, Radius 13, and an inner radius, Radius 14. As the lithium fluoride changes phase from liquid (represented by the red core) to solid (represented by the blue outer layer), it is suggested that a liquid/solid interface exists at Radius 15 and recedes toward the center of the tube. At the onset of pyrolysis (see Figure 3.2 (a)), the RI model considered the ballast tubes to be filled with molten lithium fluoride (Radius 15 = Radius 14) transferring sensible heat to the bed. As the lithium fluoride cools to the phase-change temperature and solidification commences (see Figure 3.2 (b) and (c)), the latent heat of fusion is released to the fluidized bed and the liquid/solid interface moves radially inward (Radius 15 < Radius 14), until the interface reaches the centerline of the tube (see Figure 3.2 (d)), when solidification is complete (Radius 15 → 0). Following the completion of the phase change, the lithium fluoride continues to cool, once again providing sensible heat to the fluidized bed.

The equations describing the behavior of node 1 through node 12 in the RI model are unchanged from the original LC model. However, the equations describing the behavior of the ballast tubes must be reformulated. Rather than a single node to represent the ballast tubes, two nodes are now attributed to the tubes, with one representing the stainless steel portion of the tube and the other representing the lithium fluoride portion. Prior to the commencement of the

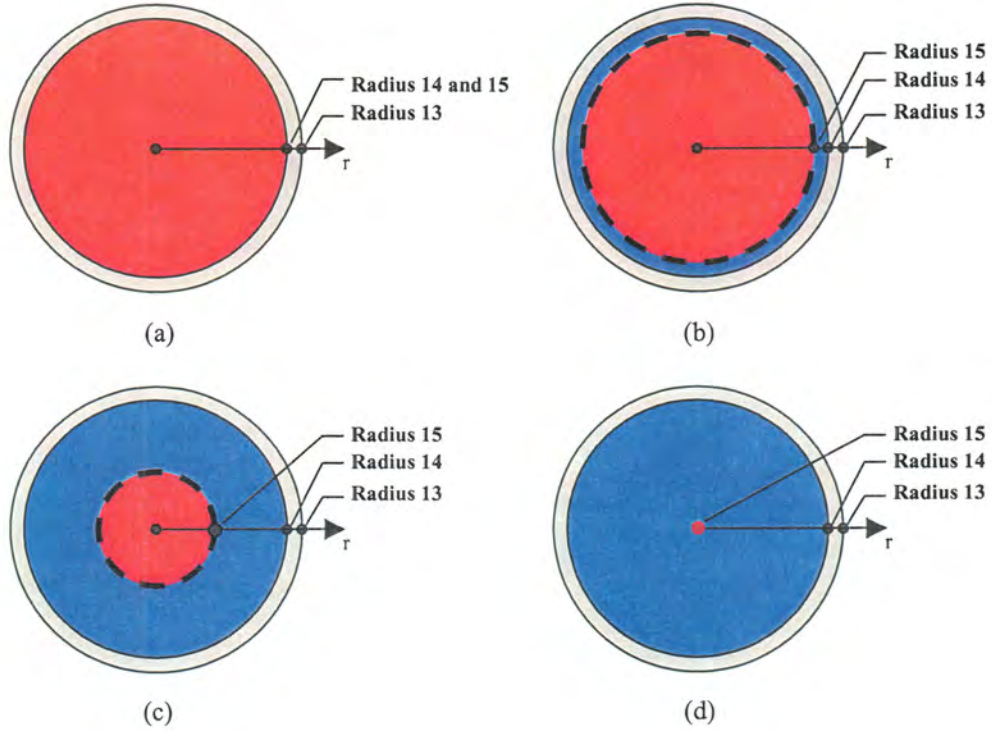


Figure 3.2—Illustration of Receding Interface model applied to the ballast tubes

solidification, the temperature gradients within the stainless steel and lithium fluoride are assumed to be negligible, and the equations for the ballast nodes are as follows:

$$\frac{dT_{13}}{dt} = \frac{1}{m_{13} \cdot c_{p,13}} \cdot \left[2 \cdot \pi \cdot r_{13} \cdot l_{tube} \cdot h_{tube} \cdot (T_1 - T_{13}) + \frac{2 \cdot \pi \cdot k_{SS} \cdot l_{tube,eff}}{\ln(r_{13}/r_{14})} \cdot (T_{14} - T_{13}) \right] \quad (3.18)$$

$$\frac{dT_{14}}{dt} = \frac{1}{m_{14} \cdot c_{p,14}} \cdot \left[\frac{2 \cdot \pi \cdot k_{SS} \cdot l_{tube,eff}}{\ln(r_{13}/r_{14})} \cdot (T_{13} - T_{14}) \right] \quad (3.19)$$

where

- m_{13} = mass of stainless steel tube shell, kg
- m_{14} = mass of lithium fluoride, kg
- $c_{p,13}$ = specific heat of stainless steel tube shell, kg
- $c_{p,14}$ = specific heat of lithium fluoride, kg
- T_{13} = temperature of stainless steel tube shell, K

T_{14}	= temperature of lithium fluoride, K
r_{13}	= outer radius of stainless steel tube, m
r_{14}	= inner radius of stainless steel tube, m
l_{tube}	= length of ballast tube, m
$l_{tube,eff}$	= effective length of ballast tube, m
h_{tube}	= heat transfer coefficient at the tube surface, W/m ² -K
k_{SS}	= thermal conductivity of the stainless steel, W/m-K

It should be noted that the effective length of tube through which conduction occurs is significantly less than the actual tube length. This arises due to the level of lithium fluoride within the tube. During previous research at Iowa State University, it was observed that the lithium fluoride only occupies approximately 60% of the volume within the actual tube [8]. Thus, the effective tube length has a value equal to approximately 60% that of the actual tube length.

During the phase change, the average temperatures within the stainless steel and the lithium fluoride become irrelevant. The important temperatures are the temperature of the outer tube surface with which the fluidized bed exchanges energy and the temperature of the liquid/solid interface, the source of the released latent heat. The outer tube surface temperature (located at r_{13}) is assumed to be the temperature of Node 13 at the beginning of the phase change period. (This is valid due to the high thermal conductivity of stainless steel.) The temperature of the liquid/solid interface is specified by the phase change temperature, $T_{pc} = 1123$ K (1560°F), and thus its temperature is constant. Therefore, Node 13 is now located at the outer stainless steel surface, and Node 14 is located at the liquid/solid interface. The heat transfer equations become:

$$\frac{dT_{13}}{dt} = \frac{1}{m_{13} \cdot c_{p,13}} \cdot \left\{ 2 \cdot \pi \cdot r_{13} \cdot l_{tube} \cdot h_{tube} \cdot (T_1 - T_{13}) + \frac{2 \cdot \pi \cdot l_{tube,eff} \cdot (T_{14} - T_{13})}{\left[\frac{\ln(r_{13}/r_{14})}{k_{SS}} + \frac{\ln(r_{14}/r_{15})}{k_{LiF}} \right]} \right\} \quad (3.20)$$

$$\frac{dT_{14}}{dt} = 0 \quad (3.21)$$

where

- r_{15} = radial position of liquid/solid interface (Node 14) within ballast tube, m
 k_{LiF} = thermal conductivity of lithium fluoride, W/m-K

In order to account for total latent heat of fusion transferred from the tubes and determine the position of the phase change interface and the amount of time during which phase change occurs, the rate of latent heat transfer to the stainless steel tube is calculated during each time step from an energy balance on the tube:

$$\dot{Q}_{latent} = \frac{2 \cdot \pi \cdot l_{tube,eff} \cdot (T_{14} - T_{13})}{\left[\frac{\ln(r_{13}/r_{14})}{k_{SS}} + \frac{\ln(r_{14}/r_{15})}{k_{LiF}} \right]} \quad (3.22)$$

The mass of lithium fluoride that solidified during the time step can be estimated by dividing the product of the latent heat transfer rate and the time step by the latent heat of fusion. With the mass known, the volume required can be determined by dividing it by the density of solid lithium fluoride, and the change in the position of the liquid/solid interface can then be calculated using the formula for volume of an annulus. This process is shown in the following equations:

$$m_{fusion} = \frac{\dot{Q}_{latent} \cdot t_{step}}{h_{fus}} \quad (3.23)$$

$$V_{fusion} = \frac{m_{fusion}}{\rho_{LiF,s}} \quad (3.24)$$

$$V_{fusion} = \pi \cdot (r_{15,t+1}^2 - r_{15,t}^2) \cdot l_{tube,eff} \quad (3.25)$$

$$r_{15,t+1} = \sqrt{r_{15,t}^2 - \frac{V_{fusion}}{\pi \cdot l_{tube,eff}}} \quad (3.26)$$

where

- \dot{Q}_{latent} = latent heat transfer rate, W
 m_{fusion} = mass of lithium fluoride solidified during time interval, kg
 h_{fus} = latent heat of fusion of lithium fluoride, J/kg
 t_{step} = time interval of numerical integration method
 V_{fusion} = volume of lithium fluoride solidified during time interval, m³
 $\rho_{LiF,s}$ = density of solid lithium fluoride, kg/m³

- $r_{15,t}$ = initial radial position of liquid/solid interface during time interval, m
 $r_{15,t+1}$ = final radial position of liquid/solid interface during time interval, m

The phase change process continues until $r_{15,t+1}$ reaches zero. At this point, sensible heat transfer resumes until the end of the cooling period. To accurately model the sensible heat transfer through the rest of the cooling period, however, a small modification to Equation 3.25 is required. This modification is necessary because a singularity develops as r_{15} approaches zero (i.e. the natural log term, $\ln(r_{14}/r_{15})$, approaches infinity). To counteract this singularity, the variable r_{15} is incremented to $r_{15} + 0.00001$, as shown in the following equations:

$$\frac{dT_{13}}{dt} = \frac{1}{m_{13} \cdot c_{p,13}} \cdot \left\{ 2 \cdot \pi \cdot r_{13} \cdot l_{tube} \cdot h_{tube} \cdot (T_1 - T_{13}) + \frac{2 \cdot \pi \cdot l_{tube,eff} \cdot (T_{14} - T_{13})}{\left[\frac{\ln(r_{13}/r_{14})}{k_{SS}} + \frac{\ln(r_{14}/(r_{15} + 0.00001))}{k_{LiF}} \right]} \right\} \quad (3.27)$$

$$\frac{dT_{14}}{dt} = \frac{1}{m_{14} \cdot c_{p,14}} \cdot \left\{ \frac{2 \cdot \pi \cdot l_{tube,eff} \cdot (T_{13} - T_{14})}{\left[\frac{\ln(r_{13}/r_{14})}{k_{SS}} + \frac{\ln(r_{14}/(r_{15} + 0.00001))}{k_{LiF}} \right]} \right\} \quad (3.28)$$

This small alteration is assumed to have very little impact on the behavior of the model and allows for a smooth transition in ballast tube temperature profiles from the period of phase change to the post-phase change period.

One additional modification is made in the RI model. The LC model determined the radiation heat transfer coefficient, h_{rad} , within the bed according to the following curve fit:

$$h_{rad} = 70 + 15 \cdot [(T_{bed} - 973)/100] \quad (3.29)$$

This is not the conventional form of the radiation heat transfer coefficient, which is:

$$h_{rad} = \frac{\varepsilon_{eff} \cdot \sigma \cdot (T_{bed}^4 - T_{surface}^4)}{(T_{bed} - T_{surface})} \quad (3.30)$$

where

$$\varepsilon_{eff} = \left(\frac{1}{\varepsilon_{bed}} + \frac{1}{\varepsilon_{surface}} - 1 \right) = \text{effective emissivity within the fluidized bed reactor}$$

ε_{bed} = emissivity of the fluidized bed

$\varepsilon_{surface}$ = emissivity of the inner surface (wall) of the reactor

σ = Stefan-Boltzmann constant = 5.67×10^{-8} , W/m²-K⁴

The empirical curve fit described in Equation 3.29 was developed for fluidization parameters similar to those of the current system [7]; however, it is unknown how slight differences in fluidization parameters will affect the accuracy of the curve fit. Therefore, the theoretical fourth-order formulation of the radiation coefficient (as described in Equation 3.30) was used to best model radiation effects in the RI model.

The Receding Interface model was programmed in C++, and the code is listed in Appendix A.

3.2 Experimental methods

The thermally-ballasted fluidized bed gasification process was experimentally investigated at the Biomass Energy Conversion (BECON) Facility in Nevada, Iowa. This facility operates under the auspices of the Iowa Energy Center. The investigation was conducted in the autumn of 2002. The equipment used to perform this work and the methods used to conduct testing are described in the following sections.

3.2.1 Experimental equipment

A pilot-scale biomass gasification system was assembled in 2000. This system was designed to investigate aspects of biomass gasification processes ranging from feedstock evaluation to producer gas analysis and cleanup. A wide range of feedstocks can be processed within the reactor, including but not exclusive to waste seed corn, switchgrass, corn stover and wood. The gasification system is able to process approximately five tons of biomass per day. The major components of the system are: the fluidized bed reactor; the latent heat ballast; the fuel feeding system; the data acquisition and control system; and the gas sampling and analysis system. A schematic of the reactor with the feed system is shown in Figure 3.3.

3.2.1.1 Fluidized bed reactor

Biomass fuels are processed in an atmospheric bubbling fluidized bed reactor. The reactor has an inner diameter of 0.457 m (18 in.). The reactor is comprised of two sections, a bed

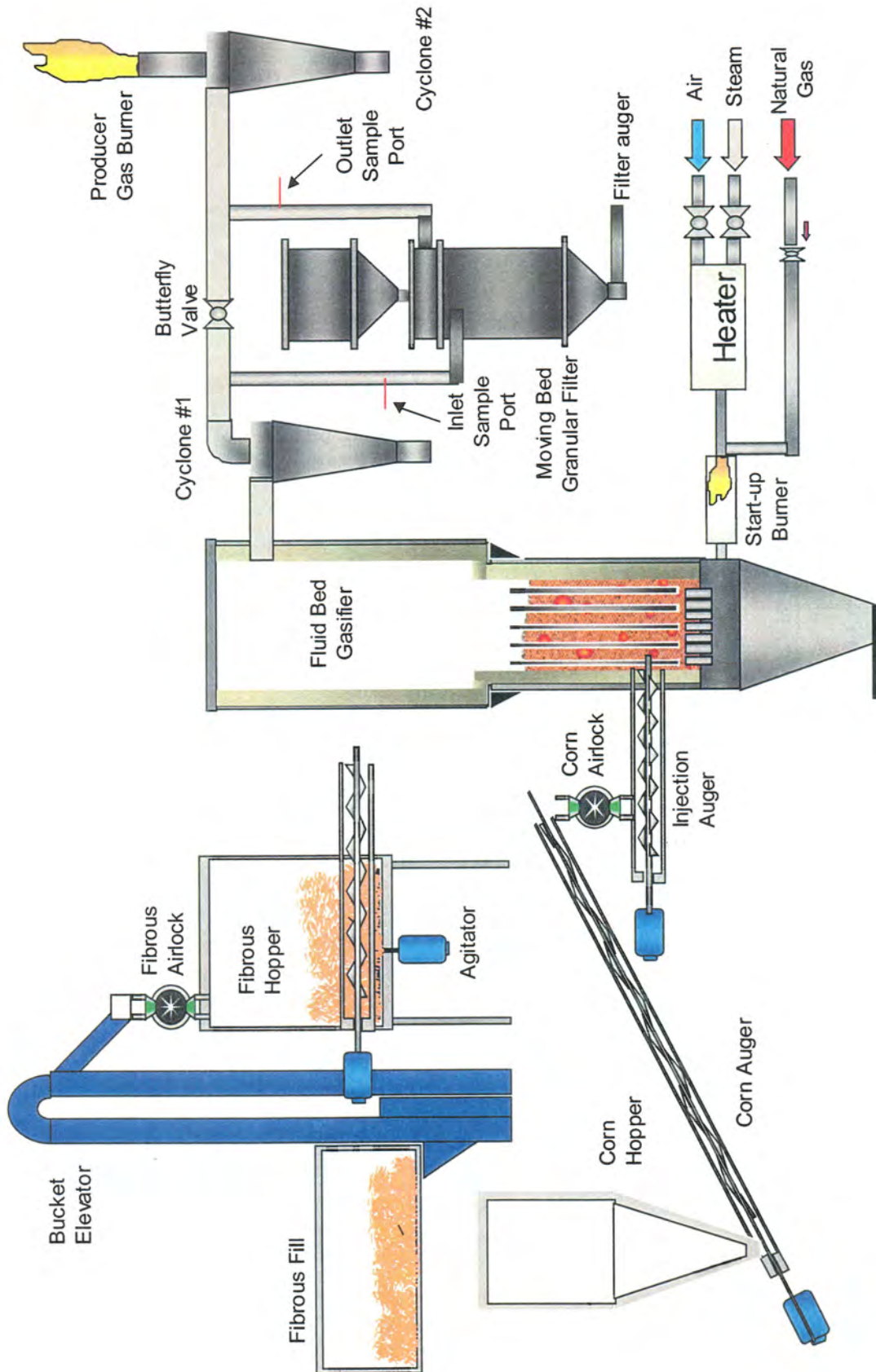


Figure 3.3—Schematic of the biomass gasification system

section and a freeboard section (labeled as (b) and (c), respectively, in Figure 3.4). The bed section has a height of 1.22 m (48.0 in.), while the freeboard has a height of 2.44 m (96.0 in.) Each section is constructed of 6.35 mm-thick (0.25 in.) mild steel. There are ports in the bed section to allow temperature and pressure monitoring.

There are 10 thermocouple ports used to monitor the temperature and 5 pressure taps to monitor pressure differentials within the bed. Biomass is fed through a 15.2 cm (8.0 in.) port approximately 15.2 cm (8.0 in.) above the distributor. The bed section contains 7.62 cm (3.0 in.) of EZ³ Lo-Erode ceramic refractory, while the freeboard is lined with 3.81 cm (1.5 in.) of EZ³ Lo-Erode refractory and 7.62 cm (3.0 in.) of IRC 25 insulating refractory. The refractories diminish the heat lost during operation.

Fluidization of the bed occurs by passing air or steam through the reactor. Air is used to fluidize the reactor during the start up process, conventional gasification and the combustion phase of ballasted gasification. The air is delivered by a positive displacement blower, which can provide air flowrates up to 254 Nm³/hr (150 SCFM). The air can be pre-heated to a temperature



Figure 3.4—Gasification reactor

of 810 K (1000°F) prior to its introduction into the bed by a natural gas burner. Steam is used to fluidize the bed during the pyrolysis phase of ballasted gasification. Saturated steam is provided by a Hurst steam boiler at pressures from 138 kPa (20 psi) to 827 kPa (120 psi). The boiler can provide steam flowrates of 227 kg/hr (500 lb/hr). The steam can be passed through a Watlow resistive circulation heater, which can raise the steam to a temperature of approximately 870 K (1100°F).

The fluidization medium, air or steam, enters the bed through the distributor (labeled as (a) on Figure 3.4), which is comprised of 32 nozzles with holes oriented along the longitudinal axis of the nozzle. This orientation prevents sand from clogging the nozzles. The medium passes through the bed material, which has a height of approximately 0.61 m (24 in.) during fluidization. The medium and products of any reaction within the bed exit through an exhaust duct 14.6 cm (5.75 in.) in diameter. The exhaust stream passes through two cyclones operated in series to remove particulate and elutriated sand. A pilot-scale moving bed granular filter (MBGF) resides between the cyclones to remove fines, although this filter may be bypassed by opening a butterfly valve. Following the filtration processes, the exhaust stream is vented to atmosphere. If the exhaust stream contains products of gasification or pyrolysis, the gases are combusted by a producer gas burner.

The start up process of the reactor begins by passing pre-heated (810 K, or 1000°F) air through the bed. When the bed reaches an average temperature of 575 K (575°F), a small amount of biomass is fed to the reactor and combusted. Feeding prior to this temperature results in poor combustion and partial gasification, actually lowering the temperature of the bed. As the bed temperature increases, the biomass feedrate can be increased and the bed temperature increases dramatically. This start up process is now automated (see Section 3.2.2 for further details). When the bed temperature reaches 1005 K (1350°F), gasification processes can commence.

3.2.1.2 Latent heat ballast

The latent heat ballast used in this study was composed of 48 stainless steel tubes. Each tube contained 0.3 kg (0.66 lb) of lithium fluoride. Thus, the bed contained 14.4 kg (31.7 lb) of lithium fluoride with a total latent heat storage capacity of 15.1 MJ (14,300 Btu). Significant properties of lithium fluoride are listed in Table 3.1.

The stainless steel tubes had a diameter of 2.54 cm (1.0 in.) and a length of 0.61 m (24 in.). Endcaps were welded onto the tubes after the placement of the lithium fluoride within. To place the tubes within the reactor, a simple support structure was constructed out of 2.54 cm (1.0 in.) pipe couplings. These couplings, 66 in total, were welded together in a honeycomb pattern,

and the tubes were placed within the couplings. One endcap on each of the tubes had a diameter of 3.18 cm. (1.25 in.), preventing the tubes from completely passing through the couplings. The collection of tubes was suspended from a support plate inserted between the fluidized bed and the freeboard of the reactor. Four threaded rods were used to connect the support plate and the tube support. The stainless steel tubes and support structure were constructed during previous ballasted gasification testing [8]. A picture of the ballast tubes prior to their insertion into the reactor is shown in Figure 3.5, while Figure 3.6 illustrates the layout of the ballast tubes within the reactor.

The lithium fluoride within the ballast tubes provides 15.1 MJ (14,300 Btu) of latent heat storage capacity within the bed. This is not the total amount of energy stored within the bed, however. The sensible heat stored in the fluidized bed as well as the sensible heat of the lithium fluoride must also be considered. The specific heat of lithium fluoride is constant at a value of 2.47 kJ/kg-K above the melting point of the compound (1121 K, or 1560°F), but drops to 2.22 kJ/kg-K as temperature approaches 900 K (1160°F) [39]. Assuming an average value of specific heat of 2.3 kJ/kg-K, 8.28 MJ are stored as the temperature of 14.4 kg (31.7 lb) of lithium fluoride is raised from 922 K (1200°F) to 1172 K (1650°F). The fluidized bed is composed of 80% quartz sand and 20% limestone. The specific heat of quartz sand is virtually constant across the relevant temperature range, with a value of 1.170 kJ/kg-K. The specific heat of the limestone is assumed constant at a value of 0.810 kJ/kg-K. Thus, the sensible heat stored within the fluidized bed is approximately 41.2 MJ. These values are displayed in Table 3.2.

3.2.1.3 Fuel feeding system

Two distinct and complete feeding systems exist at BECON. The first system is dedicated to the feeding of shelled corn. The second feeding system is used to feed all other herbaceous fuels, such as switchgrass, corn stover and oat hulls. These latter fuels require a separate fuel handling system due to their low density and nonuniform shape. Shelled corn has a

Table 3.1—Significant properties of lithium fluoride [8]

Property	Lithium Fluoride
Melting temperature (K)	1121
Latent heat of fusion (kJ/kg)	1050
Specific heat (J/kg-K)	2400
Density—solid phase (kg/m ³)	2330
Density—liquid phase (kg/m ³)	1800
Thermal conductivity—solid phase (W/m-K)	4.0
Thermal conductivity—liquid phase (W/m-K)	1.7



Figure 3.5—Ballast tubes prior to their insertion into the reactor

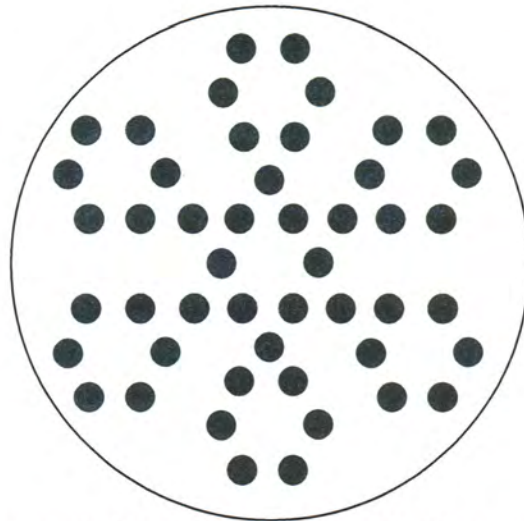


Figure 3.6—Layout of the ballast tubes within the reactor (top view)

Table 3.2—Energy stored as the bed temperature is raised from 922 K to 1172 K

	Sensible heat (MJ)	Latent heat (MJ)	Total (MJ)
Fluidized bed	41.2	0.0	41.2
Lithium fluoride	8.3	15.1	23.4

density of approximately 800 kg/m^3 (50 lb/ft^3) and a maximum particle dimension of approximately 13 mm (0.5 in.), while the fibrous fuels have densities of approximately 80-130 kg/m^3 (5-8 lb/ft^3) and can have strands as long as 50 mm (2 in.) [8]. While physically different, most biomass fuels are similar chemically. Proximate and ultimate analyses are shown for shelled corn in Table 3.3 and Table 3.4, respectively.

Of the two systems, the corn feeding system is substantially simpler. This system consists of a hopper, feeding auger and rotary airlock. The corn hopper is large enough to hold more than 6800 kg (15,000 lb) of corn. The feeding auger transports corn to the rotary airlock, which serves to prevent backflow of gases from the reactor. After passing through the airlock, the corn enters the injection auger, which serves both feeding systems. The injection auger transports the biomass into the middle of the bed, allowing the fuel to mix thoroughly in the bed. Due to the low density and fibrous nature of the herbaceous fuels, the fuel handling system for these materials includes a metering hopper as well as all of the components described above. The metering hopper is required to keep the fuel under an adequate pressure to promote consistent feeding, as the weight of the fuel is not sufficient to accomplish this task. The metering hopper is pressurized with compressed house air. Herbaceous fuels are dumped into a loading hopper, and augers at the bottom of the hopper propel the fuel into a bucket elevator, which directs the fuel through a large rotary airlock into the metering hopper. A metering auger then transports the fuel into the injection auger. As mentioned above, the injection auger serves both systems.

While the fluidized bed reactor is termed an atmospheric pressure reactor, pressures within the reactor are slightly greater than atmospheric due to pressure drops through the exhaust system. This slight pressurization of the reactor causes a small portion of the producer gases to flow back through the feeding system. In order to prevent the backflow of noxious gas, a purge gas is injected into the injection auger. This gas also serves to cool the injection auger, preventing the volatilization of the fuel prior to its arrival in the bed. House air can be used as

Table 3.3—Proximate analysis and heating value of selected feedstocks (dry basis) [8]

Feedstock	Ash (wt-%)	Volatile matter (wt-%)	Fixed carbon (wt-%)	HHV (kJ/kg)
Shelled corn	1.3	86.5	12.2	17,300

Table 3.4—Ultimate analysis of selected feedstocks (as received) [8]

Feedstock	Carbon (wt-%)	Hydrogen (wt-%)	Nitrogen (wt-%)	Oxygen (wt-%)	Sulfur (wt-%)	Ash (wt-%)
Shelled corn	39.8	6.6	1.1	51.2	0.1	1.2

purge gas during all reactor processes except the pyrolysis phase of ballasted gasification. During the pyrolysis phase, nitrogen or some other inert gas must be used. For this work, nitrogen gas was employed for this purpose.

Due to the relatively large diameter of the injection auger, a purge gas flowrate of 17.0-30.6 Nm³/hr (10-18 SCFM) was required. This flowrate is difficult to provide with conventional pressure gas cylinders, and large cryogenic nitrogen tanks were used to deliver the necessary gas. These tanks have a capacity 17 times that of conventional cylinders. Four cryogenic cylinders operated in parallel were able to provide the necessary flowrate of purge gas, and a rotameter was used to monitor the flow. While the cylinders contain liquid/gas mixture of nitrogen, the required flowrates are sufficiently small so that only gas-phase nitrogen was drawn from the cylinder. The gas delivered, however, is not at standard temperature and pressure; the temperature is less than this, approximately 273-283 K (32-50°F), while the pressure is greater to overcome pressure drops in the nitrogen lines and the feeding system. A further concern was discovered when one or two tanks began providing a much larger flowrate than the others. If the flowrate from an individual cylinder became too great, liquid nitrogen would pass through the lines, and the temperature inside the lines could drop sufficiently for frost to condense on their exterior. Constant monitoring was required to prevent the lines from “freezing.” When the tanks operated in a “balanced” fashion, with each tank providing an equally-proportioned flowrate, the nitrogen delivery system worked well.

3.2.1.4 Data acquisition and control system

An Allen-Bradley Programmable Logic Control (PLC) system was installed at the BECON facility in September and October of 2002. The ladder logic software used to program the control algorithm was RS Logic, while Wonderware was chosen as the graphical user interface. The programming of this software was completed by Teamwork Technologies, Inc. (TTI), of Clear Lake, Iowa. The PLC system consists of SLC 5.0 processing unit, 3 thermocouple input cards, 2 analog input cards, 2 analog output cards, 1 digital input card and 1 digital output card.

Temperature measurements are made at five different elevations within the bed, with two thermocouples opposite each other at each height. The temperature of the fluidizing medium is monitored immediately prior to its introduction into the distributor, and the producer gas temperature is measured throughout the exhaust ducting. Differential pressure measurements are observed across five heights. Load cells have been installed beneath the hoppers of both feeding

systems. All of these measurements are recorded in a data file during testing. In addition to these measurements, the biomass, air and steam flowrates, as determined by the output signal from the control system, and the output from the gas cart (see Section 3.2.1.5) are recorded. Data is written to a file every 10 seconds.

Nearly all of the functions of the ballasted gasification system are controlled by the control system. The only devices that are not directly controlled by the system are the steam preheater, the natural gas burner (used to preheat air) and the producer gas burner. The system does monitor the status of both burners, however.

The control system is able to manage almost all of the tasks required to switch the operation of the reactor between combustion and pyrolysis. The biomass feedrate is altered through a variable frequency drive (VFD) controlled by the Allen-Bradley system. The blower, which supplies the air for combustion, is activated and shut down through a VFD as well. The flowrate of the air is determined by a hot-wire anemometer. The steam flow is controlled directly by the system through an actuated steam valve and is monitored with a steam mass flow meter. The switch between the phases is determined by the average bed temperature within the reactor. A lower and upper temperature setpoint are established prior to operation the cycle. The only task not controlled by the Allen-Bradley system is the activation of the steam preheater, which must be enabled during the pyrolysis phase and disabled during the combustion phase.

3.2.1.5 Gas sampling and analysis system

In order to monitor and characterize the composition of the producer gas, a slipstream is drawn from the exhaust duct. The sampling port used in this work was located at the inlet of the moving bed granular filter (MBGF). As particulate matter was not being quantified at this point of the system, the sample was drawn non-isokinetically. The sampling probe had a constant diameter of 9.5 mm (0.375 in.) and was bent such that the inlet faced downstream of the producer gas flow. This orientation was used to reduce the amount of particulate matter drawn through the slipstream. The stream was passed through a series of 6 impingers immersed in an ice bath and filled with glass wool to remove particulate and condensable gases, including water. The vacuum pump used to draw the sample was located downstream of the impingers, and a rotameter and a total volume gas meter were placed after the pump. From the exit of the gas meter, the slipstream was split to deliver a sample to two separate analyzer systems: a Varian Micro-Gas Chromatograph (Micro-GC) and a gas cart consisting of a Nova Hydrogen monitor and a California Analytical Model 300 CO/CO₂/O₂ monitor.

The Varian Micro-GC is a valuable analyzer considering the dynamic processes being investigated in this work, able to provide a gas composition every 3 minutes. This instrument is able to provide the volumetric percentage of the following gases in the sample: hydrogen (H_2), oxygen (O_2), nitrogen (N_2), carbon monoxide (CO), carbon dioxide (CO_2), methane (CH_4), acetylene (C_2H_2), ethylene (C_2H_4), ethane (C_2H_6) and propane (C_3H_8). The Micro-GC is equipped with a Thermal Conductivity Detector (TCD). It should be pointed out that the Micro-GC draws a sample for thirty seconds, and the resulting composition is the average composition during the sampling period rather than an instantaneous result. However, this instrument's ability to perform analysis of non-steady gas compositions is far superior to that of standard gas chromatographs. The Micro-GC was calibrated using three different calibration gases to capture the wide-ranging changes in gas composition during the ballasted gasification cycle.

The Micro-GC was calibrated using four different calibration gases to capture the wide-ranging changes in gas composition during the ballasted gasification cycle. The compositions of the calibration gases are shown in Table 3.5. The first gas, Gas 1, extends the calibrated range of hydrogen to the high levels expected during the pyrolysis phase, while the second gas extends the calibrated range of carbon dioxide. The final two gases calibrate the Micro-GC to ensure the high nitrogen levels seen during the combustion phase fall with calibration limits. Each of these gases also calibrates the Micro-GC for carbon dioxide, oxygen and small hydrocarbons.

A gas cart was assembled and is currently comprised of two instruments, the Nova Hydrogen monitor and the California Analytical Model 300 continuous emission monitor. Like the Micro-GC, the Nova Hydrogen monitor is equipped with a Thermal Conductivity Detector (TCD). This instrument is able to provide a continuous profile of the hydrogen content (vol-%) in the sample gas. The hydrogen monitor was calibrated by zeroing the instrument with 100 vol-% nitrogen gas and spanned using 100 vol-% hydrogen gas. Following discussions with the vendor, it was learned that carbon species, in particular carbon monoxide, carbon dioxide and methane interfere with hydrogen monitoring. Calculations were performed to determine the

Table 3.5—Calibration gases used to calibrate Micro-GC

	N_2 (vol-%)	H_2 (vol-%)	CO (vol-%)	CO_2 (vol-%)	O_2 (vol-%)	CH_4 (vol-%)	C_2H_2 (vol-%)	C_2H_4 (vol-%)	C_2H_6 (vol-%)	C_3H_8 (vol-%)
Gas 1	40	30	1	27	—	1	—	1	—	—
Gas 2	50	6	22	12	—	6	—	4	—	—
Gas 3	91	1	2	1	1	1	1	1	1	1
Gas 4	96	—	—	2	2	—	—	—	—	—

effect of this interference, and the relative error is between 2.5% and 7.5%. These calculations are shown in Appendix B.

The Model 300 monitor employs a non-dispersive infrared (NDIR) detector to determine carbon monoxide and carbon dioxide concentrations and a fuel cell to quantify oxygen concentration. The monitor was calibrated by zeroing with 100 vol-% nitrogen gas for all three species. The span gas used for carbon monoxide and carbon dioxide contained 60 vol-% carbon monoxide (balance N₂) and 40%vol carbon dioxide (balance N₂), respectively. The oxygen monitor was spanned using a gas with a composition of 21 vol-% oxygen and 79 vol-% nitrogen.

Methods exist to quantify tar and moisture content of the producer gas, as well as the mass of char and particulate collected by the cyclones. These methods were not employed in the present study.

3.2.2 *Experimental procedures*

Prior to the conduction of ballasted testing, the fluidized bed was placed in the reactor. The fluidized bed consisted of 150 kg (330 lb) of a quartz sand/limestone mixture. The mixture was composed of 80% sand and 20% limestone.

The heat up process of the fluidized bed was controlled primarily by the Allen-Bradley control system. The first portion of the process was accomplished by passing pre-heated air through the bed. A natural gas burner pre-heated the air to 810 K (1000°F), and this air raised the temperature of the bed to approximately 590 K (600°F). At this point, seed corn was fed to the bed at low feedrate, approximately 11 kg/hr (25 lb/hr). As the bed temperature reached 670 K (750°F), the corn feedrate was increased to 22 kg/hr (50 lb/hr). The feedrate was increased once more to 45 kg/hr (100 lb/hr) when the bed temperature achieved 810 K (1000°F). This feedrate was sufficient to heat the reactor to temperatures required for any gasification process.

As mentioned earlier, purge gas is required to keep the feeding system sufficiently cool during operation of the gasifier. Air was used to purge the feeding system during heat up, but nitrogen was used during all portions of ballasted gasification testing. The flowrate was set based on the external temperature of the injection auger. An attempt was made to keep this temperature below 313 K (105°F). The purge gas flowrate was increased until this criterion was met. Once the purge gas flowrate was set, it was not altered.

As described in Section 3.1.4, the switch between the combustion and the pyrolysis phases was determined by the average of the ten bed temperature measurements. Combustion proceeded until the average bed temperature reached 1172 K (1650°F). At this point, the control system shut down the air flow and opened the steam line. The steam pre-heater was turned on

manually, set to a temperature of 810 K (1000°F). The biomass feedrate was increased to the pyrolysis feedrate, and pyrolysis continued until the average bed temperature fell to 922 K (1200°F). The steam was shut down, the steam pre-heater was turned off, and the air flow was returned to the reactor. The air was not pre-heated during the combustion phase, which continued until the bed temperature once again reached 1172 K (1650°F). The switching strategy used during pyrolysis testing is illustrated in Figure 3.7 and listed in Table 3.6.

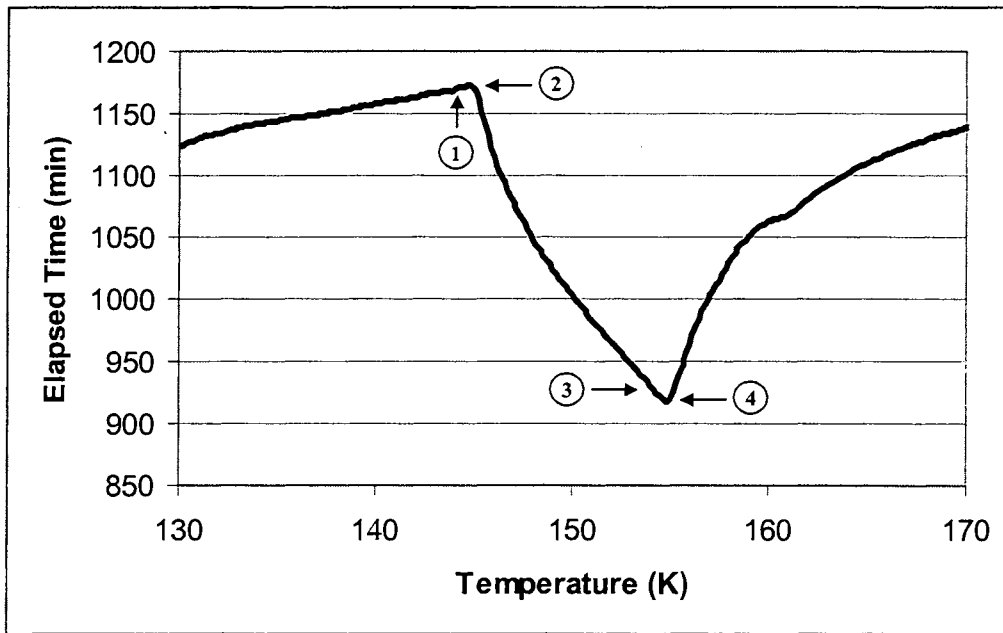


Figure 3.7—Temperature profile during ballasted gasification illustrating control strategy

Table 3.6—Phase-switching control strategy during pyrolysis testing

Point	Bed Temp (K)	Action(s)	Control Type
1	1167	Set steam preheater temperature to 810 K (1000°F)	Manual
2	1172	Set air flowrate to 0 Nm ³ /hr (0 SCFM)	Automated
		Set steam flowrate to 90.9 kg/hr (200 lb/hr)	Automated
		Increase biomass feedrate to 182 kg/hr (400 lb/hr)	Automated
3	927	Set steam preheater temperature to 422 K (300°F)	Manual
4	922	Set air flowrate to 161 Nm ³ /hr (95 SCFM)	Automated
		Set steam flowrate to 0.0 kg/hr (0.0 lb/hr)	Automated
		Decrease biomass feedrate to 68 kg/hr (150 lb/hr)	Automated

4. RESULTS AND DISCUSSION

Following the formulation of the Receding Interface (RI) heat transfer model, the model was validated by comparing its output against previous Lumped Capacitance (LC) modeling results and experimental data from previous research. Upon validation of the updated model, a sensitivity analysis was performed to identify the parameters which most heavily influenced the heat transfer processes. In addition to modeling efforts, experimental trials were conducted at the Biomass Energy Conversion (BECON) Facility to characterize the dynamic chemical behavior of the ballasted gasification process and obtain a profile of the gas composition throughout the pyrolysis phase. Heat transfer data was also obtained to compare with RI model predictions. The results of this work are the focus of this section.

4.1 Validation of Receding Interface model

The first step of validating the updated model was to ensure the only difference between the predictions of the updated model and the previous model lay in the modeling of the ballast tubes. This confirmation was required as the updated model was coded in C++, while the previous model was written in VisualBasic. The predictions of both models were virtually identical, and so the Receding Interface (RI) ballast tube model was inserted into the updated model.

In order to verify the accuracy of the Receding Interface (RI) model and demonstrate that the RI model offered an improvement over the Lumped Capacitance (LC) model, the RI model was used to generate predicted bed temperature profiles for steam cooling tests, in which no biomass was fed to the reactor. These steam cooling tests allow the examination of heat transfer processes that occur in the ballasted gasification system without considering the complex chemistry of the pyrolysis process. The profiles predicted by the RI model were compared to LC model predictions and experimental data from previous research for both ballasted and unballasted steam cooling of the fluidized bed [8]. The temperature profiles for unballasted and ballasted steam cooling tests are shown in Figure 4.1 and Figure 4.2, respectively. (The same time scale is used on both graphs to illustrate the beneficial impact of the ballast.)

It can be seen from the graphs that the RI model provides predictions that are closer to the experimental profile in both the ballasted and unballasted case. The differences between the LC and RI models in the unballasted case are attributed to the reformulation of the radiation heat transfer coefficient. In the ballasted case, the RI model predicts a continuous temperature decline during the phase-change period rather than the isothermal phase-change period predicted by the

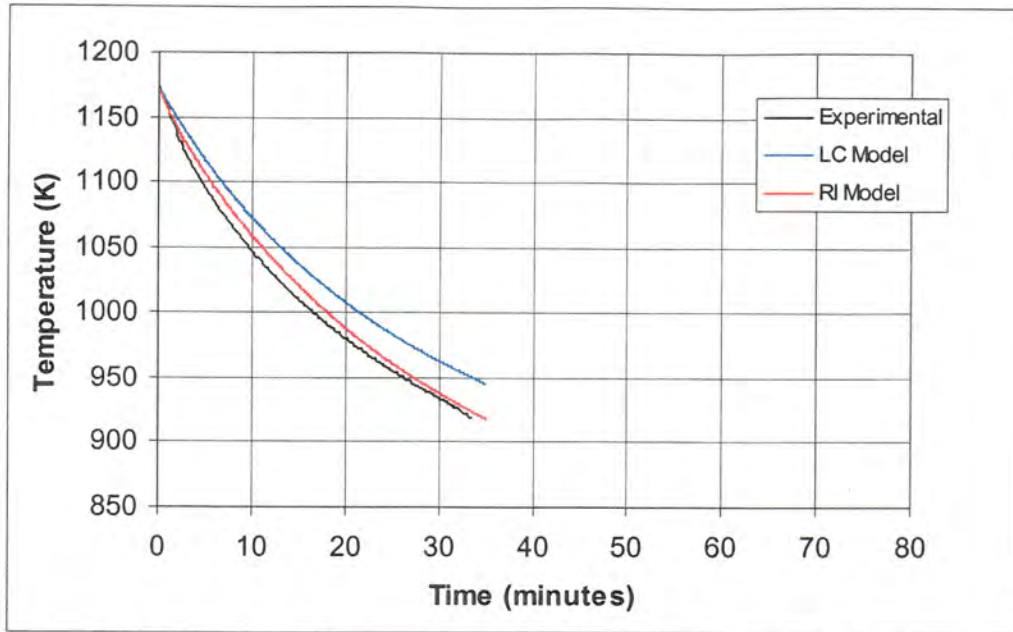


Figure 4.1—Average bed temperature during steam cooling (no ballast present)

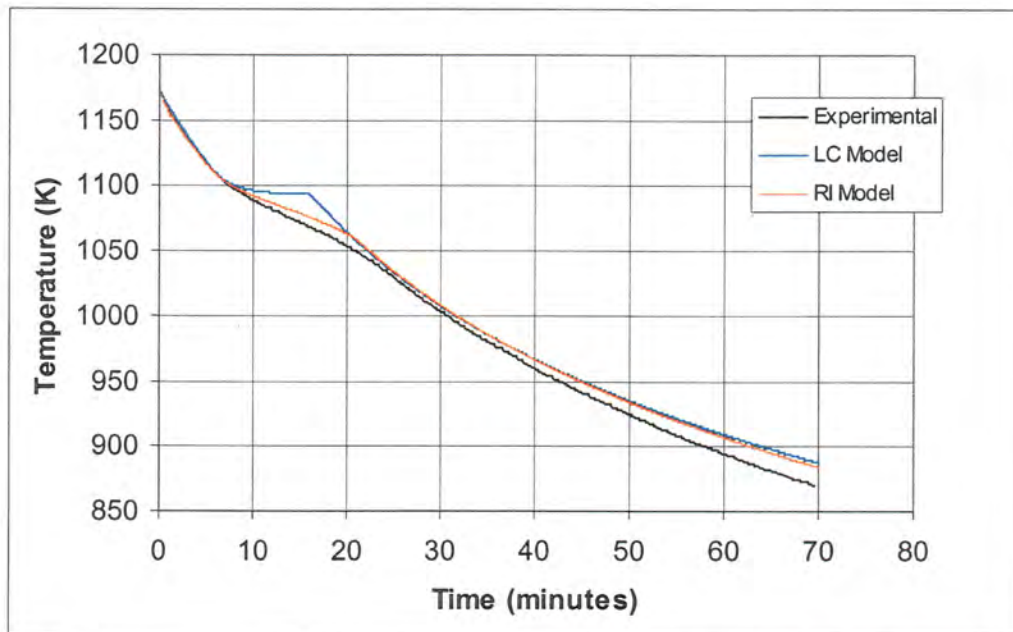


Figure 4.2—Average bed temperature during steam cooling (ballast present)

LC model. This continuous temperature decline is consistent with the behavior seen in the experimental data. The improved accuracy obtained during the phase-change does not reduce the accuracy of the RI model following the completion of the phase-change, as the RI and LC predictions are quite similar during the final 45 minutes of the steam cooling period. Thus, the RI model does indeed offer an improvement over the LC model. Both the RI and LC models predict

temperature profiles that are slightly higher than experimental profiles, but this is reasonable due to the one-dimensional modeling of the system. With the validity of the RI model demonstrated, the extent to which crucial parameters affect the behavior of the ballasted gasification cycle can be investigated.

4.2 Sensitivity analyses

Following the verification of RI model predictions, a sensitivity analysis was performed. Sensitivity analysis used in conjunction with a system model provides a means to identify variables that have the most significant impact upon system behavior. Furthermore, the extent of these impacts can be determined. This information is vital to optimize operation for complex systems with numerous variables.

Previous analyses have determined that internal and external convection coefficients, h_{wall} and h_{ext} , respectively, and the bed height, H_{bed} , have minimal impact upon the fluidized bed temperature profile [7, 8]. In the present analyses, six variables are explored: thermal conductivity of the external blanket insulation, k_{ins} ; inlet temperature of the cooling steam, T_{steam} ; the volumetric flowrate of the nitrogen purge gas, \dot{V}_{N_2} ; thermal conductivity of the lithium fluoride, k_{LiF} ; the mass of lithium fluoride per tube, m_{LiF} ; and the characteristic dimension of the ballast tubes, explored through the radius of the ballast tube, r_{tube} . The first three variables affect the operation of the entire reactor, while the other three variables predominantly affect ballast behavior. These analyses were performed considering the steam cooling tests conducted on the Biofuels Facility reactor used in previous ballasted gasification research [8]. This reactor was considered in order to eliminate pyrolysis chemistry complications and minimize the influences of large purge gas flowrates required by the current ballasted gasification system.

4.2.1 Thermal conductivity of external blanket insulation

While unaccounted for in many theoretical treatments, heat losses from non-adiabatic reactors often play a large role in determining actual reactor behavior. The thermal resistance due to conduction through a cylindrical wall, $R_{t,cond}$, from Incropera and Dewitt [40] is, in terms of inner radius and outer radius, r_1 and r_2 , respectively, the thermal conductivity of the wall, k , and the length of the cylinder, L :

$$R_{t,cond} = \frac{\ln(r_1 / r_2)}{2 \cdot \pi \cdot k \cdot L} \quad (4.1)$$

The cylindrical wall of the Biofuels Facility reactor was a composite of a 2.54 cm-thick (1.0 in.) layer of internal refractory, a 0.625 cm-thick (0.25 in.) steel shell and a 2.54 cm-thick (1.0 in.) layer of blanket insulation. Assuming that the steel shell offered negligible resistance to heat flow compared to the insulation layers, the total resistance, R_{tot} , is the sum of the thermal resistances of the refractory and insulation, in terms of their corresponding radii and the thermal conductivities of the refractory and insulation, k_{ref} and k_{ins} , respectively. An overall heat transfer coefficient for the conductive heat transfer, UA_{cond} , can be defined as the inverse of the total conductive resistance:

$$R_{cond,tot} = \frac{\ln(r_{1,ins} / r_{2,ins})}{2 \cdot \pi \cdot k_{ins} \cdot L} + \frac{\ln(r_{1,ref} / r_{2,ref})}{2 \cdot \pi \cdot k_{ref} \cdot L} \quad (4.2)$$

$$UA_{cond} = (R_{cond,tot})^{-1} \quad (4.3)$$

In this analysis, the total resistance, R_{tot} , was varied by varying the thermal conductivity of the blanket insulation, k_{ins} . The thermal conductivity of the refractory, k_{ref} , was held constant in the analysis. The values of these conductivities are dependent upon temperature, and thus, they vary as the bed cools. However, these variations are fairly small, and the value of the k_{ref} is roughly 1.44 W/m-K, while the value of k_{ins} is approximately 0.18 W/m-K for the refractory and insulation used on the Biofuels Facility reactor. Thus, $R_{cond,tot}$ has a value of 0.154 K/W, while UA_{cond} has a value of 3.82 W/K for this reactor. The values of k_{ins} and the corresponding values of $R_{t,ins}$, $R_{t,ref}$, $R_{cond,tot}$ and UA_{cond} used in the sensitivity analysis are listed in Table 4.1. The resulting bed temperature profiles are shown in Figure 4.3.

Table 4.1—Parameters examined in sensitivity analysis of k_{ins}

Case no.	k_{ins} (W/m-K)	$R_{t,ins}$ (K/W)	$R_{t,ref}$ (K/W)	$R_{cond,tot}$ (K/W)	UA_{cond} (W/K)
1	0.01	2.430	0.019	2.449	0.41
2	0.18	0.135	0.019	0.154	6.49
3	0.88	0.028	0.019	0.047	21.28
4	7.81	0.003	0.019	0.022	45.45

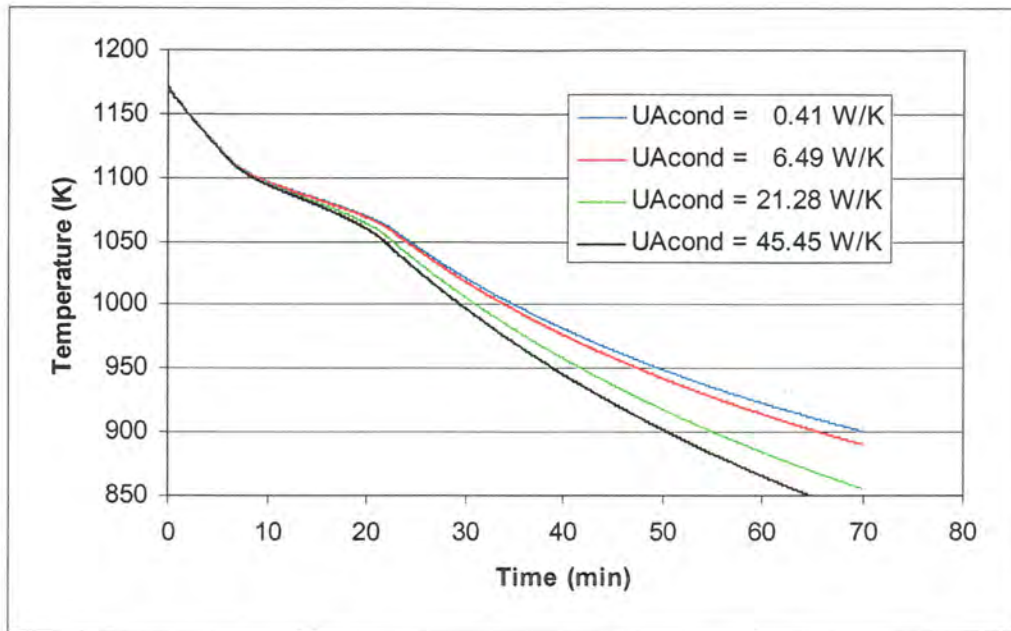


Figure 4.3—Bed temperature profiles for varied values of k_{ins}

From the profiles shown, it is clear that the thermal conductivity of the blanket insulation, k_{ins} , has a significant, although not dramatic, effect on the reactor cooling time. Increasing the amount of blanket insulation, and effectively raising the total resistance beyond the current level, with $R_{cond,tot} = 0.154$ K/W, results in only marginal gains, lengthening the time required for the bed to cool to 900 K by less than 5 minutes. Reducing the total resistance does shorten the time required for the the bed to cool to 900 K from approximately 65 minutes to approximately 55 minutes and approximately 50 minutes for values of k_{ins} of 0.88 W/m-K and 7.81 W/m-K, respectively, although any further increases in insulation thermal conductivity have virtually no effect as the resistance due to the refractory, $R_{t,ref}$, begins to dominate the total resistance term. These effects are illustrated in Figure 4.4.

4.2.2 Volumetric flowrate of the nitrogen purge gas

Although purge gas does participate in the chemical processes that may occur within the reactor and only serves to ensure proper operation of the feeding system, the presence of this gas does affect reactor operation. The presence of the gas introduces an additional energy sink within the reactor, as thermal energy is transferred from the fluidized bed to the cold (room temperature) gas. As the flowrates of the purge gas increase, this sink becomes more significant. To examine

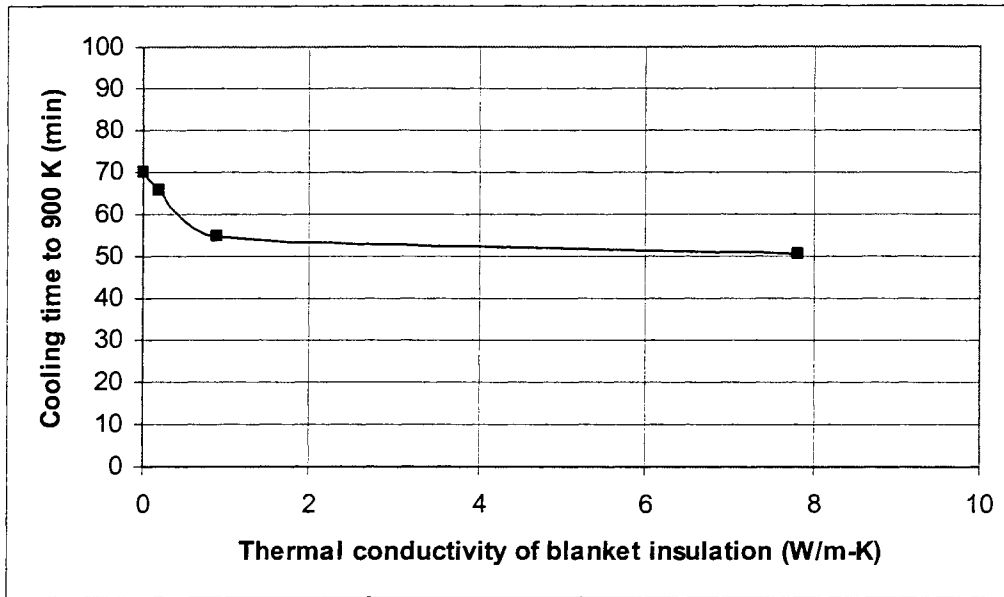


Figure 4.4—Reactor cooling time as a function of k_{ins}

this significance, a sensitivity analysis was performed investigating various mass flowrates of nitrogen into the system. Flowrates of 0.0 Nm³/hr (0.0 SCFM), 6.3 Nm³/hr (3.7 SCFM), 17.0 Nm³/hr (10 SCFM) and 30.6 Nm³/hr (18 SCFM) were examined. Results of this analysis are illustrated in Figure 4.5.

It is apparent from the temperature profiles that the flow of nitrogen purge gas can have a significant effect on reactor cooling time. If no purge gas is introduced into the reactor, the time required for the reactor to reach 922 K (1200°F) is approximately 62 minutes. If 6.3 Nm³/hr (3.7 SCFM) of nitrogen is introduced into the reactor during steam cooling, the cooling time is approximately 57 minutes, while this time is reduced to 49.5 minutes and 43 minutes when the purge gas flowrate is increased to 17.0 Nm³/hr (10.0 SCFM) and 30.6 Nm³/hr (18 SCFM), respectively. This trend is illustrated by Figure 4.6. Similar to the effect of thermal conductivity of the external insulation, changes in purge gas flowrate can reduce cooling times by a range of 10% to 20%.

4.2.3 Inlet temperature of the cooling steam

Assuming little heat loss through the wall of the reactor, the flow of relatively cold steam through the reactor is the primary heat sink in steam cooling tests, and one would intuitively expect there to be considerable variation in bed temperature profiles as the steam inlet temperature varied. The heat transfer rate, \dot{Q}_{steam} , is determined by the thermal mass flowrate of

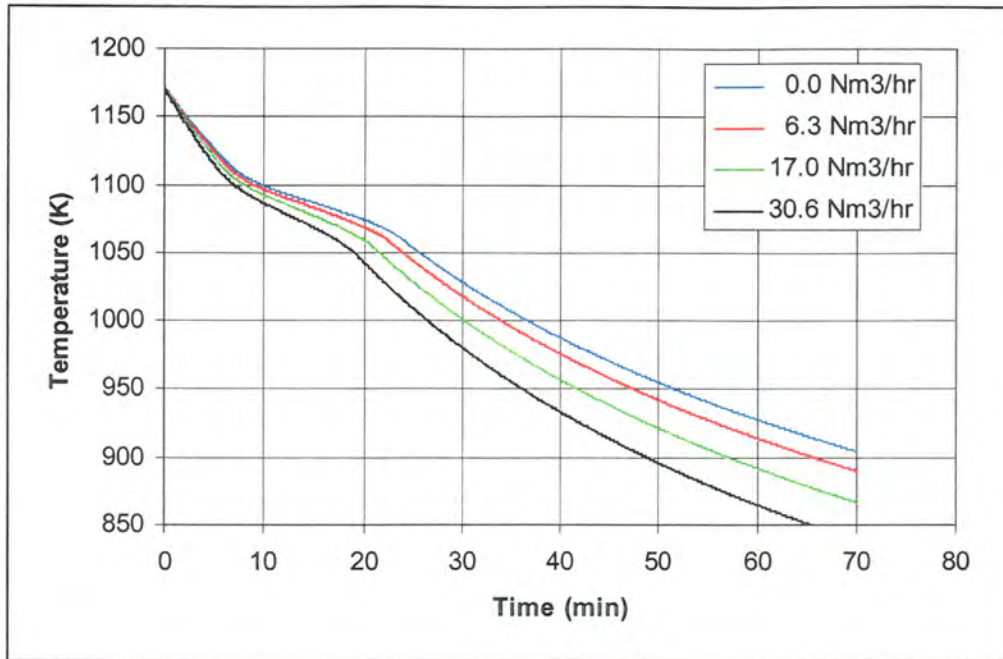


Figure 4.5—Bed temperature profiles for varied values of \dot{V}_{N_2}

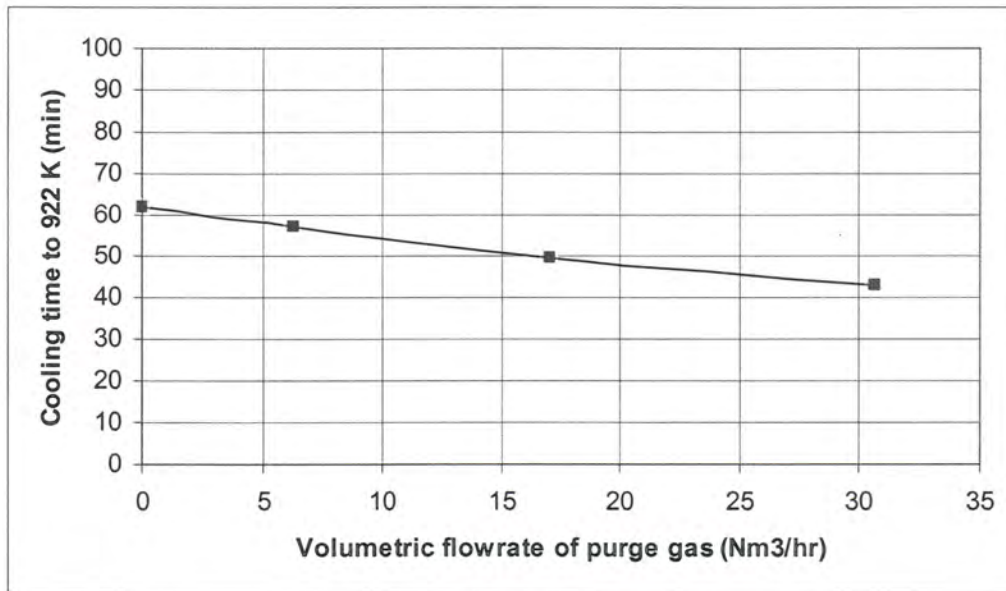


Figure 4.6—Reactor cooling time as a function of \dot{V}_{N_2}

the steam, $\dot{m}_{steam} \cdot c_{p,steam}$, and the temperature gradient, $T_{bed} - T_{steam}$, according to the relationship:

$$\dot{Q}_{steam} = \dot{m}_{steam} \cdot c_{p,steam} \cdot (T_{bed} - T_{steam}). \quad (4.4)$$

The mass flowrate of steam, \dot{m}_{steam} , is constant throughout the steam cooling period, and the specific heat of steam, $c_{p,steam}$, varies only slightly with temperature. Thus, the heat transfer rate to the steam varies almost directly with the temperature gradient, $T_{bed} - T_{steam}$. Inlet steam temperatures of 420 K, 620 K, 720 K, 820 K and 920 K were chosen for this analysis. The resulting bed temperature profiles are shown in Figure 4.7.

Illustrated by the radically different cooling curves, the inlet steam temperature has a very striking impact on the behavior of the bed, greater than the effect of external insulation. The initial temperature of the fluidized bed is constant, so as the steam inlet temperature increases the temperature gradient is diminished. Therefore, the heat transfer rate from the bed to the steam, \dot{Q}_{steam} , decreases, lengthening the time required for the bed to reach a given temperature. This decrease in \dot{Q}_{steam} is evident from the outset of the steam cooling period as each profile is distinct, even in the initial stages of cooling. In addition, neglecting losses through the wall, the bed temperature will not fall below the steam inlet temperature. Thus, this temperature establishes two important factors within the reactor; a given steam inlet temperature sets the temperature gradient between the steam and the bed as well as fixes the steady-state (final temperature) of the bed.

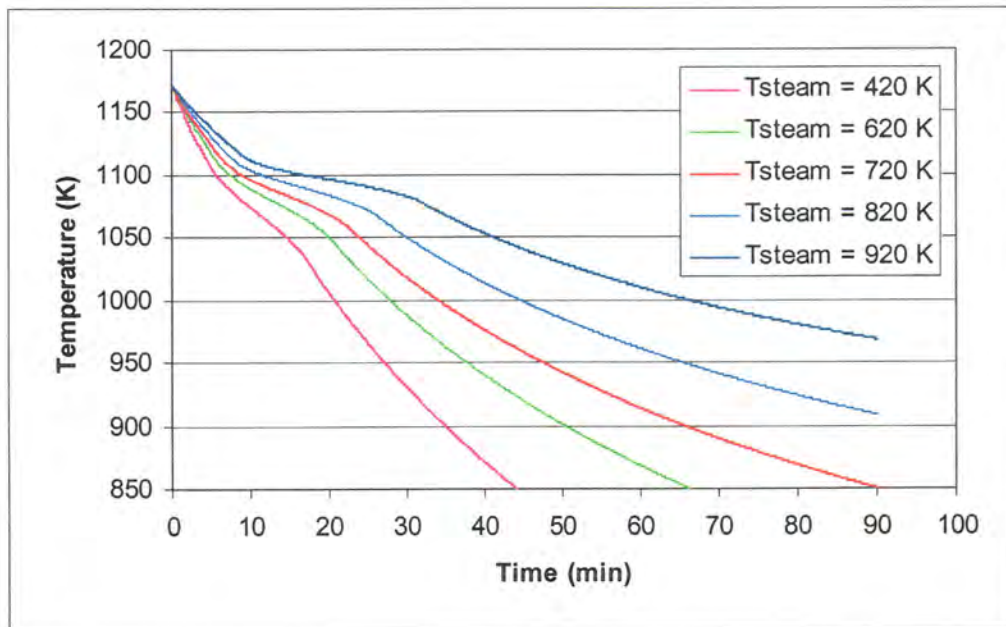


Figure 4.7—Bed temperature profiles for varied values of T_{steam}

By examining the profiles for various steam inlet temperatures, the variations can be quantified. The variation of cooling time as a function of inlet steam temperature is illustrated in Figure 4.8. For a steam inlet temperature of 720 K, the time required for the bed to reach 900 K is approximately 65 minutes. If the steam inlet temperature is increased to 820 K, the bed temperature remains above 900 K even after 90 minutes. On the other hand, if the steam inlet temperature is decreased to 620 K, the bed temperature reaches 900 K after only 50 minutes of cooling. If the steam inlet temperature is further decreased to 420 K, the time required to cool the bed to 900 K is only 35 minutes, a reduction of 46% compared to the cooling time with an inlet steam temperature of 720 K.

The relative importance of the amount of insulation surrounding the fluidized bed, the volumetric flowrate of the purge gas and the temperature at which the fluidizing medium enters the reactor can be discerned by examining Figure 4.4, Figure 4.6 and Figure 4.8. These figures illustrate the practical limits of the variables in question. Practical variations of thermal conductivity of blanket insulation and purge gas flowrate cause variations in cooling time from 50 to 70 minutes, while variations in steam inlet temperature can lead to cooling times ranging from 35 to 90 minutes. Thus, the inlet temperature of the fluidizing medium is of greater importance to reactor behavior than the amount of external insulation surrounding the ballasted gasification reactor and the purge gas flowrate, although these latter two variables are still significant.

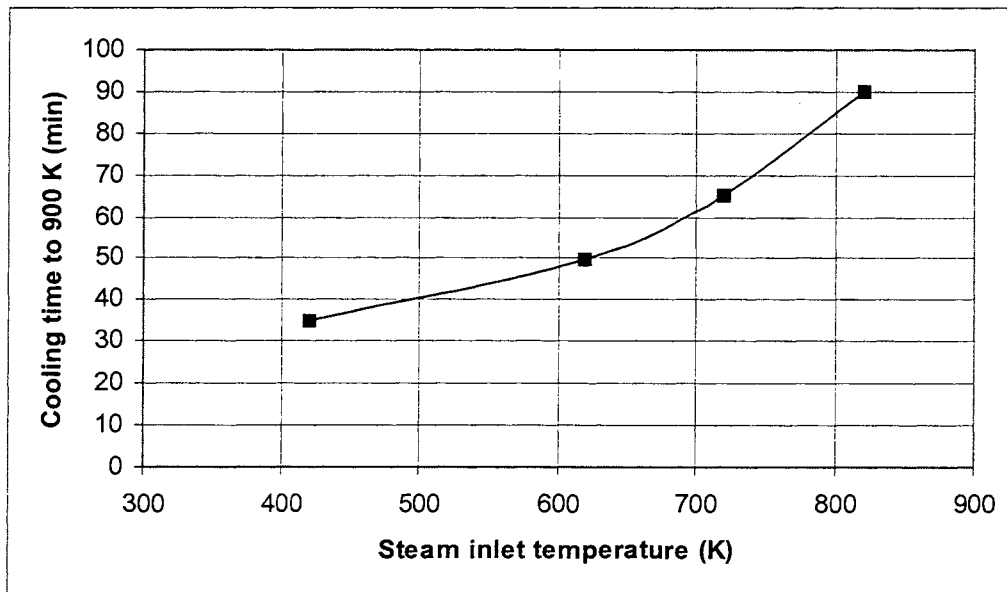


Figure 4.8—Variation in reactor cooling time as a function of T_{steam}

4.2.4 Mass of phase-change material per tube

As mentioned in Section 2.5, the length of time an ideal ballasted reactor would remain in isothermal operation is dependent upon the mass of phase-change material contained within the bed, m_{pc} , as well as the latent heat of fusion of the phase-change material, $h_{pc,fus}$, and the rate at which energy is withdrawn from the bed. In the case of steam cooling, that rate is equal to the rate of heat transfer from the bed to the steam described above, \dot{Q}_{steam} . While in practice the fluidized bed never operates in an isothermal mode, the effect of the phase-change is seen as a period during which the rate of change of the bed temperature approaches zero. Two inflection points bound this period, and the time between these points can be defined as the phase-change time, t_{pc} , and the following equation can be written:

$$t_{pc} \approx \frac{m_{pc} \cdot h_{pc,fus}}{\dot{Q}_{steam}}. \quad (4.4)$$

The intended purpose of a thermal ballast is to extend this period of minimal bed temperature loss to the greatest extent possible. The latent heat of fusion is fixed for a given phase-change material, so the only way to increase t_{pc} for a given \dot{Q}_{steam} is to increase the mass of phase-change material contained within the bed, m_{pc} . There were 48 ballast tubes employed in the ballasted gasifier containing 0.3 kg (0.66 lb) of lithium fluoride per tube, so the total mass of phase-change material was approximately 14.4 kg (31.7 lb). If an additional 0.13 kg (0.29 lb) of lithium fluoride were added to the tubes, the total amount of phase-change material would then increase to 20.9 kg (45.9 lb). An analysis was performed to determine the effects of this additional phase-change material. The resulting bed temperature profiles for this analysis are shown in Figure 4.9.

The phase-change time, t_{pc} , expected for the reactor containing 14.4 kg of lithium fluoride can be estimated by estimating the heat transfer rate, \dot{Q}_{steam} , during the phase-change process. For a steam mass flowrate of 90.3 kg/hr (199 lb/hr) at an inlet temperature of 720 K (837°F), \dot{Q}_{steam} would have a value of approximately 79,600 kW. The latent heat of fusion of LiF, $h_{pc,fus}$, has a value of 1050 kJ/kg. Thus, for a reactor containing 14.4 kg of lithium fluoride, the phase-change time, t_{pc} , would be approximately 0.190 hours, or 11.4 minutes. For a reactor containing 20.9 kg of lithium fluoride, this time increases to approximately 0.275 hours, or 16.5 minutes. From Figure 4.9, this time between the inflection points of the profile is approximately

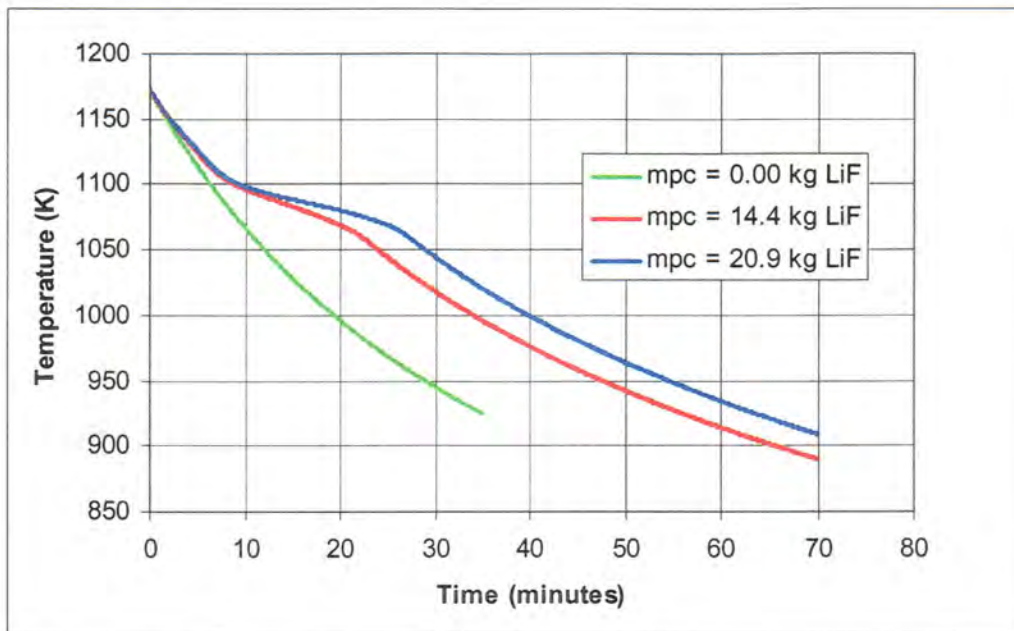


Figure 4.9—Bed temperature profiles for varied values of m_{pc}

13 minutes for a reactor containing 14.4 kg of phase-change material and approximately 18 minutes for a reactor containing 20.9 kg of phase-change material.

While the actual times are slightly longer than the estimates due to the inhibition of heat transfer, the additional phase-change material increases the phase-change time approximately 5 minutes in both the estimated and actual times. This increase in time remains throughout the entire temperature profile. The inhibition of heat transfer affects the rate at which thermal energy enters the fluidized bed from the ballast tubes but has very little effect on the ability of the phase-change material to lengthen cooling times of the reactor. The variations in reactor cooling time as the mass of lithium fluoride within the reactor is varied is shown in Figure 4.10. The correlation between reactor cooling time and mass of phase-change material appears linear, although there are only 3 cases considered in this analysis. Based on this apparent linearity, the effect of a given amount of lithium fluoride within the reactor should be able to be estimated by Equation 4.4.

4.2.5 Thermal conductivity of lithium fluoride

As conduction through the solidified phase-change material plays a significant role in the heat transfer process between the bed and the ballast tubes during phase-change, the thermal conductivity of the lithium fluoride was believed to be a critical parameter of the system.

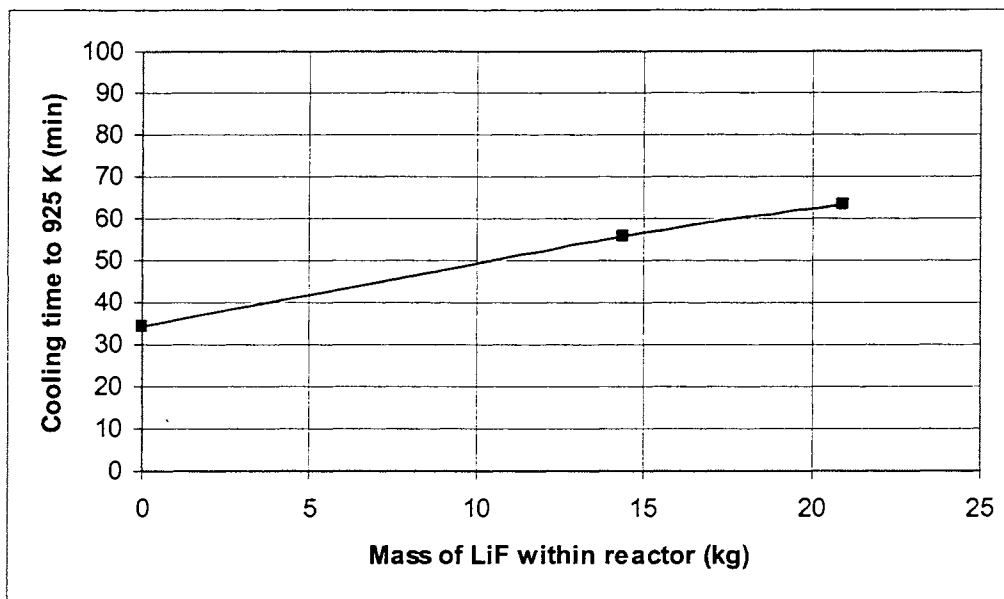


Figure 4.10—Variation in reactor cooling time as a function of m_{pc}

However, precise values of thermal conductivity were difficult to obtain for lithium fluoride. Tabulated data on a variety of phase-change materials listed the thermal conductivity of lithium fluoride in the range of 2.0-4.0 W/m-K [8]. A value of 4.0 W/m-K was assumed for the solid-phase thermal conductivity of lithium fluoride, k_{LiF} , during the modeling work conducted. A second source was found following the completion of a great deal of the modeling work, providing evidence that the thermal conductivity ranges from 6.0 W/m-K at temperatures of 500 K to 3.0 W/m-K at temperatures of 1100 K [41]. Therefore, a sensitivity analysis was performed to determine the effects of this range of thermal conductivity values. The resulting bed temperature profiles are displayed in Figure 4.11.

Slight variations exist during the phase-change period as the thermal conductivity of lithium fluoride ranges from 3.0 W/m-K to 6.0 W/m-K. When the value of k_{LiF} is 6.0 W/m-K, the bed temperature remains at approximately 1070 K at the end of the phase-change process, while the bed temperature remains at approximately 1060 K at the end of the phase-change process when the value of k_{LiF} is 3.0 W/m-K. The phase-change time, t_{pc} , defined again as the time between inflection points of the bed temperature profile, varies from approximately 11 minutes when k_{LiF} is 6.0 W/m-K to 13 minutes when k_{LiF} is 3.0 W/m-K. Unlike the profiles for various values of m_{pc} , the effects seen during the phase-change process do not carry through the

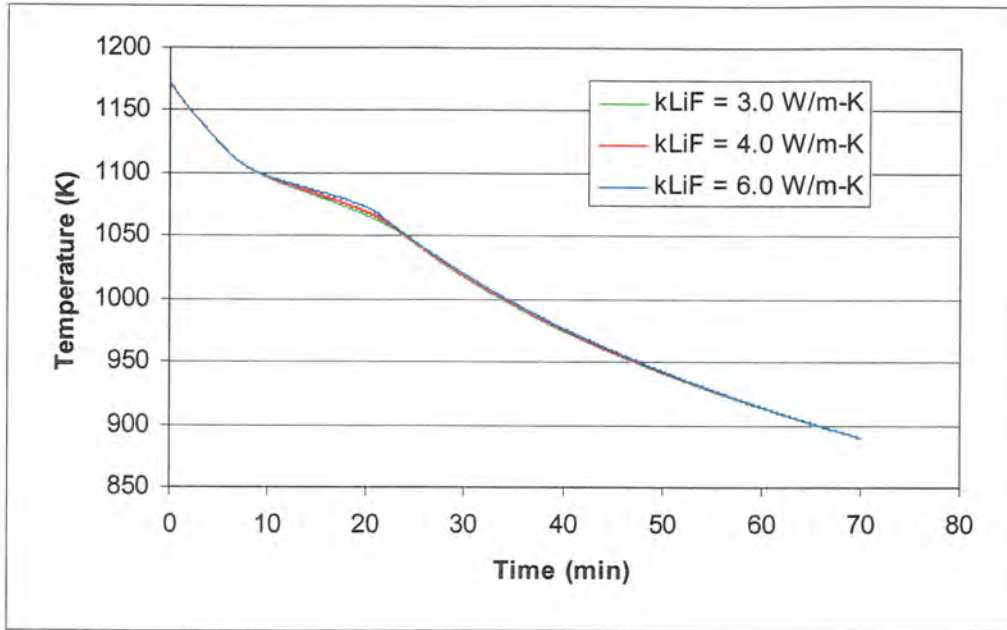


Figure 4.11—Bed temperature profiles for varied values of k_{LiF}

remainder of the period, as the profiles converge quickly following the end of the phase-change process. Thus, the value of k_{LiF} has virtually no impact upon the overall reactor behavior, particularly within the realistic range of 3.0-6.0 W/m-K. The variation due to thermal conductivity of the phase-change material would become more significant if the phase-change period constituted a greater portion of the overall process.

4.2.6 Characteristic dimension of the ballast

Behavior of a transient heat transfer process of a given element is heavily influenced by the Biot number of the element, Bi , which is a ratio of convective thermal resistance and conductive thermal resistance [40]:

$$Bi = \frac{h \cdot L_c}{k}, \quad (4.5)$$

where h is the convection heat transfer coefficient at the outer surface of the element, k is the thermal conductivity within the element, and L_c is the characteristic dimension of the element.

The characteristic dimension is defined as the ratio of volume, V , and surface area, A_{surf} [40]:

$$L_c = \frac{V}{A_{surf}}. \quad (4.6)$$

For long cylinders, such as the ballast tubes, the characteristic dimension is equal to half the radius or one quarter of the diameter:

$$L_c = \frac{r_{tube}}{2} = \frac{d_{tube}}{4}. \quad (4.7)$$

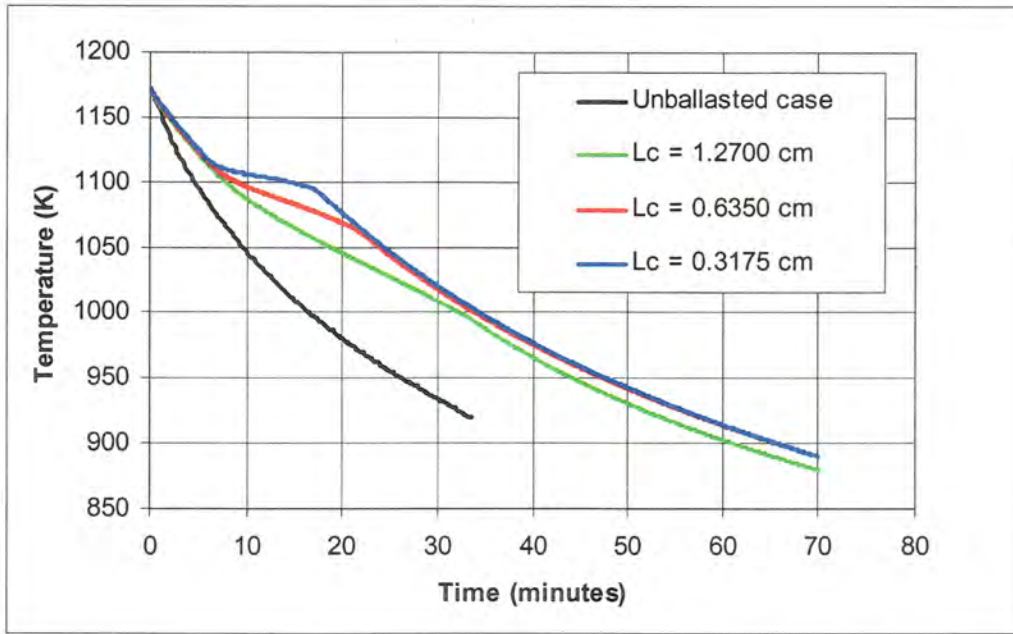
As the convection coefficient of the fluidized bed and the thermal conductivity within the ballast tube are relatively fixed, the only means of altering Bi is to alter the characteristic dimension of the tubes. The actual diameter of the tubes was 2.54 cm (1.0 in.), and so a sensitivity analysis was performed considering ballast tube diameters of 1.27 cm (0.5 in.), 2.54 cm (1.0 in.) and 5.08 cm (2.0 in.). In order to keep the amount of phase-change material constant across the various cases, however, the number of tubes and amount of lithium fluoride per tube was adjusted accordingly. The values of the parameters of this analysis are compiled in Table 4.2. The resulting fluidized bed temperature profiles are illustrated in Figure 4.12. The unballasted case has been included on Figure 4.12 to establish a baseline case.

The Biot number of each case can be estimated by assuming a convection coefficient, h , with a value of 300 W/m²-K and a thermal conductivity, k , with a value of 4 W/m-K. For the case in which $L_c=0.635$ cm, the Biot number is 0.476. For the cases of $L_c=0.318$ cm and $L_c=1.27$ cm, the Biot number is 0.238 and 0.953, respectively. According to theory, the element can be considered a lumped capacitance and temperature gradients within the element are negligible when the Biot number is less than 0.1. This is not the case in any of the values of characteristic dimension considered in this analysis, and thus, temperature gradients within the ballast tubes are significant in all cases.

The value of the characteristic dimension, L_c , has a tremendous impact on reactor behavior during the phase-change process, although the effect is less dramatic following this period. Regardless of the magnitude of the characteristic dimension, it is clear that the thermal ballast offers significant benefit over the unballasted case. However, it is clear that as the characteristic dimension decreases, the temperature profile behaves in a manner that is increasingly closer to ideal. When $L_c=1.27$ cm, it is difficult at first glance to identify the inflection points that delineate the onset and conclusion of the phase-change process, while when $L_c=0.318$ cm, the phase-change process occurs across a very narrow temperature range of

Table 4.2—Parameters examined in sensitivity analysis of L_c

Case no.	L_c (cm)	d_{tube} (cm)	n_{tubes}	$m_{pc,tube}$ (kg)	$m_{pc,total}$ (kg)	Biot no.
1	0.3175	1.27	192	0.075	14.4	0.238
2	0.6250	2.54	48	0.300	14.4	0.476
3	1.2700	5.08	12	1.200	14.4	0.953

**Figure 4.12—Bed temperature profiles for varied values of L_c**

approximately 10 K. The fluidized bed reaches a temperature of 900 K at approximately the same time in all cases, but if near-isothermal behavior is desired during the phase-change process, the characteristic dimension of the phase-change containment units should be minimized.

4.2.7 Potential enhancement of the thermal ballast

Certain aspects of the thermal ballast were also shown to be critical through sensitivity analyses. Any increase in mass of phase-change material within the fluidized increased the length of the phase-change period, and this effect remained throughout the entire cooling period. The characteristic dimension also proved to be a key parameter. As the characteristic dimension was reduced, the bed approached a more ideal behavior. Should both of these parameters be able to be optimized simultaneously, the potential may exist to operate the cycle within a fairly narrow

temperature range, which would lead to higher average temperatures in the bed, greater consistency in the producer gas and less thermal shock transferred to the reactor and ballast tubes.

One method of increasing the amount of phase-change material within the reactor would be to lengthen the currently-employed ballast tubes. As noted by Pletka [8], the solidified lithium fluoride resides in the bottom half of the reactor. The longer tubes would extend out of the sand bed, while all of the phase-change material should still reside below the surface of the fluidized bed, as illustrated in Figure 4.13. If the ballast tubes were lengthened to 106.7 cm (42.0 in.), the amount of phase-change material contained within the tubes could be increased to 0.7 kg (1.54 lb) per tube. Calculations were performed to ensure that internal pressures would need exceed the material limitations of the tubes, and these calculations are shown in Appendix C. The increased mass of lithium fluoride would result in a phase-change period of approximately 30 minutes during steam cooling. This increase could be achieved with no effect to characteristic dimension of the tubes or fluidized bed dynamics. As the longer tubes would be slightly more prone to warping, the tubes may have to be designed with an increased wall thickness. As the thermal conductivity of stainless steel is relatively high, this increased thickness should not significantly affect heat transfer processes between the tubes and the fluidized bed.

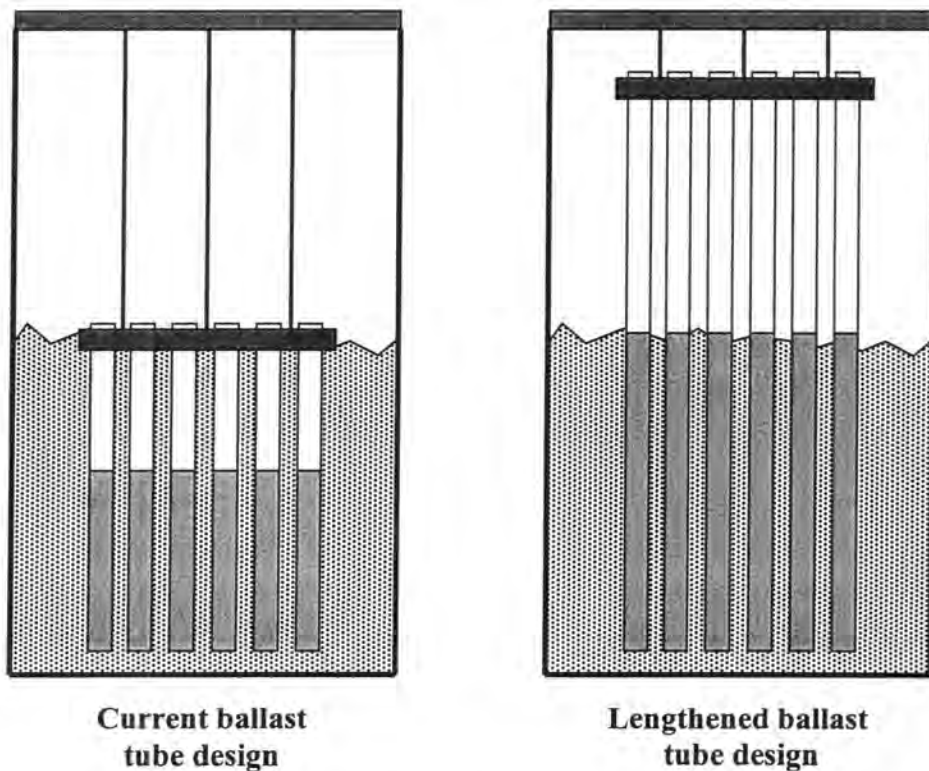


Figure 4.13—Comparison of current and lengthened ballast tube design

A second design would alter the characteristic dimension of the thermal ballast. This ballast would be composed of large hexagonal annuli clustered in a honeycomb fashion, illustrated in Figure 4.14. The honeycomb ballast would then be inserted into the reactor. This ballast design would require thin walls to minimize the space occupied by the insert and maximize the amount of phase-change material stored within the walls of the annuli. The annuli could have a length equal to that of the tubes used in the conventional ballast, but the inner diameter of the annulus must be large enough to allow fluidization within it. Feeding biomass to each annulus would be difficult, however. If the fluidized bed were deep enough, biomass could be fed into a mixing region below the ballast, which could theoretically deliver the feedstock to each annulus (see Figure 4.15). If the bed were fluidized on the inside and outside of each annulus, the characteristic dimension of this design would one-half of the distance between the inner and outer annulus wall.

4.3 Experimental results

In order to characterize the operation of the ballasted gasification cycle in a fluidized bed, experiments were carried out at the BECON Facility. Two sets of tests were conducted during this research. The first set of tests consisted of steam cooling tests, in which no biomass was fed to the reactor, while the second consisted of ballasted gasification tests. The purpose of the steam cooling testing was to obtain bed temperature profiles during the cooling period to compare to model predictions. While this task was also accomplished during the ballasted gasification testing, the purpose of the ballasted gasification testing was to obtain time-resolved gas composition profiles throughout the pyrolysis phase. All tests were executed with ballast tubes

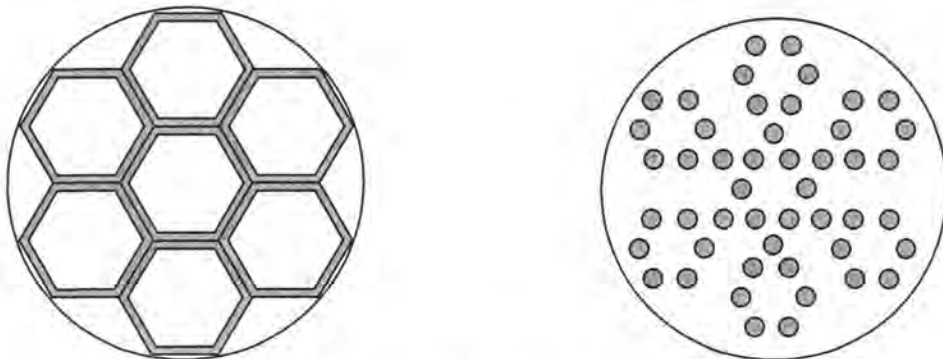


Figure 4.14—Comparison of honeycomb ballast and tube ballast

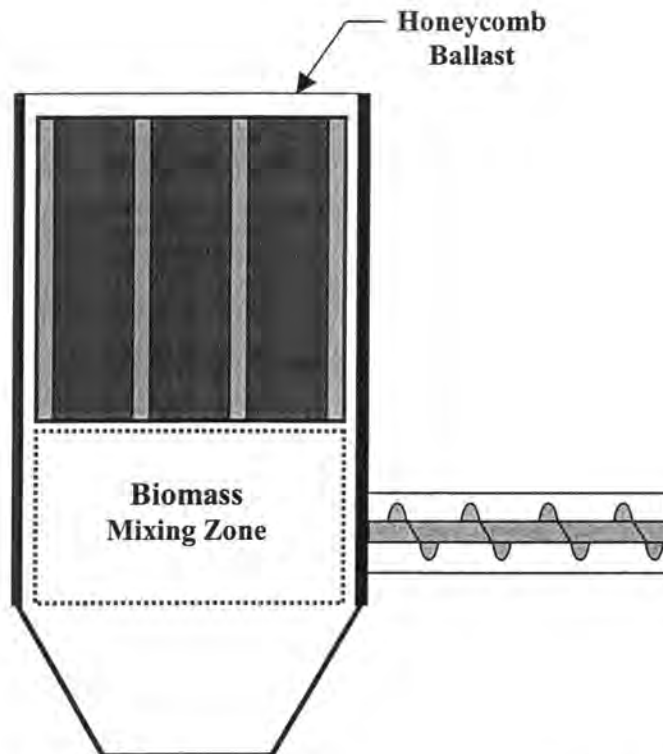


Figure 4.15—Illustration of biomass mixing zone within fluidized bed

present in the reactor. Time limitations precluded operating the cycle without ballast tubes within the reactor.

4.3.1 Reactor cooling time and cooling temperature profiles

The purpose of the latent-heat ballast is to increase the energy stored within the bed and allow a greater quantity of biomass to be processed during the pyrolysis phase of ballasted gasification. The additional advantage of the latent-heat ballast is to increase the average bed temperature during the pyrolysis period. The extent to which this temperature is increased can be determined by examining the temperature profiles during the phase. Reactor cooling time and temperature profiles were obtained for both steam cooling tests, in which no biomass was fed to the reactor, and the pyrolysis phase of ballasted gasification.

4.3.1.1 Steam cooling tests

The purpose of the steam cooling tests is to provide experimental data to verify the bed temperature profiles predicted by the RI model for the current ballasted gasification system. The heat transfer processes that occur within the reactor during pyrolysis are greatly complicated by

the chemical energy absorbed and released as the multiple chemical reactions associated with pyrolysis proceed. This complex chemistry is not well understood, and to better understand the heat transfer processes not associated with pyrolysis chemistry, cooling tests were performed without feeding biomass into the reactor. With the chemical processes removed, all heat loss was attributed to one of three sinks: heat loss to fluidizing steam, heat loss to purge gas and heat loss through the composite wall.

Five steam cooling tests were performed. The steam flowrate was held constant at 90.9 kg/hr (200 lb/hr) for the first three of these tests, while the steam flowrate was adjusted to 100 kg/hr (220 lb/hr) and 81.8 kg/hr (180 lb/hr) for the fourth and fifth tests, respectively. The purge gas flowrate was set to 30.6 Nm³/hr (18 SCFM). The resulting bed temperature profiles during the steam cooling tests are shown in Figure 4.16. The bed temperature profile was determined by averaging the measurements of the ten thermocouples placed within the fluidized bed.

The results fall in the order that one would expect, with cooling times decreasing as steam flowrate is increased, with the exception of the first test performed at a steam flowrate of 90.9 kg/hr. This test was the first test performed upon the completion of the start up process, and the reactor may not have yet reached quasi-steady state operation. The temperature profiles of the remaining runs completed at a steam flowrate of 90.9 kg/hr lie virtually on top of one another, so disregarding the first run during analysis is justified. Surprisingly little variation exists as the

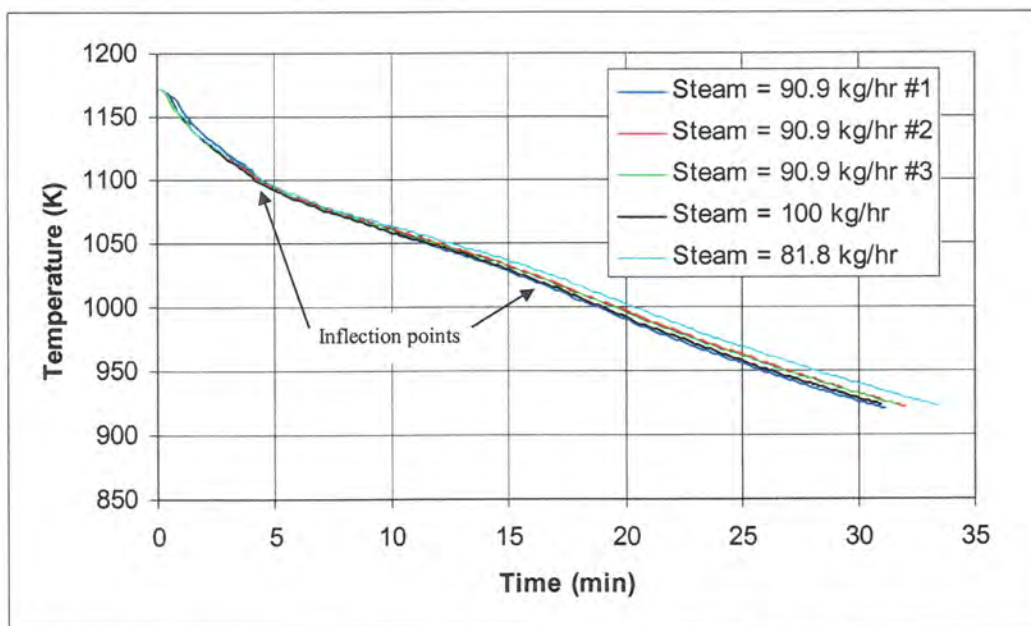


Figure 4.16—Bed temperature profiles during steam cooling for various steam flowrates

steam flowrate is adjusted. The time required for the average bed temperature to fall from 1172 K (1650°F) to 922 K (1200°F) is 31.8 minutes when the steam flowrate was 90.9 kg/hr. This time increased only 1.5 minutes to 33.3 minutes when the steam flowrate was reduced to 81.8 kg/hr, while it decreased just 0.8 minutes to 31.0 minutes when the steam flowrate was increased to 100 kg/hr. This lack of variation suggests that losses through the wall and losses due to the heating of cold purge gas are on the same order of magnitude as the losses due to the heating of the steam during the cooling period.

The RI model predictions of the bed temperature profile were compared to steam cooling test data for all three steam flowrates. The results of the modeling of the steam cooling test with a flowrate of 81.8 kg/hr (180 lb/hr) are shown in Figure 4.17, while results from steam cooling tests with steam flowrates of 90.9 kg/hr (200 lb/hr) and 100 kg/hr (220 lb/hr) are illustrated in Figure 4.18 and Figure 4.19, respectively.

From the graphs, the model follows the behavior of the fluidized bed fairly well during the steam cooling periods. Further, the model shows the same slight variation in cooling time that was seen in experimental data. The model showed the ability to predict bed temperatures within 30 K, when bed temperatures were on the order of 1000 K, an error of less than 3% of the absolute temperature. The errors seen in the RI model predictions for the present system are greater than those seen for the previous system (see Figure 4.2), but it is reasonable considering the uncertainties in the purge gas flowrate and the increased heat loss through the wall of the present gasifier.

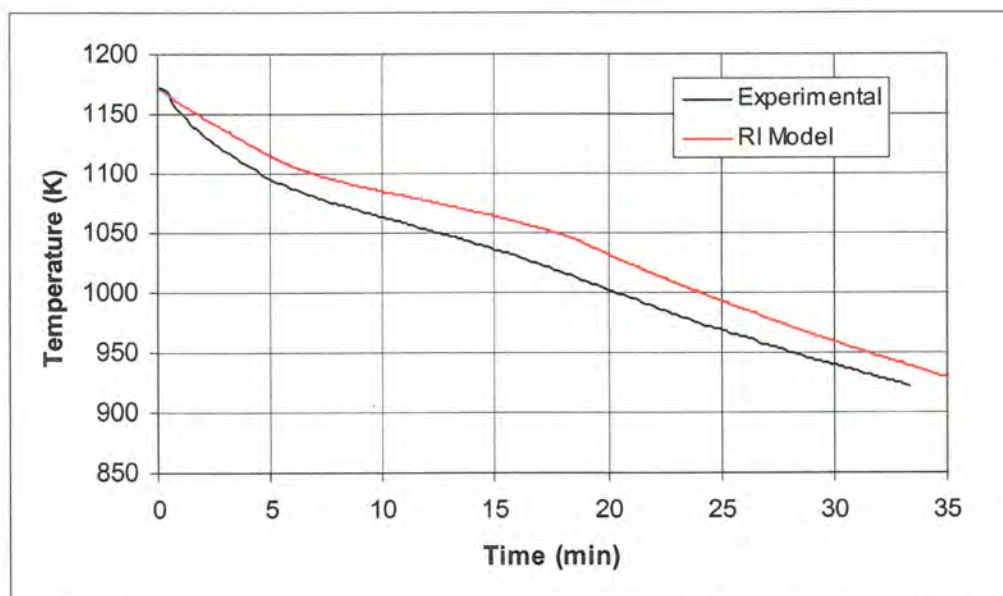


Figure 4.17—Bed temperature profiles during steam cooling tests (flowrate = 81.8 kg/hr)

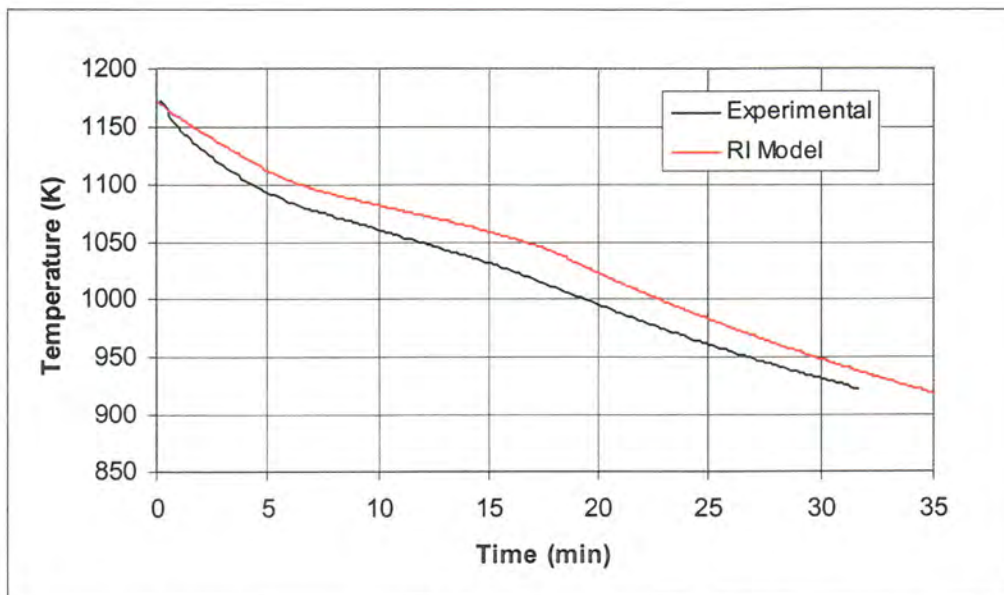


Figure 4.18—Bed temperature profiles during steam cooling tests (flowrate = 90.9 kg/hr)

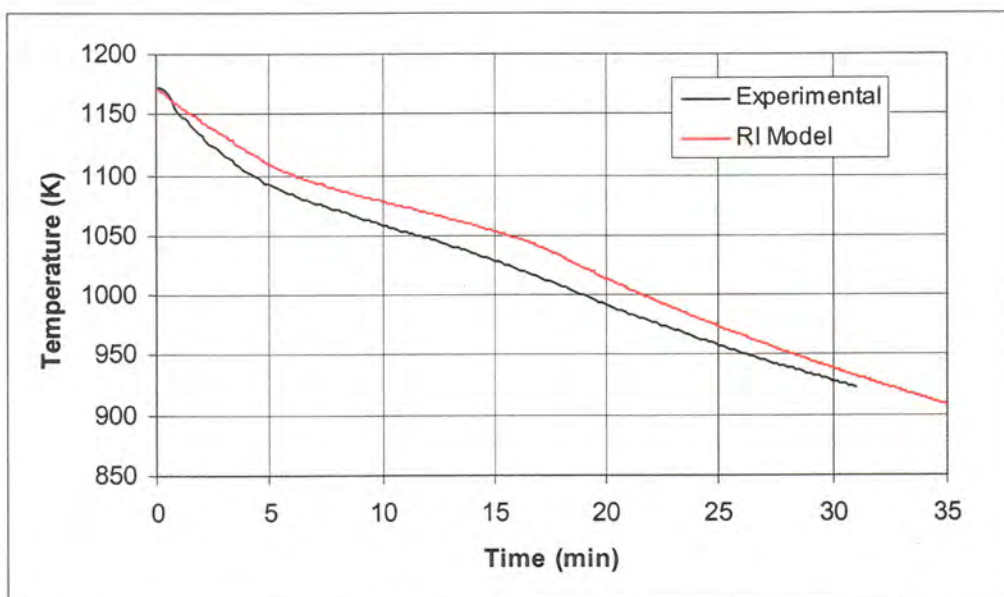


Figure 4.19—Bed temperature profiles during steam cooling tests (flowrate = 100.0 kg/hr)

4.3.1.2 Pyrolysis tests

In order to determine the bed temperature profiles during the pyrolysis of biomass, temperature data was recorded during the pyrolysis phase of the ballasted gasification cycle. The fluidized bed reactor was operated for five complete cycles. The feedstock used for these tests was corn. The biomass feedrate and steam flowrate were set to 181.8 kg/hr (400 lb/hr) and 90.9

kg/hr (200 lb/hr), respectively. The purge gas flowrate was set to 23.8 Nm³/hr (14 SCFM). The resulting bed temperature profiles during the steam cooling tests are shown in Figure 4.20. Again, the bed temperature profile was determined by averaging the measurements of the ten thermocouples placed within the fluidized bed.

As the operating parameters were not altered during the experiment, little deviation is expected in the bed temperature profiles, and this is indeed the behavior seen in the experimental data. At any given time during the pyrolysis phase, the profiles of the five cycles varied less than 10 K (while actual temperatures were on the order of 1000 K). The time required for the bed to cool from 1172 K (1650°F) to 922 K (1200°F) ranged from 9.5 minutes to 9.8 minutes, a difference of about 20 seconds. This lack of variation indicates a consistent behavior of the entire system from cycle to cycle.

While the bed temperature profiles obtained during steam cooling tests contain two relatively clear inflection points indicating the onset and conclusion of the phase-change period, the profiles obtained during pyrolysis testing contains no clear inflection points corresponding to the onset and completion of the phase-change period. As discussed in Section 2.5, ideal behavior is seen only when the thermal energy losses from the fluidized bed are balanced by the transfer of thermal energy from the ballast tubes. Compared to the rate of energy

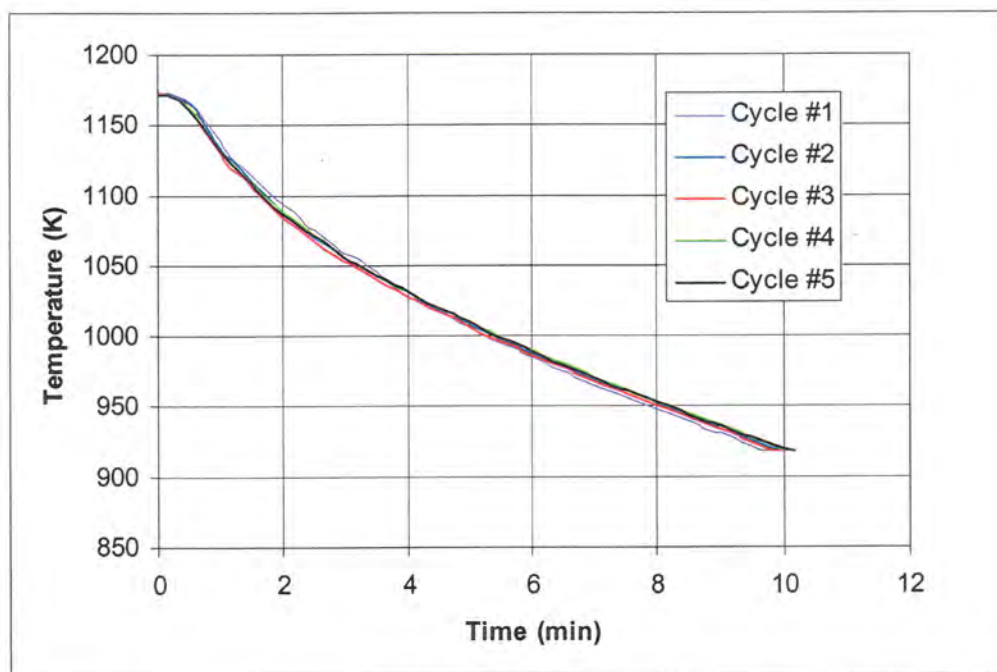


Figure 4.20—Bed temperature profiles during pyrolysis phase of ballasted gasification

loss during steam cooling, the endothermic chemical processes of pyrolysis greatly increase the rate of energy loss from the bed, while the heat transfer process from the tubes to the bed remains relatively unchanged. Thus, the bed behaves much less ideally during this period, and these non-ideal processes “hide” the inflection points that signal the beginning and end of the phase-change process.

Attempts to predict the bed temperature profiles through the pyrolysis phase of the ballasted gasification cycle cannot be done considering the physical heat transfer processes alone. The energy required by the chemical reactions that occur during the pyrolysis process is substantial. Previous research found that thermodynamic predictions of the producer gas composition are inaccurate as thermodynamic equilibrium is not achieved within the reactor. Thus, modeling of the bed temperature profiles cannot be accomplished until this chemical process has been characterized. This characterization must include a description of the gas composition and a quantification of the amount of gas produced. An attempt to achieve this characterization will be discussed in Section 4.3.3.

4.3.2 *Combustion temperature profiles*

While the products of the pyrolysis phase contain the desired fuel gases, consideration of the behavior of the fluidized bed during the combustion process is crucial when determining the ultimate efficiency of the system. Thus, data was also recorded during combustion phases of steam cooling tests and pyrolysis tests. The biomass feedrate during the combustion phase of both sets of tests was 150 kg/hr. During steam cooling testing, the air flowrate was 144.4 Nm³/hr (85 SCFM), and the purge gas flowrate was 30.6 Nm³/hr (18 SCFM). The resulting bed temperature profiles are illustrated in Figure 4.21. During pyrolysis testing, the air flowrate was 161.4 Nm³/hr (95 SCFM), and the purge gas flowrate was 23.8 Nm³/hr (14 SCFM). The bed temperature profiles from pyrolysis testing are shown in Figure 4.22. It is important to note that the air used to fluidize the bed during the combustion phase of both sets of tests was not pre-heated. Like the pyrolysis phase, the time required to complete the combustion period is consistent, with combustion times of approximately 29 minutes during steam cooling and approximately 27 minutes during pyrolysis tests.

The most prominent feature of the bed temperature profiles is the brief temperature plateau as the bed reached an average temperature near 1060 K (1450°F). This temperature is too low to cause the melting of lithium fluoride, and this effect is not attributable to char burnout as it is present during steam cooling tests, in which no char is produced. The calcination of limestone does occur at this temperature, but the repetition of this effect would indicate that limestone

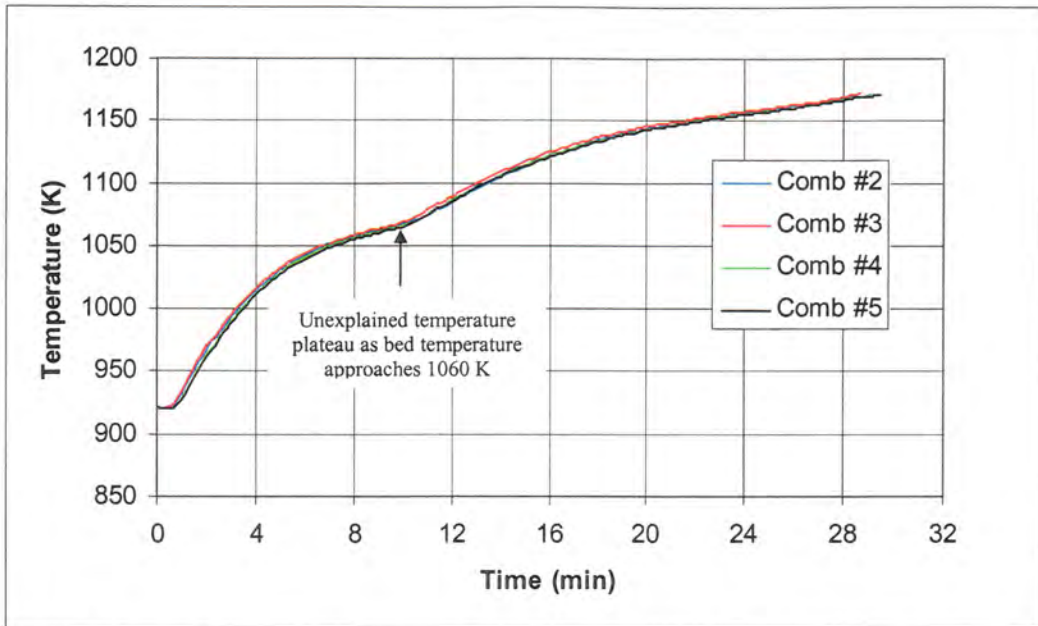


Figure 4.21—Bed temperature profiles during combustion phase of steam cooling tests

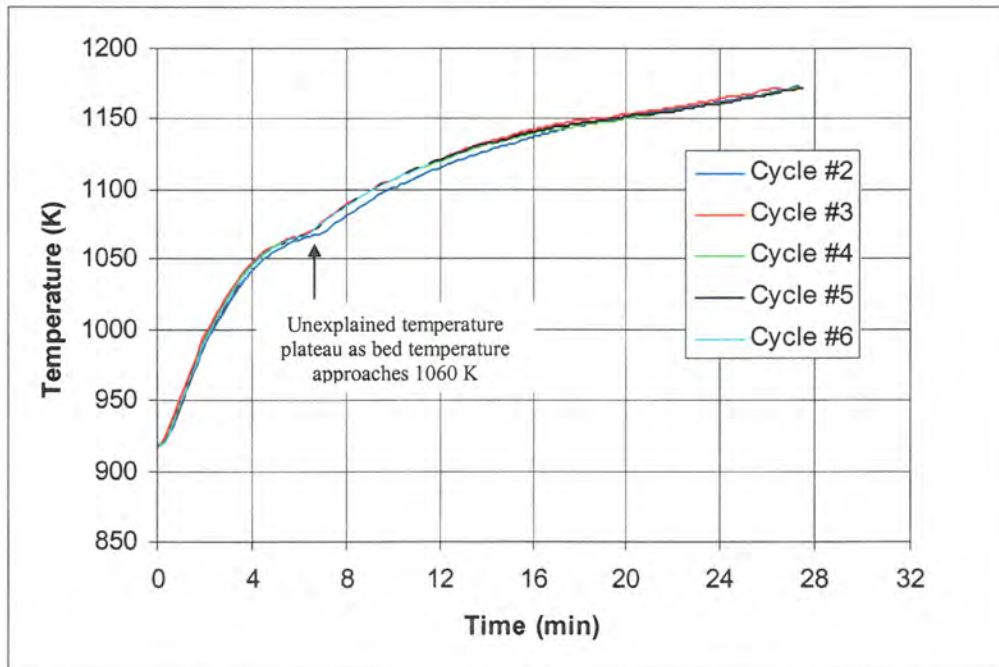


Figure 4.22—Bed temperature profiles during combustion phase of ballasted gasification

undergoes the reverse process during pyrolysis. Further investigation is required to determine the source of this phenomenon.

At first glance, it is difficult to identify the phase-change period during the combustion phase. If the temperature profiles are re-examined, focusing on the end of the combustion period,

the phase-change period becomes more evident. With the time scale changed to a range of 12-28 minutes and the temperature scale set to 1125-1175 K, inflection points become apparent at the approximate times of 18 minutes and 23 minutes, as depicted in Figure 4.23. As the phase-change temperature of lithium fluoride is 1121 K (1560°F), this is the portion of the combustion phase that one would expect the phase-change process to occur. The time required for the melting process is approximately 7 minutes, shorter than the solidification process during steam cooling tests. This shorter phase-change time is due to the large quantities of thermal energy provided by the combustion process.

4.3.3 Gas composition

As mentioned previously, characterization of the producer gas stream is essential to predicting the heat transfer processes within the reactor during pyrolysis. Thus, the primary goal of the ballasted gasification testing was the acquisition of gas composition profiles throughout the pyrolysis phase. One of the principal limitations of the previous research was the inability of gas analysis systems to continuously monitor the changes in the gas composition as the pyrolysis phase proceeds. Only time-averaged compositions could be determined, which did not accurately characterize the dynamic chemical processes that occur during the pyrolysis phase of ballasted gasification. This limitation was addressed, and continuous emission monitors were available

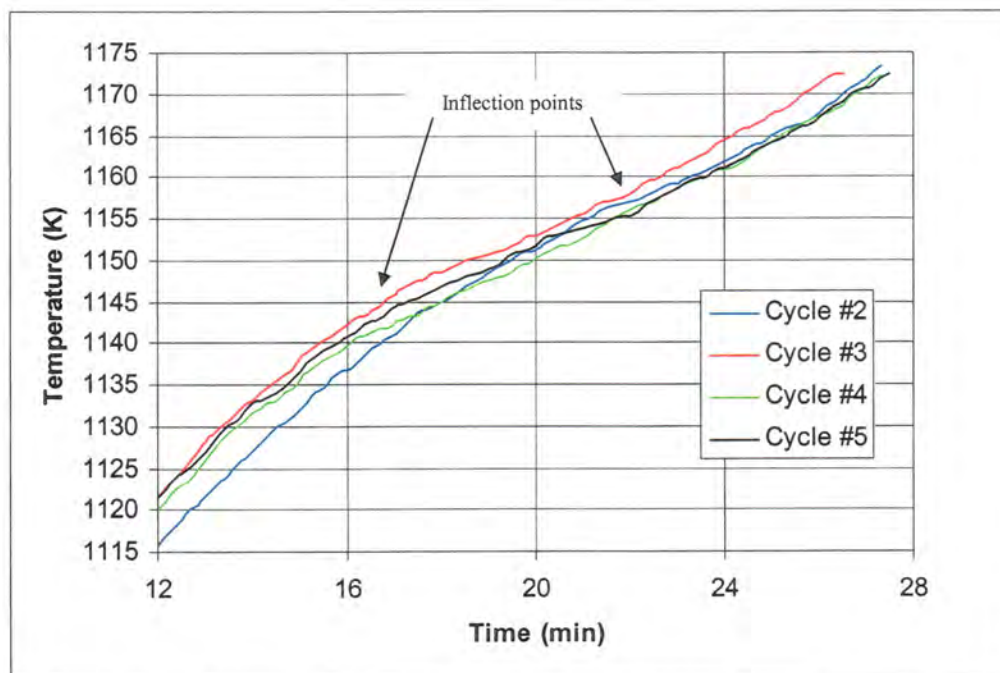


Figure 4.23—Bed temperature profiles illustrating phase-change during combustion

during the present study to continuously quantify the species of most interest: hydrogen and carbon monoxide. These continuous profiles were supplemented by intermittent determinations of other species within the gas matrix by a Micro-GC. Continuous emission monitors (CEM) quantified the content of the following gases: hydrogen (H_2), carbon monoxide (CO), carbon dioxide (CO_2) and oxygen (O_2). A Varian Micro-GC also determined the presence of these gases, as well as methane (CH_4), acetylene (C_2H_2) and ethylene (C_2H_4), ethane (C_2H_6), propane (C_3H_8) and nitrogen (N_2). All gas compositions were determined on a dry, tar-free basis. The CEM data throughout the testing period is illustrated in Figure 4.24.

One of the most striking features of Figure 4.24 is the repeatability of the gas composition through each phase of ballasted gasification, particularly for the final four cycles. During the first cycle, the H_2 content of the gas is about 2 vol-% lower during the initial minutes of the pyrolysis phase, while the peak of CO is a fraction of a percent higher than those of the ensuing cycles. Neglecting these small variations, the cycles are almost indistinguishable.

It is important to note that the composition of the producer gas varies significantly as the pyrolysis phase proceeds. This behavior can be seen clearly by examining the CEM data through one ballasted gasification cycle. The fourth cycle, which is the last cycle that was followed by a complete combustion phase, was chosen to illustrate these changes and is depicted in Figure 4.25.

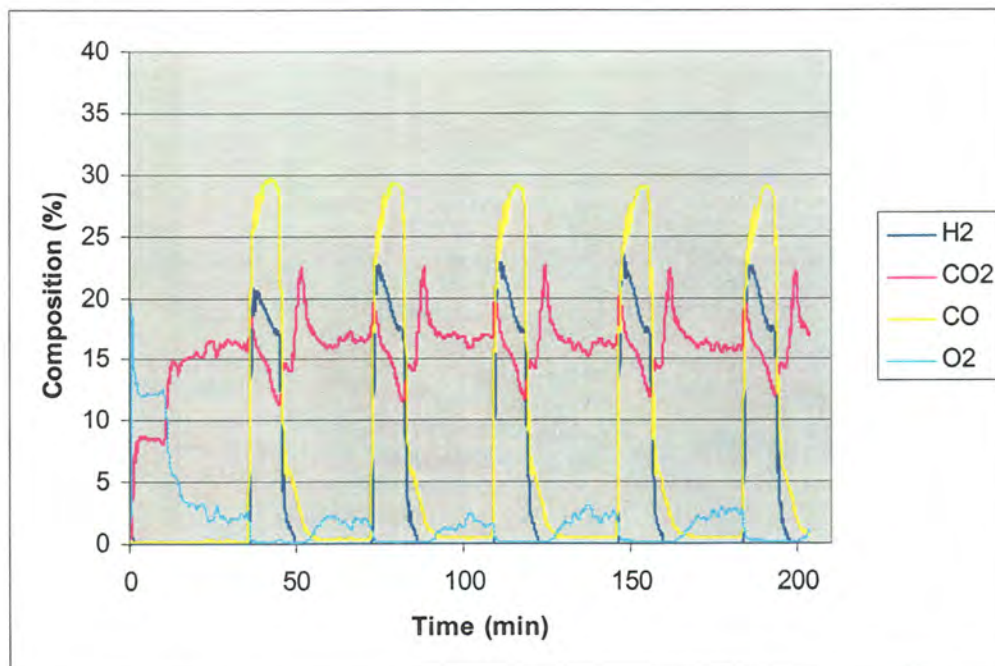


Figure 4.24—Raw gas composition as determined by CEM's during pyrolysis testing

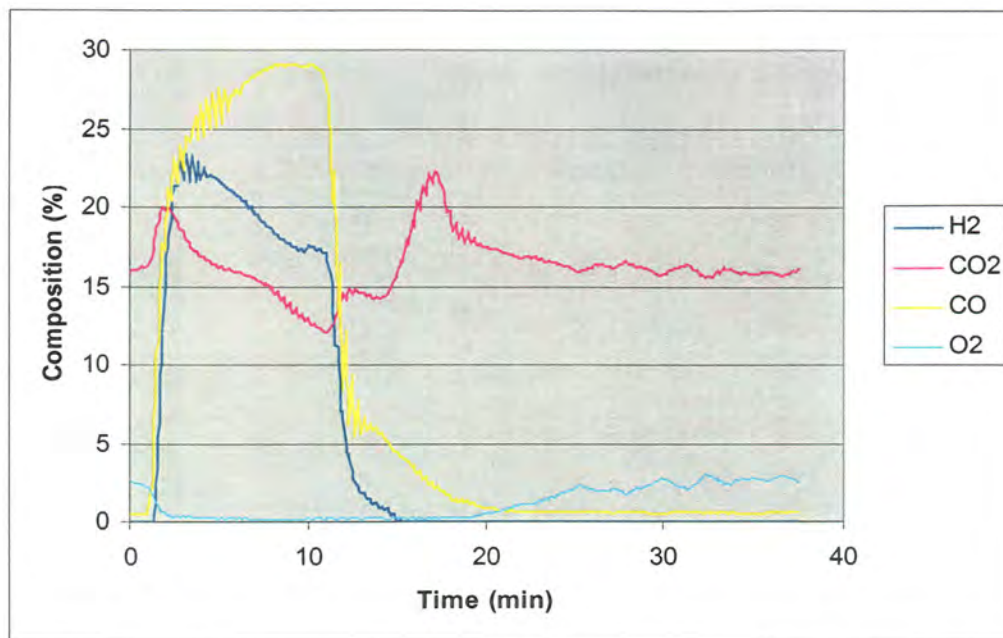


Figure 4.25—Raw gas composition as determined by CEM's during cycle #4

A short time delay of approximately 1.5 minutes exists from the time the pyrolysis conditions exist in the reactor until the sample gas reaches the CEM's, but it is apparent upon the switch from combustion to pyrolysis that the H₂ and CO concentrations rise dramatically. The initial composition contains equal parts of H₂ and CO, at approximately 22 vol-% of the total sample gas composition, and roughly 20 vol-% CO₂. The CO concentration increases throughout the cycle to nearly 29 vol-%, while H₂ and CO₂ concentrations decrease during this time to approximately 17 vol-% and 12 vol-%, respectively. As the pyrolysis phase ends and steam flow is ceased, air is reintroduced into the bed and a short period of char burnout commences. This char, produced during the pyrolysis phase, is incompletely combusted, as evidenced by the presence of a significant amount of CO and a small portion of H₂. As char burnout comes to completion, CO₂ production spikes. Following this spike, excess oxygen becomes evident and the combustion phase continues in a relatively stable fashion.

While only H₂, CO and CO₂ are monitored continuously during the pyrolysis, the Micro-GC data from several cycles can be manipulated to provide profiles of the other species present in the gas. Due to the time required by the Micro-GC to draw a sample and analyze the gas, only three to four measurements could be obtained during the pyrolysis phase of the cycle. However, the intermittent Micro-GC data can be superimposed upon the CEM data, which is done in Figure 4.26. Furthermore, the consistency of the CEM data from cycle to cycle allows the construction

of a composite graph illustrating the trend of Micro-GC data throughout the cycle, shown in Figure 4.27.

From the composite Micro-GC data, the patterns of the H_2 , CO and CO_2 are consistent with the CEM data. This provides evidence that the composite gas composition is accurate throughout the cycle and instills confidence in the measurements of gases not included in the CEM data: nitrogen (N_2); methane (CH_4); acetylene (C_2H_2) and ethylene (C_2H_4), which are measured together; ethane (C_2H_6) and propane (C_3H_8). Concentrations of CH_4 and the combination of C_2H_2 and C_2H_4 during the pyrolysis phase are approximately 10-12 vol-% and 4-5 vol-%, respectively, while N_2 concentrations range from 18-22 vol%.

The N_2 present in the producer gas does not arise from the pyrolysis of biomass, however. Reconsidering the ultimate analysis results shown in Table 3.4, fuel-borne nitrogen comprises a very small portion of the biomass fuel fed to the reactor. For seed corn, this value is approximately 1% by weight, or 0.6% on a molar basis. Thus, only a negligible amount of N_2 exists in the products of pyrolysis, and all N_2 present in the products of the steam pyrolysis process is assumed to originate from purge gas that passes through the reactor. This nitrogen is an undesirable product of the process and only serves to prevent the off-gassing of biomass within the feeding system prior to its insertion into the reactor. In principle, the feeding system could be designed to eliminate the need of purge gas, or recycled producer gas could be used in

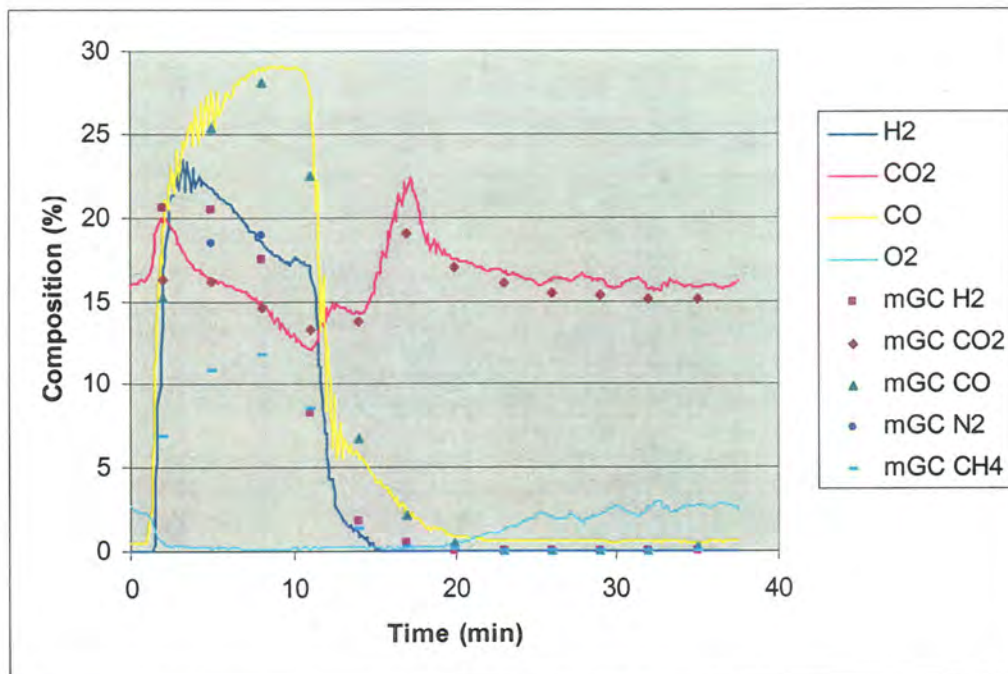


Figure 4.26—Cycle #4 CEM data with selected Micro-GC data superimposed

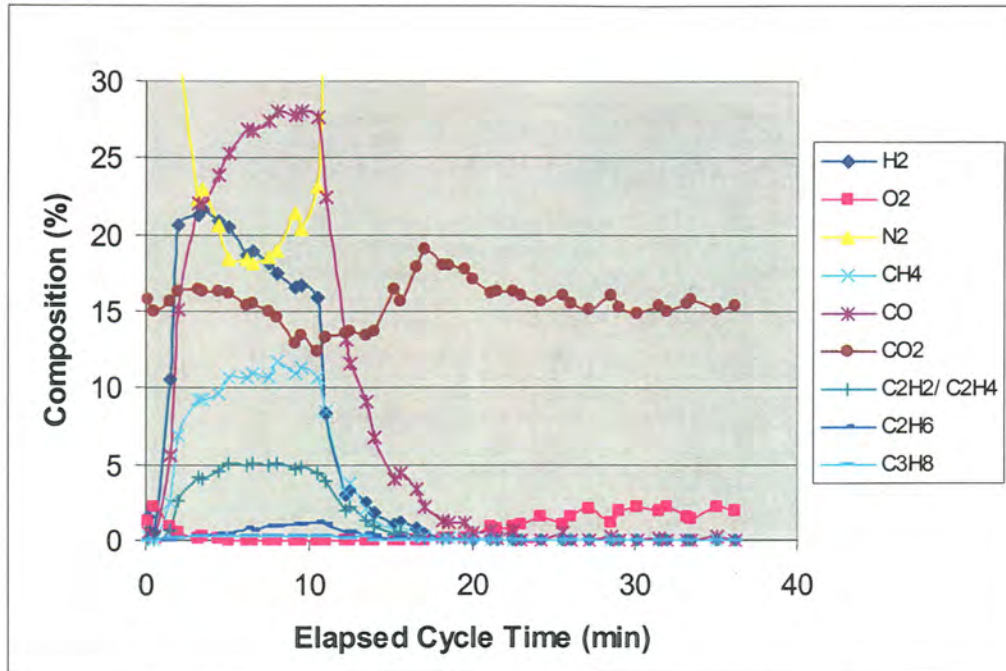


Figure 4.27—Composite of Micro-GC data during pyrolysis testing

this role. This would increase the heating value and hydrogen content of the gas. The current gas data was adjusted to remove the nitrogen from the producer gas composition. A comparison of the hydrogen content and heating value of each sample point for both the raw gas composition and the adjusted (0% N₂) composition is listed in Table 4.3, and Figure 4.28 illustrates the Micro-GC data adjusted to 0% N₂.

Table 4.3—Comparison of gas qualities for raw gas and gas adjusted to 0% N₂

Cycle Time (min)	Raw composition		Adjusted composition (0% N ₂)	
	H ₂ content (%)	HHV (kJ/Nm ³)	H ₂ content (%)	HHV (kJ/Nm ³)
2.00	20.61	8,600	31.18	13,000
3.17	21.27	11,500	27.39	14,800
3.50	21.61	11,500	28.04	14,900
4.50	20.87	12,200	26.27	15,300
5.00	20.46	13,000	25.06	15,900
6.17	18.71	13,100	22.92	16,100
6.50	18.96	13,300	23.17	16,200
7.50	18.11	13,200	22.24	16,200
8.00	17.44	13,700	21.50	16,800
9.17	16.54	13,100	21.03	16,700
9.50	16.73	13,400	21.00	16,800
10.50	15.91	12,800	20.69	16,600

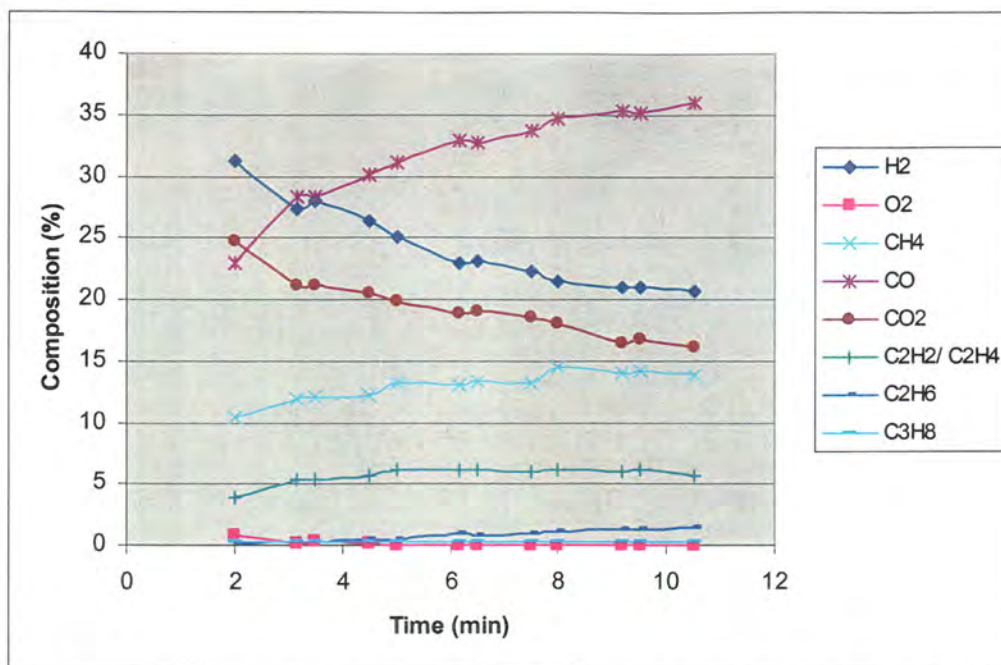


Figure 4.28—Composite of Micro-GC data during pyrolysis phase (adjusted to 0% N₂)

Although the hydrogen content of the producer gas decrease as temperature decreases during the pyrolysis cycle, this does not require the elevation of reactor operating temperatures to maximize hydrogen production. Catalytic cracking processes may be employed to convert hydrocarbons to additional hydrogen, and the water-gas shift reaction can be utilized to convert the abundant carbon monoxide and steam to hydrogen and carbon dioxide. Only if these processes prove inefficient or cost-prohibitive would reactor temperatures be required to increase in order to increase hydrogen content.

4.3.4 System efficiency considerations

As mentioned previously, the complete ballasted cycle, i.e. both the pyrolysis phase and the combustion phase, must be evaluated to determine the efficiency of the process. One means of quantifying the efficiency at which the system converts biomass into useful energy is to determine the ratio of the amount of biomass pyrolyzed to the total biomass fed to the reactor. The pyrolysis phase lasts 10.0 minutes at a biomass feedrate of 182 kg/hr (400 lb/hr), and the combustion phase requires 27.0 minutes to obtain the prescribed temperature. The length of the pyrolysis period is reasonable when compared to previous experiments. In previous testing conducted on a reactor located at the Biofuels Facility at Iowa State University [8], the reactor was able to remain in the pyrolysis phase for 10.5 to 14.3 minutes for biomass feedrates ranging from 159 kg/hr (350 lb/hr) to 113 kg/hr (250 lb/hr). However, the length of the combustion phase

during these tests was constant at 12.5 minutes. The process times for the previous tests and the test conducted during the current study are listed in Table 4.4. A comparison of the fraction of fuel pyrolyzed is listed in Table 4.5. Less than half of the fuel fed to the previous reactor is pyrolyzed, which obviously results in a poor efficiency of the system when compared to the previous trials.

The difference in combustion times can be attributed to four factors: the differences in refractory and insulation thicknesses of the reactors (listed in Table 4.6); the lack of a char combustion period during present testing; the low inlet temperature of the combustion air during the present study; and the additional purge gas required by fuel feeding system of the present reactor. Based on the sensitivity analyses developed earlier and experience with the system, all of these factors are significant.

The thickness of refractory and insulation within the reactor has two significant effects with respect to the length of time required to raise the temperature of the reactor. First, the lack of external insulation on the present reactor increases thermal losses through the wall when

Table 4.4—Comparison of ballasted gasification cycle times

Reactor	Pyrolysis		Process time (min)			
	fuel flow rate (kg/hr)	Char comb.	Biomass comb.	Total comb.	Pyrolysis	Cycle total
Biofuels Fac.	91	3.5	9.0	12.5	14.3	26.8
Biofuels Fac.	113	3.5	9.0	12.5	12.8	25.3
Biofuels Fac.	136	3.5	9.0	12.5	11.3	24.0
Biofuels Fac.	159	3.5	9.0	12.5	10.5	23.0
BECON	182	—	27.0	27.0	10.0	37.0

Table 4.5—Comparison of the fraction of fuel pyrolyzed

Reactor	Pyrolysis fuel flow rate (kg/hr)	Cycles per hour	Total fuel combusted (kg/hr)	Total fuel pyrolyzed (kg/hr)	Fuel fraction pyrolyzed
Biofuels Fac.	91	2.2	15.3	48.4	0.76
Biofuels Fac.	113	2.4	16.1	57.4	0.78
Biofuels Fac.	136	2.5	17.0	65.2	0.79
Biofuels Fac.	159	2.6	17.8	72.4	0.80
BECON	182	1.6	49.7	48.5	0.49

Table 4.6—Refractory and insulation thicknesses of previous and present reactors

Reactor	Refractory thickness (cm)	Insulation Thickness (cm)
Biofuels Fac.	2.54	2.54
BECON	7.62	0.00

compared to the previous reactor. Sensitivity analysis has shown that the presence of external insulation has a moderately significant effect during steam cooling, and this may also be the case during the combustion phase.

Second, the additional refractory with the present reactor significantly increases the thermal mass of the wall, causing more sensible energy to be stored within the wall. A comparison of thermal mass of the walls of the reactors is shown in Table 4.7. From this comparison, it can be seen that an additional 117 kJ/K is stored in the wall of the present reactor as the refractory is heated during the combustion phase. While this additional thermal capacity would not affect a steady-state process to a significant degree, it is problematic for the dynamic ballasted gasification system. It is hypothesized that large quantities of thermal energy are transferred to and from the refractory during the combustion and pyrolysis phases. If the average temperature within the refractory fluctuated by 150 K during the operation of the cycle (the fluidized bed temperature fluctuates 250 K during this time), an additional 17.5 MJ would be stored within the refractory, requiring additional energy to be provided during the phase. There are currently no means of measuring the temperature of the refractory in the present reactor, and so a precise determination of the role this large thermal mass plays in the operation of the reactor cannot be quantified.

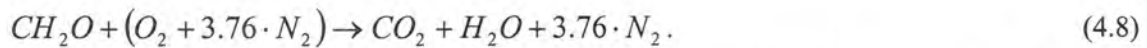
The char burnout period is critical to cycle behavior as it accomplishes two important tasks. First, it removes the char that accumulates within the bed during pyrolysis, and second, the oxidation of the char provides thermal energy to the bed. During the char burnout period carried out in previous testing, the bed was fluidized with air, but no biomass was fed to the reactor. Thus, the main product of this period was CO₂ as the char (C) reacted with oxygen in the air. The period continued until the char had been consumed. In the present study, air and biomass were fed to the reactor immediately following the conclusion of the pyrolysis phase. Because of the char present during the portion of this combustion phase, there was not enough air to combust all of the fuel within the reactor, and so the exhaust stream contained products of incomplete combustion. This can be seen in the graph of the chemical composition of Cycle 4 (see Figure 4.25). Significant amounts of carbon monoxide and hydrogen are present in the producer gas,

Table 4.7—Thermal mass of the walls of the previous and present reactors

Reactor	Refractory				Insulation				Total
	thick. (cm)	m (kg)	c _p (kJ/kg-K)	m*c _p (kJ/K)	thick. (cm)	m (kg)	c _p (kJ/kg-K)	m*c _p (kJ/K)	m*c _p (kJ/K)
Biofuels Fac.	2.54	56.6	0.92	52.1	2.54	3.7	1.05	3.9	55.0
BECON	7.62	187.6	0.92	172.6	0.00	0.0	1.05	0.0	172.6

and these products carry a certain amount of chemical exergy with them as they leave the reactor. In effect, the removal of this chemical exergy robs the fluidized bed of thermal energy, increasing the amount of biomass that must be combusted to raise the temperature of the bed.

The inlet temperature of steam has been found to be a significant factor in determining reactor behavior during pyrolysis (see Figure 4.7 and Figure 4.8), and it is reasonable to believe that inlet temperature of the air has a similar effect during the combustion phase. During previous testing, both the combustion air and steam were passed through a preheater, elevating air and steam temperatures to approximately 720 K (837°F). During present testing the combustion was not preheated, and the inlet temperature profiles are plotted with bed temperature profiles for both steam cooling and pyrolysis tests in Figure 4.29 and Figure 4.30, respectively. These graphs illustrate that the inlet temperature is below 400 K throughout the majority of the combustion phase. If stoichiometric combustion is considered, and the biomass is assumed to have the form CH_2O , the combustion equation can be written as:



According to a proximate analysis conducted for seed corn, the higher heating value, HHV , has a value of 17,300 kJ/kg. This value is defined based on the enthalpies of formation, but does not consider the sensible enthalpy of the reactants and products. If these sensible enthalpies are

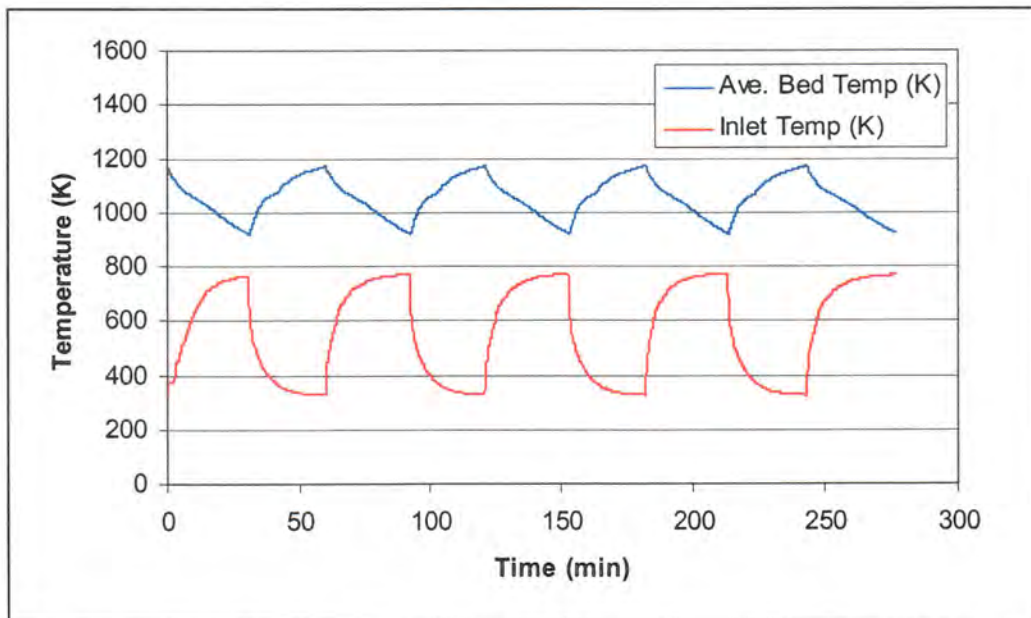


Figure 4.29—Average bed temperature and inlet temperature during steam cooling cycle

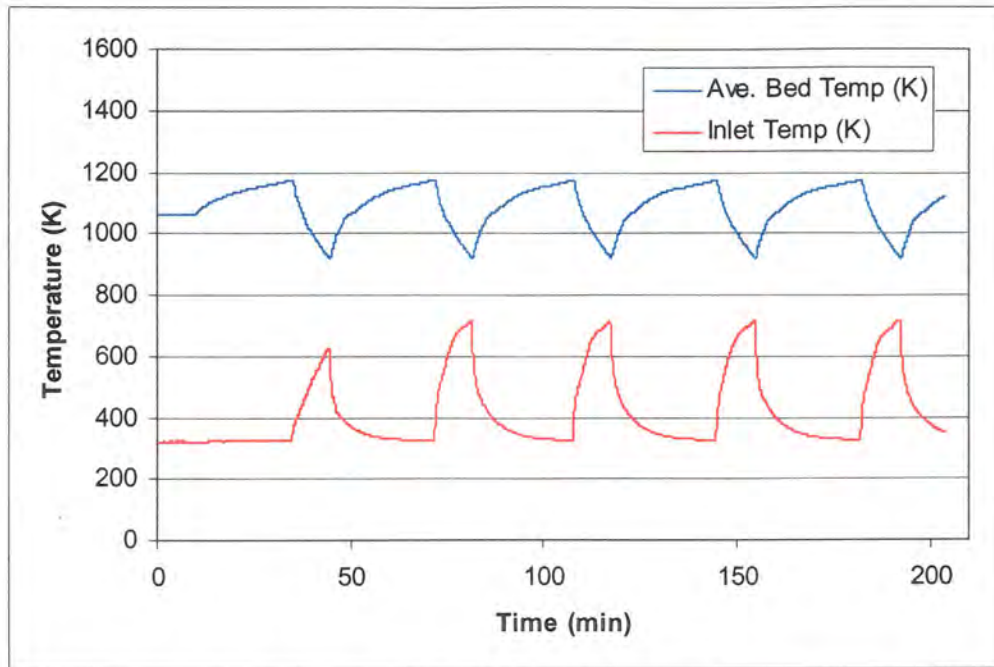


Figure 4.30—Average bed temperature and inlet temperature during ballasted gasification

considered, the enthalpy of the combustion reaction, Δh_{comb} , can be calculated and is considerably lower than the higher heating value, HHV , as a large amount of sensible energy leaves the reactor with the products of combustion. Rather than the higher heating value, it is the enthalpy of combustion that best describes the amount of energy released to raise the temperature of the fluidized bed. By examining the enthalpy of combustion for air inlet temperatures of 400 K and 720 K, it is clear that raising the inlet temperature increases the amount of energy released during the combustion process. It is assumed that the products of combustion are raised to the bed temperature. Thus, as the temperature of the bed increases, the enthalpy of combustion decreases due to the increased exit temperature of the products of combustion. A comparison of enthalpies of combustion throughout the process for two inlet air temperatures, 420 K and 720 K, is shown in Table 4.8.

Table 4.8—A comparison of enthalpy of combustion for varying inlet air temperatures

Bed Temp (K)	Δh_{comb} (kJ/kg of biomass)		% Diff.
	$T_{air,in} = 400$ K	$T_{air,in} = 720$ K	
922	10360	11900	+14.8
1000	10900	12440	+14.1
1100	11640	13180	+13.2
1172	12200	13740	+12.6

Based on the results of a sensitivity analysis of the purge gas flowrate (Section 4.2.2), this gas can also be a significant heat sink during the operation of the reactor. It is unclear, however, how considerable this sink is during the combustion process, when large amounts of thermal energy are introduced into the reactor.

There appear to be several factors that result in the lengthy combustion period observed in tests conducted on the BECON reactor. One of the most significant factors is the large thermal mass represented by the increased refractory within the reactor, but it is unlikely that this parameter can be drastically altered. Therefore, improvements to bed operation must focus on changes to parameters that can be effectively modified. The most effective means of shortening the combustion phase would be to preheat the air which fluidizes the bed and provides the oxidant for combustion. Conducting a char burnout phase would also better utilize the fuel present within the reactor and increase the fraction of fuel pyrolyzed. The period could be further reduced by wrapping the bed with external blanket insulation and decreasing the flowrate of the purge gas, although these would provide less substantial improvements in bed behavior than the other factors mentioned.

A more detailed analysis of the ballasted gasification cycle would be greatly facilitated by the closure of a mass balance around the system, and so an attempt was made to close such a balance. The most vital portion of this mass balance was the mass flowrates of the respective species within the producer gas. As mentioned previously, all nitrogen present in the producer gas is believed to be derived from the purge gas. Thus, it was hypothesized that the purge gas could be used as a “tracer” to determine the producer gas mass flowrates. As the Micro-GC provided composition on a molar basis, the ratio the mole fraction of a given species, x_i , to the mole fraction of nitrogen (N_2), x_{N_2} , would be equal to the ratio of the respective volumetric flowrates, \dot{V}_i and \dot{V}_{N_2} , according to the equation:

$$\frac{x_i}{x_{N_2}} = \frac{\dot{V}_i}{\dot{V}_{N_2}}. \quad (4.2)$$

However, uncertainty arose in the nitrogen flowrate through the reactor from two sources. The first source of uncertainty was due to the omission of a pressure gauge downstream of the rotameter used to measure the flow. Due to this, the pressure at the rotameter was uncertain, and correction calculations were unable to be performed. The second source of uncertainty was due to leaks in the herbaceous fuels feeding system. The leaks from this system have not been quantified, but they are thought to be significant. Because of these uncertainties, the nitrogen flowrate through the reactor could not be confidently quantified, and thus, this method was

unqualified to quantify the producer gas flowrate. Methods to properly quantify the other mass flowrates of the system, char, tar and water flowrates, were not employed, and thus, attempts to close a mass balance were unsuccessful.

In order to obtain a mass balance on the ballasted gasification cycle, a number of steps should be taken. The first of these steps would be to inject an alternate tracer gas into the stream. This tracer should be inert and be able to be detected by the Micro-GC. Argon would fit these requirements. If a fixed amount of the tracer were injected into the freeboard of the reactor, virtually all of it would exit with the producer gas through the exhaust ducting. As the tracer and the producer gas would pass through the first cyclone, the gases should be well mixed. Micro-GC measurements could then be collected for a number of cycles, and the argon content of the resulting producer gas could be used to determine total flowrates, similarly to Equation 4.2.

Excluding the producer gas, all mass should leave the reactor as char, tar or water. The char can be quantified by performing the following tasks: completing a char burnout period and weighing the cyclones barrels. Using the gas cart and Micro-GC data during combustion, carbon dioxide profiles can be obtained and the tracer gas can be used to establish the mass flowrate of carbon dioxide in the exhaust stream. This mass flowrate of carbon dioxide could be used to determine the mass of char, assumed to be composed solely of carbon (C), combusted during the period [42]. The change in barrel weight would provide an estimate of the char and flyash that elutriated from the fluidized bed during operation. It is assumed that very little char and flyash are produced during the combustion phase. The tar and water content of the gas can be determined according to the Guideline for Sampling and Analysis of Tar and Particles in Biomass Producer Gases [43], which employs an impinger train to capture these components.

Upon the closure of a mass balance, two significant tasks will be able to be achieved: the modeling of the pyrolysis phase of the ballasted gasification cycle and the calculation of a cold-gas efficiency of the process. With the closure of the mass balance, the composition and quantity of the producer gases will be known, and this empirical data will provide the basis to determine the rates at which the chemical processes absorb energy within the bed. The accuracy of the Receding Interface model predictions during the steam cooling tests indicate that the physical heat transfer processes of ballasted gasification are well-understood. Thus, once the chemical processes have been properly characterized, the model should accurately predict reactor behavior during the pyrolysis phase.

The cold gas efficiency is ratio of the total chemical exergy of the producer to the chemical exergy of the biomass fed to the reactor throughout the entire cycle. The chemical exergy of the producer gas can be calculated as the product of the total quantity of gas produced

and the average heating value of the gas. The chemical exergy of the biomass fed to the reactor is the product of the sum of biomass fed during the pyrolysis and combustion phase and the higher heating value of the biomass. In order to be considered an effective gasification system, the cold gas efficiency should exceed 60%.

5. CONCLUSIONS AND RECOMMENDATIONS FOR FUTURE STUDY

5.1 Conclusions

The development of practical hydrogen production methods would be a valuable step toward the emergence of a sustainable energy infrastructure based on fuel cell power. One viable method of generating hydrogen in the Midwestern United States is biomass gasification. One gasification concept, ballasted gasification, provides higher hydrogen contents and heating values than those of conventional gasification processes. However, ballasted gasification requires a source of energy to drive the endothermic pyrolysis reactions. One means of providing this energy is by inserting a thermal energy storage device within the reactor. This thermal storage device is termed a thermal ballast, as it stores heat during a combustion period and releases heat during pyrolysis.

A thermally-ballasted gasification cycle was operated successfully at the BECON Facility. Bed temperature profiles were obtained, and producer gas composition was characterized throughout the pyrolysis phase. Hydrogen contents as high as 31% were achieved on a dry, inert-free basis, with high levels of carbon monoxide and significant quantities of methane, acetylene, ethylene and ethane as well. Heating values of the producer gas were observed in excess of $16,000 \text{ kJ/m}^3$ (430 Btu/ft^3), with an average of $15,800 \text{ kJ/m}^3$ (424 Btu/ft^3) throughout the pyrolysis phase. Despite the successful production of a hydrogen-rich fuel gas, the current system suffered from a long combustion period. This lengthy period reduced system efficiency and was caused by multiple factors, including the large thermal mass of the internal refractory of the reactor and the relatively cold inlet temperature of the combustion air.

A previous mathematical model of the heat transfer processes which occur within the reactor was modified to account for the insulating effect of the solidifying phase-change material. This addition allowed the model to predict bed temperature profiles more accurately during the phase-change process without reducing accuracy during the remainder of the period. Once experimental data verified the accuracy of the model, the model was used to perform sensitivity analyses to determine the significance of certain parameters. The steam inlet temperature was found to be especially significant to the cooling process of the reactor, while the addition of phase-change material and the reduction of characteristic length of the ballast allowed the fluidized bed to operate in a more ideal manner.

Based on the results of the sensitivity analyses, two potential improvements to the design of the thermal ballast have been suggested. The first suggestion is the modification of the current tube-based ballast design by extending the tubes above the surface of the bed. Lengthening these tubes would increase the amount of phase-change material within the without compromising

fluidization dynamics or heat transfer processes. The second potential design attempts to reduce the characteristic length of the ballast, while retaining the same quantity of phase-change material within the bed. This design suffers from an inability to assure a well-mixed bed, but would potentially behave in a more ideal manner. It is believed that near-ideal operation of the thermal ballast will be required to create a potential for thermally-ballasted gasification to be successful in efficiently producing a high-quality fuel gas.

5.2 Recommendations for future study and process improvement

While some of the objectives of this research have been achieved, others will require additional experimentation and research. The enthalpy of pyrolysis and the cold gas efficiency of the system have not been determined. To obtain this information, the closure of a mass balance around the ballasted gasification system is of the utmost importance. As mentioned in Section 4.4, this balance could be achieved by completing the following:

- Argon should be injected into the freeboard of the reactor and used as tracer gas. This tracer will help quantify actual gas flowrates when detected with the Micro-GC.
- Char should be quantified by performing char burnout tests. With the CEM, a CO₂ profile could be obtained and integrated to determine the amount of char consumed during the burnout period. Elutriated char could be quantified by weighing the cyclone barrels before and after each test.
- Tar and water could be quantified by passing a slipstream of the producer gas through a series of impingers containing dichloromethane, as described in [38].

Additional work and research opportunities include:

- The development of catalytic tar cracking and water-gas shift processes to increase the hydrogen content of the producer gas. The producer gas contains significant amounts of carbon monoxide and hydrocarbons that could be converted into additional hydrogen.
- Operating additional ballasted gasification tests to obtain more Micro-GC data to confirm the present data and provide additional data points for species not quantified by the CEM's.
- Exploration of the source of the unexplained temperature plateau during the combustion phase. This phenomenon consistently appears as temperatures approach 1075 K (1475°F).

- Developing a method of cooling the feeding system that would eliminate the need for purge gas injected into the reactor. This would eliminate the dilution due to purge gas and allow a more representative analysis of the actual ballasted gasification behavior.
- Obtaining temperature data from the castable refractory of the reactor. This would provide insight into the heat transfer processes that occur between the fluidized bed and the refractory. A series of thermocouples at various depths within the refractory would be extremely valuable.
- The placement of additional phase-change material within the reactor to determine if predictions based on the sensitivity analysis are correct.
- Use experimental data acquired during pyrolysis as empirical data points to determine heat of reaction during the pyrolysis phase. This heat of pyrolysis will vary as the cooling period proceeds. The utilization of this data will improve model predictions during the pyrolysis phase of ballasted system.
- Developing a model of the combustion phase of the ballasted gasification cycle to predict heating times. This might offer additional insights into the lengthy combustion times seen during the present study.
- Developing of a graphical user interface to increase the amount of variables the user can control. This would reduce the time required to consider various parameters of the model by allowing the user to enter these parameters via dialog boxes.

**APPENDIX A: BALLASTED GASIFICATION (BIOFUELS FACILITY REACTOR)
MODEL CODE (C++)**

```
//-----

#include <vcl.h>
#include <math.h>
#include <iostream.h>
#include <fstream.h>
#include <conio.h>
#pragma hdrstop

//-----

// Declaration of global variables, arrays and functions

double T[25];      //node temperatures

double m[25];      //mass values for node points
double mSt1 = 1.0; //mass of steel in steel/ref node
double mRef = 1.0; //mass of ref in steel/ref mode
double mSt2 = 1.0; //mass of steel in steel/ins node
double mIns = 1.0; //mass of ins in steel/ins node

double cp[25];     //specific heat values for node points

double k[25];      //thermal conductivity for node points
long double r[25]; //distance from the center of reactor of each node point

double y[4][25];
double kVal[4][25];

bool ballast;
bool reaction;
double feedrate = 0.0;

double getInfo (); //obtains information from user

void initialTemps ();
void massCalc (double);
void cpCalc ();
double fluidSpecHeat (int, double);
void kCalc ();
void rCalc (double);

double RungeKutta (double);
void derivatives (int, double, double);
double hReacCalc (double, double);
double enthalpyCalc (int, double);
```

```
//-----
#pragma argsused
void main()
{
    double h = 0.1;      //step-size
    double t = 0.0;      //increment (time) counter
    double tf = 0.0;     //final value of counter
    double dx = 0.0254/7.0;

    //variables used in recording latent heat and tube modeling
    double latentQ = 0.0;
    double latentQTotal = 0.0;
    double mFus = 0.0;
    double volFus = 0.0;
    double hFusLiF = 1050000.0;
    double rhoLiFs = 2330.0;
    double solidHeight = 0.3357;

    tf = getInfo ();

    rCalc (dx);
    initialTemps ();
    massCalc (dx);
    cpCalc ();

    int printCounter = 0;

    ofstream outfile ("Z:\\ballast.dat");
    outfile << "t, t (min), T[0], T[1], T[2], T[3], T[4], T[5], T[6], T[7], "
        << " T[8], T[9], T[10], T[11], T[12], T[13]" <<endl<< "0, 0, ";
    for (int i=0; i<14; i++) outfile << T[i] << ", ";
    outfile << endl;

    do {

        //determine the specific heat of the bed (85% sand, 15% limestone)
        cp[1] = 0.85*(-1.563e-4*pow(T[1],2.0) + 0.5388*T[1] + 773.2) + 0.15*810;

        //determine the specific heat of the fluidizing steam
        // (based on average temperature of bed and steam)
        cp[19] = fluidSpecHeat(1,(T[1]+T[19])/2.0);

        //determine the specific heat of the purge gas
        // (based on average temperature of bed and steam)
        cp[20] = fluidSpecHeat(2,(T[1]+300.0)/2.0);

        //determine the thermal conductivity
        kCalc ();
    }
}
```

```

//RungeKutta (h) numerically integrates the temperature equations
latentQ = RungeKutta (h);
latentQTotal += latentQ;

//calculate the change in volume of solidified LiF
// and the change in radius of r[15]
mFus = -latentQ/hFusLiF;
volFus = mFus/rhoLiFs;

if ((pow(r[15],2.0)-(volFus/(solidHeight*M_PI))<0.0) r[15] = 0.0;
else r[15] = sqrt(pow(r[15],2.0)-(volFus/(solidHeight*M_PI)));

if (printCounter == 49) {
    outfile << t << " " << t/60.0 << " ";
    for (int i=0; i<16; i++) outfile << T[i] << " ";
    outfile << r[15] << " " << latentQ << " ";

    outfile << endl;
    printCounter = 0;
}
else printCounter++;

//increment the time
t += h;

} while (t < tf);

outfile.close();

cout << endl << latentQTotal << endl;
cout << endl << endl << "Calculations complete. Data file stored as "
    << "'ballast.dat' on Z: drive." << endl << "Press any key to "
    << "continue." << endl;
getch ();    //requires the header file 'conio.h'

return;
}

double getInfo ()
{
    double b;
    int monitor = 0;
    double timef;

    do {
        cout << "Is the gasifier ballasted?" << endl
            << "Please enter 0 for unballasted gasifier." << endl
            << "Please enter 1 for ballasted gasifier." << endl;

        cin >> b;

```

```

    if (fabs(b) < 0.0001) {
        ballast = false;
        monitor = 1;
    }
    else if (fabs(b)-1.0 < 0.0001) {
        ballast = true;
        monitor = 1;
    }
}
while (monitor == 0);

monitor = 0;

do {
    cout << endl << "Should pyrolysis chemistry be considered?" << endl
        << "Please enter 0 to not consider pyrolysis." << endl
        << "Please enter 1 to consider pyrolysis." << endl;

    cin >> b;
    if (fabs(b) < 0.0001) {
        reaction = false;
        monitor = 1;
    }
    else if (fabs(b)-1.0 < 0.0001) {
        reaction = true;
        cout << endl << "What is the biomass feedrate "
            << "(in kg/hr)?" << endl;
        cin >> feedrate;
        if (feedrate < 0.0) feedrate = 50.0;
        else if (feedrate > 200.0) feedrate = 200.0;
        monitor = 1;
    }
}
while (monitor == 0);

cout << endl << "How long (in seconds) should the simulation run?"
    << endl;
cin >> timef;

if (timef < 0.0) timef = 1.0;
else if (timef > 5000.0) timef = 4200.0;

return timef;
}

void rCalc (double deltax)
{
    r[0] = 1.0; //ambient temperature
    r[1] = 1.0;
}

```

```

for (int i=2; i<10; i++) r[i] = 9.0*0.0254 + (i-2)*deltax;
r[10] = r[9] + 0.00635;
r[11] = r[10] + 0.0127;
r[12] = r[11] + 0.0127;
r[13] = 0.0127;
r[14] = r[13] - 0.065*0.0254;
r[15] = r[14];

}

void initialTemps ()
{
    //all temperatures in K
    T[0] = 303.0; //ambient temperature
    T[1] = 1172.0;
    T[10] = 922.0;
    T[12] = 711.0;
    T[19] = 720.0; //steam inlet temperature (from RP's thesis)

    T[2] = T[1] - 30.0;
    T[9] = T[10];
    T[11] = T[12] + (T[10]-T[12])/2.0;

    for (int i=3; i<9; i++) T[i] = T[i-1] - ((T[2]-T[9])/(9.0-2.0));

    T[13] = T[1];
    T[14] = T[1];
}

void massCalc (double deltax)
{
    double rhoSt = 7854.0; //density of carbon steel (reactor shell)
    double rhoRef = 2403.0; //density of refractory (from RP's thesis)
    double rhoIns = 128.0; //density of insulating blanket (from RP's)
    double rhoSS = 8238.0; //density of ballast tube shell (SS 316)
    double bedH = 0.6; //bed height in meters. (0.6 m = 23.6")
    double tubeL = 24*0.0254; //length of ballast tube (24")

    m[0] = 1.0;
    if (ballast == true) m[1] = 150.0; //mass of bed = 150 kg for ballasted tests
    if (ballast == false) m[1] = 172.0; //mass of bed = 172 kg for unballasted
    // RP's thesis (p. 41)
    m[2] = rhoRef*M_PI*(pow((r[2]+deltax/2.0),2.0)-pow(r[2],2.0))*bedH;
    for (int i=3; i<9; i++) {
        m[i] = rhoRef*M_PI*(pow((r[i]+deltax/2.0),2.0)
            -pow((r[i]-deltax/2.0),2.0))*bedH;
    }
    mSt1 = rhoSt*M_PI*(pow((r[9]+0.00635/2.0),2.0)-pow(r[9],2.0))*bedH;
}

```

```

mRef=rhoRef*M_PI*(pow(r[9],2.0)-pow((r[9]-deltax/2.0),2.0))*bedH;
m[9] = mSt1 + mRef;
mSt2 = rhoSt*M_PI*(pow(r[10],2.0)-pow((r[10]-0.00635/2.0),2.0))*bedH;
mIns = rhoIns*M_PI*(pow((r[10]+0.0127/2.0),2.0)-pow(r[10],2.0))*bedH;
m[10] = mSt2 + mIns;
m[11] = rhoIns*M_PI*(pow((r[11]+0.0127/2.0),2.0)
                -pow(r[11]-0.0127/2.0,2.0))*bedH;
m[12] = rhoIns*M_PI*(pow(r[12],2.0)-pow(r[12]-0.0127/2.0,2.0))*bedH;
m[13] = rhoSS*M_PI*(pow(r[13],2.0)-pow(r[14],2.0))*tubeL;
m[14] = 0.3; // 0.3 kg of LiF per tube

```

```

}

```

```

void cpCalc ()

```

```

{

```

```

    double cpRef = 920.0;
    double cpIns = 1050.0;
    double cpSt = 1170.0; //from Incropera & DeWitt (T=1000 K)
    double cpSS = 600.0; //from Incropera & DeWitt (T=1000 K)
    double cpLiF = 2300.0; //cp attributed to LiF in RP's thesis

```

```

    for (int i=2; i<9; i++) cp[i] = cpRef;

```

```

    cp[9] = (mSt1*cpSt + mRef*cpRef)/(mSt1 + mRef);
    cp[10] = (mSt2*cpSt + mIns*cpIns)/(mSt2 + mIns);

```

```

    cp[11] = cpIns;
    cp[12] = cpIns;
    cp[13] = cpSS;
    cp[14] = cpLiF;

```

```

}

```

```

double fluidSpecHeat (int fluidNo, double fTemp)

```

```

{

```

```

    double cv = 0.0;
    double kcp[8];
    double beta = 0.0;
    double specHeat = 0.0;

```

```

    switch (fluidNo) {

```

```

        case 1: // specific heat for steam (atmos. pressure, ideal gas)

```

```

            kcp[0] = 46000.0;
            kcp[1] = 1011.249;
            kcp[2] = 0.83893;
            kcp[3] = -2.19989e-4;
            kcp[4] = 2.46619e-7;
            kcp[5] = -9.7047e-11;

```

```

cv = 0.0;
for (int i=0;i<6;i++) {
    cv += kcp[i]*pow(fTemp, i-1);
}
specHeat = cv + 8314.0/18.02;
break;

```

```

case 2: // specific heat for N2
kcp[0] = -218203.473713518;
kcp[1] = 10157.3580096247;
kcp[2] = -165.50472165724;
kcp[3] = 743.17599919043;
kcp[4] = -5.14605623546025e-3;
kcp[5] = 5.18347156760489e-6;
kcp[6] = -1.05922170493616e-9;
kcp[7] = 298.389393363817;
beta = 3353.4061;

```

```

cv = 0.0;
for (int i=0;i<7;i++) {
    cv += kcp[i]*pow(fTemp, i-3);
}
cv += kcp[7] * exp(beta/fTemp)
    * pow((beta/fTemp)/(exp(beta/fTemp)-1),2.0);
specHeat = cv + 8314.0/28.0;
break;

```

```

default:
    cout << "Error in fluid specific heat calculation."
        << endl;
}

```

```

return specHeat;
}

```

```

void kCalc ()
{
    double kLiF = 4.0;    //thermal conductivity of Lithium Fluoride
    for (int i=2; i<9; i++) {
        k[i] = 2.166E-04*T[i] + 1.222;
    }
    k[9] = 74.59-0.04445*((T[9]+T[10])/2.0);
    for (int i=10;i<12;i++) {
        k[i] = 1.875e-7*pow(((T[i]+T[i+1])/2.0),2.0)
            - 1.09875e-4*((T[i]+T[i+1])/2.0) + 0.0775216875;
    }
    k[13] = 8.968 + 0.0153*((T[13] + T[14])/2.0);
    k[14] = kLiF;
}

```

```

double RungeKutta (double step)
{
    double latQ = 0.0;
    double step2 = step/2.0;
    double hReac = 0.0;

    if (reaction == false) hReac = 0.0;
    if (reaction == true) hReac = hReacCalc (T[1], T[19]);

    //set current values as y[0][i]
    for (int i=0; i<20; i++) y[0][i] = T[i];

    //acquire RungeKutta k1 values
    // k1 values correspond to k[0][i] array
    derivatives (0, step, hReac);

    //determine first predictions of f[i] at the midpoint of the the step
    for (int i=0; i<20; i++) y[1][i] = T[i] + step2*kVal[0][i];

    //acquire RungeKutta k2 values
    // k2 values correspond to k[1][i] array
    derivatives (1, step, hReac);

    //determine second predictions of f[i] at the midpoint of the the step
    for (int i=0; i<20; i++) y[2][i] = T[i] + step2*kVal[1][i];

    //acquire RungeKutta k3 values
    // k3 values correspond to k[2][i] array
    derivatives (2, step, hReac);

    //determine third predictions of f[i] at the endpoint of the the step
    for (int i=0; i<20; i++) y[3][i] = T[i] + step*kVal[2][i];

    //acquire RungeKutta k4 values
    // k4 values correspond to k[3][i] array
    derivatives (3, step, hReac);

    for (int i=0; i<20; i++) {
        T[i] = T[i] + (step/6.0*(kVal[0][i] + 2.0*(kVal[1][i]
            + kVal[2][i]) + kVal[3][i]));
    }

    latQ = step/6.0*(kVal[0][20] + 2.0*(kVal[1][20] + kVal[2][20]) + kVal[3][20]);

    return latQ;
}

```

```

double hReacCalc (double Tbed, double Tgas)

```

```

{
double hR = 0.0;

double molesH = 1.98; //formula for corn = CH(1.98)O(0.97)
double molesC = 1.00;

double hGas = 0.0;
double reacH = 0.0;
double reacHf = 0.0;
double prodH = 0.0;
double prodHf = 0.0;

double molWt[11] = {2.016, 16.04, 28.01, 44.01, 26.04, 28.05,
                    30.07, 14.23, 15.37, 18.01, 29.54};
//molecular weights of major constituents (kg/mol)
// 0 = H2
// 1 = CH4
// 2 = CO
// 3 = CO2
// 4 = C2H2
// 5 = C2H4
// 6 = C2H6
// 7 = tar (modeled as CH(2.2))
// 8 = char, C(s)
// 9 = water
// 10 = fuel (corn CH(1.98)O(0.97))

double gasComp[11] = {0.1881, 0.0740, 0.2800, 0.1314, 0.0036, 0.0373,
                     0.0036, 0.1260, 0.3001, 0.4270, 1.000};
// gas composition of major constituents (kmol/kmol fuel)
// same numbering scheme as molWt

double heatForm[11] = {0.0, -74850.0, -110530.0, -393520.0, 226731.0,
                      52167.0, -84700.0, 0.0, 0.0, -241820.0, 0.0};
// heats of formation for major constituents (kJ/kmol)
// same numbering scheme as molWt

double enthalpy[11] = {0.0, 0.0, 0.0, 0.0, 0.0, 0.0,
                      0.0, 0.0, 0.0, 0.0, 0.0};
// enthalpies of major constituents (kJ/kmol)

// calculate the heat of formation of fuel (from T. Reed's
// "Biomass Gasification Principles and Technology")
heatForm[10] = (-1473.0*(molesH/molesC) - 149.0)*2.326*molWt[10];

// calculate the heat of formation of tar (Reed's formula)
heatForm[7] = (-1473*(2.2/1.0) - 149)*2.326*molWt[7];

// calculate the enthalpies of relevant species
for (int i=0; i<10; i++) enthalpy[i] = enthalpyCalc (i, Tbed);

```

```

reacH = 0.0; // not considering water as reactant, enthalpy of fuel unknown
reacHf = heatForm[10];

```

```

// calculate the enthalpy of the products
for (int i=0; i<10; i++) prodH += gasComp[i]*enthalpy[i];
for (int i=0; i<10; i++) prodHf += gasComp[i]*heatForm[i];
hR = (-1000/molWt[10])*(prodH + prodHf - reacH - reacHf);

```

```

return hR;

```

```

}

```

```

double enthalpyCalc (int j, double t)

```

```

{

```

```

    double h = 0.0;

```

```

    switch (j) {

```

```

        case 0:

```

```

            //H2

```

```

            h = 0.001663*pow(t,2.0) + 26.978*t - 7959.2;

```

```

            break;

```

```

        case 1:

```

```

            //CH4

```

```

            h = 0.01994*pow(t,2.0) + 31.024*t - 12789.0;

```

```

            break;

```

```

        case 2:

```

```

            //CO

```

```

            h = 0.00283*pow(t,2.0) + 27.387*t - 8526.4;

```

```

            break;

```

```

        case 3:

```

```

            //CO2

```

```

            h = 0.006287*pow(t,2.0) + 41.315*t - 14210.0;

```

```

            break;

```

```

        case 4:

```

```

            //C2H2

```

```

            h = 0.01044*pow(t,2.0) + 47.023*t - 16256.0;

```

```

            break;

```

```

        case 5:

```

```

            //C2H4

```

```

            h = 0.022515*pow(t,2.0) + 47.712*t - 19572.0;

```

```

            break;

```

```

        case 6:

```

```

            //C2H6

```

```

            h = 0.03228*pow(t,2.0) + 56.554*t - 12729.0;

```

```

            break;

```

```

        case 7:

```

```

            //CH2

```

```

            h = 0.0071592*pow(t,2.0) + 31.042*t - 10093.0;

```

```

            break;

```

```

        case 8:

```

```

            //C(s)

```

```

        h = 0.003858*pow(t,2.0) + 13.573*t - 5643.0;
        break;
    case 9:
        //H2O
        h = 0.0061523*pow(t,2.0) + 28.980*t + 34865.0;
        break;
    default:
        h = 0.0;
}

return h;
}

void derivatives (int j, double h, double heatReac)
{
    double mdotPurge = 3.7*(101.325/((8.314/28.0)*298.15))*(0.02832/60);
        //convert 3.7 scfm to kg/s
    double tPurge = 300.0; // temperature of the purge gas (300 K)

    //External heat transfer coefficients
    double hFree = 5.0;
    double hRadExt = 14.8;
    double hExt = hFree + hRadExt;

    //Internal heat transfer coefficients
    double hConv = 305.0;
    double sigma = 5.67e-8;
    double epsBed = 0.85;
    double epsSurface = 0.35;
    double epsEff = 1.0/((1.0/epsSurface) + (1.0/epsBed) - 1.0);
    double hRadWall = sigma*epsEff*(pow(T[1],4.0)-pow(T[2],4.0))/(T[1]-T[2]);
    double hWall = hConv + hRadWall;
    double hRadTube;
    if (T[1] == T[13]) hRadTube = 0.0;
    else hRadTube = sigma*epsEff*(pow(T[1],4.0)-pow(T[13],4.0))/(T[1]-T[13]);
    double hTube = hConv + hRadTube;

    double bedH = 0.6; //actual bed height in gasifier (RP altered height in
        //program to obtain better agreement with experimental data)
    double mdotFluid; // mass flowrate of fluidizing media
    double nTubes = 48.0; // number of ballast tubes in bed
    double tubeL = 24*0.0254; //tube length = 24"
    double effTubeL = 0.343; //effective length of the ballast tube
        // (0.343 m = 13.5")
    double mBiomass = feedrate/3600.0;

    // k values correspond to the value of the derivative evaluated
    // according to initial temperatures and predictor temperatures

```

```
// kVal[j][20] corresponds to latent heat calculation from the tube
```

```
//UNBALLASTED, NO PYROLYSIS EQUATIONS
```

```
if (ballast == false) {
```

```
    mdotFluid = 107.0/3600.0;
```

```
    kVal[j][1] = (1.0/(m[1]*cp[1]))*
        (mdotFluid*cp[19]*(y[j][19]-y[j][1])
        + mdotPurge*cp[20]*(tPurge-y[j][1])
        + 2.0*M_PI*r[2]*bedH*hWall*(y[j][2]-y[j][1])
        + mBiomass*heatReac);
```

```
    kVal[j][2] = (1.0/(m[2]*cp[2]))*
        (2.0*M_PI*r[2]*bedH*hWall*(y[j][1]-y[j][2])
        + 2.0*M_PI*k[2]*bedH/log(r[3]/r[2])*(y[j][3]-y[j][2]));
    for (int i=3; i<12; i++) kVal[j][i] = (1.0/(m[i]*cp[i]))*
        (2.0*M_PI*k[i-1]*bedH/log(r[i]/r[i-1])*(y[j][i-1]-y[j][i])
        + 2.0*M_PI*k[i]*bedH/log(r[i+1]/r[i])*(y[j][i+1]-y[j][i]));
    kVal[j][12] = (1.0/(m[12]*cp[12]))*
        (2.0*M_PI*k[11]*bedH/log(r[12]/r[11])*(y[j][11]-y[j][12])
        + 2.0*M_PI*r[12]*bedH*hExt*(y[j][0]-y[j][12]));
    kVal[j][20] = 0.0;
```

```
}
```

```
if (ballast == true) {
```

```
    mdotFluid = 90.3/3600.0;
```

```
    kVal[j][1] = (1.0/(m[1]*cp[1]))*
        (mdotFluid*cp[19]*(y[j][19]-y[j][1])
        + mdotPurge*cp[20]*(tPurge-y[j][1])
        + 2.0*M_PI*r[2]*bedH*hWall*(y[j][2]-y[j][1])
        + nTubes*2.0*M_PI*r[13]*tubeL*hTube*(y[j][13]-y[j][1])
        + mBiomass*heatReac);
```

```
    kVal[j][2] = (1.0/(m[2]*cp[2]))*
        (2.0*M_PI*r[2]*bedH*hWall*(y[j][1]-y[j][2])
        + 2.0*M_PI*k[2]*bedH/log(r[3]/r[2])*(y[j][3]-y[j][2]));
    for (int i=3; i<12; i++) kVal[j][i] = (1.0/(m[i]*cp[i]))*
        (2.0*M_PI*k[i-1]*bedH/log(r[i]/r[i-1])*(y[j][i-1]-y[j][i])
        + 2.0*M_PI*k[i]*bedH/log(r[i+1]/r[i])*(y[j][i+1]-y[j][i]));
    kVal[j][12] = (1.0/(m[12]*cp[12]))*
        (2.0*M_PI*k[11]*bedH/log(r[12]/r[11])*(y[j][11]-y[j][12])
        + 2.0*M_PI*r[12]*bedH*hExt*(y[j][0]-y[j][12]));
```

```
    if (T[14] > 1123.0 && r[15] > 0.0) {
        kVal[j][13] = (1.0/(m[13]*cp[13]))*
            (2.0*M_PI*r[13]*tubeL*hTube*(y[j][1]-y[j][13])
            + 2.0*M_PI*k[13]*effTubeL/log(r[13]/r[14])*
            (y[j][14]-y[j][13]));
```

```

kVal[j][14] = (1.0/(m[14]*cp[14]))*(2.0*M_PI*k[13]*effTubeL
    /log(r[13]/r[14])*(y[j][13]-y[j][14]));
kVal[j][20] = 0.0;
}
else if (T[14] <= 1123.0 && r[15] > 0.0) {
kVal[j][13] = (1.0/(m[13]*cp[13]))*
    (2.0*M_PI*r[13]*tubeL*hTube*(y[j][1]-y[j][13])
    + 2.0*M_PI*effTubeL*(y[j][14]-y[j][13])
    /((log(r[13]/r[14])/k[13]+log(r[14]/r[15])/k[14]));
kVal[j][14] = 0.0;
T[14] = 1123.0;
kVal[j][20] = 2.0*M_PI*effTubeL*(y[j][13]-y[j][14])
    /((log(r[13]/r[14])/k[13]+log(r[14]/r[15])/k[14]));
}
else {
kVal[j][13] = (1.0/(m[13]*cp[13]))*
    (2.0*M_PI*r[13]*tubeL*hTube*(y[j][1]-y[j][13])
    + 2.0*M_PI*effTubeL*(y[j][14]-y[j][13])
    /((log(r[13]/r[14])/k[13]+log(r[14]/(r[15]+0.00001))/k[14]));
kVal[j][14] = (1.0/(m[14]*cp[14]))*(2.0*M_PI*effTubeL*(y[j][13]-y[j][14])
    /((log(r[13]/r[14])/k[13]+log(r[14]/(r[15]+0.00001))/k[14]));
kVal[j][20] = 0.0;
}
}
}
}
//-----

```

APPENDIX B: CALCULATION OF POTENTIAL INTERFERENCE OF HYDROGEN ANALYZER BY GAS COMPONENTS

From a fax from Nova Analytical Systems regarding the H2 analyzer:

"Thermal conductivity sensor output for various gases

The thermal conductivity sensor output was set to provide 0-100 mV for 0-100% hydrogen. The ambient temperature was 25C and the R.H. was 35%. All gases used have low dewpoints (~ -40C). Flow rate is 1 SCFH.

Gases:

100% N2	=	+ 0.00 mV
100% H2	=	+ 100.00 mV
100% CH4	=	+ 11.71 mV
100% CO	=	- 1.24 mV
100% CO2	=	- 10.06 mV
100% O2	=	+ 1.21 mV "

(I've omitted certain gases that didn't seem relevant, such as SF6, Helium, Argon and natural gas.)

So, during combustion, when we see 80% N2, ~16% CO2 and ~2% O2, we would expect to see an offset of:

$$\text{offset, comb} = 0.80*(0.00) + 0.16*(-10.06) + 0.02*(1.21) = -1.58 \text{ mV}$$

We actually see an offset of -1.4 mV during testing, so this appears to make sense.

During gasification, we see ~20% N2, 25-29% CO, 13-20% CO2, 7-10% CH4 and negligible oxygen. These are the ranges seen on the gas composition through the pyrolysis phase of the ballasted cycle. CO, CO2 and O2 were determined through the gas cart and corroborated by the microGC. CH4 and N2 were determined solely by the microGC. CO and CO2 have negative interferences, while CH4 has a positive interference. So if CO and CO2 were at their maximum, while CH4 was at its minimum (which is not likely in reality), the offset would be:

$$\text{offset, gas} = 0.29*(-1.24) + 0.20*(-10.06) + 0.07*(11.71) = -1.55 \text{ mV}$$

If CO and CO2 were at their minimum, however, while CH4 was at its maximum, the offset would be:

$$\text{offset, gas} = 0.25*(-1.24) + 0.13*(-10.06) + 0.10*(11.71) = -0.45 \text{ mV}$$

During gasification, when there are more carbon species present, there is slightly less interference, as the negative CO and CO2 interference is mitigated to some degree by the positive interference of CH4. The offset error during combustion is obvious—as we see an offset of -1.4 when we expect 0.0. The offset error during gasification is less obvious, assuming a hydrogen content of ~20% (dry, with N2), the relative error is approximately 2.5% to 7.5%.

APPENDIX C: PREDICTION OF INTERNAL PRESSURE WITHIN A LiF BALLAST TUBE [8]

As lithium fluoride changes phase from solid to liquid, it undergoes a significant change in volume, increasing the pressure within the ballast tube. The following calculations determine the factor of safety of the tube design.

Current ballast tube design

Tube Geometry:

Length,	L	$= 61.0 \text{ cm}$	(24.0 in.)
Outer diameter,	D_o	$= 2.54 \text{ cm}$	(1.0 in.)
Wall thickness,	t	$= 0.165 \text{ cm}$	(0.065 in.)
Inner diameter,	D_i	$= OD - 2*t$	
		$D_i = 2.21 \text{ cm}$	(0.87 in.)

$$\text{Inner tube volume, } V_{\text{free}} = \pi * L * (D_i^2 / 4)$$

$$V_{\text{free}} = 233.99 \text{ cm}^3 \quad (14.279 \text{ in}^3)$$

Lithium fluoride (LiF) properties:

$$\text{Mass of LiF/tube, } m_{\text{LiF}} = 0.3 \text{ kg} \quad (0.661 \text{ lb})$$

$$\begin{aligned} \text{Density, solid, } \rho_s &= 2330 \text{ kg/m}^3 \\ \text{Volume, solid, } V_s &= m_{\text{LiF}} / \rho_s \\ V_s &= 128.8 \text{ cm}^3 \quad (7.86 \text{ in}^3) \end{aligned}$$

$$\begin{aligned} \text{Density, liquid, } \rho_l &= 1800 \text{ kg/m}^3 \\ \text{Volume, liquid, } V_l &= m_{\text{LiF}} / \rho_s \\ V_l &= 166.7 \text{ cm}^3 \quad (10.17 \text{ in}^3) \end{aligned}$$

Pressure exerted by LiF:

State a:

$$T_a = 293 \text{ K}$$

$$P_a = 1 \text{ atm}$$

$$\text{Initial volume of air pocket, } V_a = V_{\text{free}} - V_s = 105.0 \text{ cm}^3 \quad (6.41 \text{ in}^3)$$

State b:

$$T_b = 1200 \text{ K}^*$$

$$\text{Initial volume of air pocket, } V_a = V_{\text{free}} - V_l = 67.13 \text{ cm}^3 \quad (4.10 \text{ in}^3)$$

*Maximum temperature (LiF melts at 1122 K)

$$\text{Employing the ideal gas law: } (p_a V_a) / (T_a R) = (p_b V_b) / (T_b R)$$

$$p_b = 6.408 \text{ atm} = 649.3 \text{ kPa} = 94.2 \text{ psi}$$

Evaluate failure possibilities:

Strength of tubing, $S = 48000 \text{ kPa}$ ($S = 6962 \text{ psi}$)

Wall failure:

For thin walled cylinders the hoop stress, σ , is given by the formula, $\sigma = pr/t$, where p is the internal pressure, r is the internal radius and t is the wall thickness.

$$\sigma = p_b \cdot (D_i/2)/t, \quad \sigma = 4346 \text{ kPa} \quad (\sigma = 630 \text{ psi})$$

Factor of safety for the wall, $SF = S/\sigma = 11.046$

Weld failure:

Pressure exerted on the top of the tube will be transmitted to the weld, possibly causing failure.

Area exposed to internal pressure, $A_i = \pi \cdot (D_i^2/4)$

Force applied to tube cap, $F = p_b \cdot A_i = 249 \text{ Newtons} = 56.0 \text{ lbf}$

Weld area, $A_{\text{weld}} = \pi \cdot (D_o^2/4) - A_i$

Stress in the weld, $\sigma = F/A_{\text{weld}} = 2022 \text{ kPa}$ ($\sigma = 293 \text{ psi}$)

Factor safety in the weld, $SF = S/\sigma = 23.742$

Lengthened ballast tube design ($L = 106.7 \text{ cm}$ with 0.7 kg of LiF per tube)**Tube Geometry:**

Length,	$L = 106.7 \text{ cm}$	(42.0 in.)
Outer diameter,	$D_o = 2.54 \text{ cm}$	(1.0 in.)
Wall thickness,	$t = 0.165 \text{ cm}$	(0.065 in.)
Inner diameter,	$D_i = OD - 2 \cdot t$	
	$D_i = 2.21 \text{ cm}$	(0.87 in.)

Inner tube volume, $V_{\text{free}} = \pi \cdot L \cdot (D_i^2/4)$

$$V_{\text{free}} = 409.5 \text{ cm}^3 \quad (24.99 \text{ in}^3)$$

Lithium fluoride (LiF) properties:

Mass of LiF/tube, $m_{\text{LiF}} = 0.7 \text{ kg}$ (1.54 lb)

Density, solid, $\rho_s = 2330 \text{ kg/m}^3$

Volume, solid, $V_s = m_{\text{LiF}}/\rho_s$
 $V_s = 300.4 \text{ cm}^3$ (18.33 in³)

$$\begin{aligned}
 \text{Density, liquid, } \rho_1 &= 1800 \text{ kg/m}^3 \\
 \text{Volume, liquid, } V_1 &= m_{\text{LiF}}/\rho_1 \\
 V_1 &= 388.9 \text{ cm}^3 \quad (23.73 \text{ in}^3)
 \end{aligned}$$

Pressure exerted by LiF:

State a:

$$T_a = 293 \text{ K}$$

$$P_a = 1 \text{ atm}$$

$$\text{Initial volume of air pocket, } V_a = V_{\text{free}} - V_s = 109.1 \text{ cm}^3 \quad (6.66 \text{ in}^3)$$

State b:

$$T_b = 1200 \text{ K}^*$$

$$\text{Initial volume of air pocket, } V_a = V_{\text{free}} - V_1 = 20.58 \text{ cm}^3 \quad (1.26 \text{ in}^3)$$

*Maximum temperature (LiF melts at 1122 K)

$$\text{Employing the ideal gas law: } (p_a V_a)/(T_a R) = (p_b V_b)/(T_b R)$$

$$p_b = 21.71 \text{ atm} = 2200 \text{ kPa} = 319.1 \text{ psi}$$

Evaluate failure possibilities:

$$\text{Strength of tubing, } S = 48000 \text{ kPa} \quad (S = 6962 \text{ psi})$$

Wall failure:

For thin walled cylinders the hoop stress, σ , is given by the formula, $\sigma = pr/t$, where p is the internal pressure, r is the internal radius and t is the wall thickness.

$$\sigma = p_b * (D_i/2)/t, \quad \sigma = 14733 \text{ kPa} \quad (\sigma = 2137 \text{ psi})$$

$$\text{Factor of safety for the wall, } SF = S/\sigma = 3.258$$

Weld failure:

Pressure exerted on the top of the tube will be transmitted to the weld, possibly causing failure.

$$\text{Area exposed to internal pressure, } A_i = \pi * (D_i^2/4)$$

$$\text{Force applied to tube cap, } F = p_b * A_i = 844 \text{ Newtons} = 189.8 \text{ lbf}$$

$$\text{Weld area, } A_{\text{weld}} = \pi * (D_o^2/4) - A_i$$

$$\text{Stress in the weld, } \sigma = F/A_{\text{weld}} = 6856 \text{ kPa} \quad (\sigma = 994 \text{ psi})$$

$$\text{Factor safety in the weld, } SF = S/\sigma = 7.001$$

REFERENCES

1. Wheldon, A.E.; Gregory, C.E. Energy, electricity and the environment. IEE Proceedings-A 140 (1):2-7.
2. El-Hinnawi, Essam E. The Environmental Impacts of Production and Use of Energy. Shannon, Ireland: Irish Elsevier Printers Limited, 1981.
3. Union of Concerned Scientists. Briefing: The Hidden Costs of Fossil Fuels. Located online at: <http://www.ucsusa.org/energy/brief.hidden.html>.
4. Deffeyes, Kenneth S. Hubbert's Peak: the impending world oil shortage. Princeton, NJ: Princeton University Press, 2001.
5. Energy Information Administration. The International Energy Outlook 2002. Located online at: <http://www.eia.doe.gov/oiaf/ieo/appendixes.html>.
6. Arnason, Bragi; Sigfusson, Thorsteinn I. Iceland—a future hydrogen economy. International Journal of Hydrogen Energy 25:389-394.
7. Oatley, Jeffrey A. 1994. Development of a Latent-Heat-Ballasted Biomass Gasifier. MS Thesis. Iowa State University, Ames, IA.
8. Pletka, Ryan Joseph. 1998. Latent Heat Ballasted Biomass Gasification. MS Thesis. Iowa State University, Ames, IA.
9. Hoffman, Peter. Tomorrow's Energy: hydrogen, fuel cells and the prospects for a cleaner planet. Cambridge, MA: The MIT Press, 2001.
10. Larminie, James; Dicks, Andrew. Fuel Cell Systems Explained. Chichester, England: John Wiley & Sons, Ltd., 2000.
11. Spath, Pamela L.; Mann, Margaret K. 2001. Life cycle assessment of hydrogen production via natural gas steam reforming. NREL/TP-570-27637.

12. Ahmed, S.; Krumpelt, M. 2001. Hydrogen from hydrocarbon fuels for fuel cells. *Int. J. Hydrogen Energy* 26: 291-301.
13. Gaudernack and Lynum (1998). Hydrogen from natural gas without release of CO₂ to the atmosphere. *Int. J. Hydrogen Energy* 23(12): 1087-1093.
14. Ohta, T.; Veziroglu, T.N. Hydrogen production using solar radiation. *Int. J. Hydrogen Energy* 1: 255-263.
15. Dutton, A.G., et al. (2000). Experience in the design, sizing, economics, and implementation of autonomous wind-powered hydrogen production systems. *Int. J. Hydrogen Energy* 25: 705-722.
16. Padin, J.; Veziroglu, T.N.; Shahin, A. Hybrid solar high-temperature hydrogen production system. *Int. J. Hydrogen Energy* 25: 295-317.
17. Funk and Reinstrom (1966). Energy Requirements in the Production of Hydrogen from Water. *I&EC Process Design and Development* 5(3): 336-342.
18. LC Brown, et al. High efficiency generation of hydrogen fuel cells using nuclear power. General Atomics Report GA-A23451.
19. Besenbruch, Gottfried (1982). The General Atomic Sulfur-Iodine Thermochemical Water-Splitting Process. *American Chemical Society, Div. Pet. Chemistry, Prepr.* 271, p. 48-53.
20. GE Besenbruch, et al. (2000). High efficiency generation of hydrogen fuels using nuclear power. General Atomics GA-A23510.
21. Das, Debabrata; Veziroglu, T. Nejat. Hydrogen production by biological processes: a survey of literature. *Int. J. Hydrogen Energy* 26: 13-28.

22. Wolfrum, Edward J.; Watt, Andrew S. Bioreactor design studies for a novel hydrogen-producing bacterium. Proceedings of the 2001 DOE Hydrogen Program Review.
23. Milne, Thomas A.; Elam, Carolyn C.; Evans, Robert J. 2002. Hydrogen from biomass: state of the art and research challenges. A report for the International Energy Agency Agreement on the production and utilization of hydrogen task 16, Hydrogen from carbon-containing materials. IEA/H2/TR-02/001. Available online at: www.eren.doe.gov/hydrogen/iea/iea_publications.html.
24. Turn, S.; et al. 1998. An experimental investigation of hydrogen production from biomass gasification. *Int. J. Hydrogen Energy* 23(8): 641-648.
25. Rapagna, S.; Jand, N.; Foscolo, P.U. 1998. Catalytic gasification of biomass to produce hydrogen rich gas. *Int. J. Hydrogen Energy* 23(7): 551-557.
26. Brown, R.C. 1994. The potential for biomass production and conversion in Iowa. Iowa State University Technical Report. ISU-ERI-Ames 95009.
27. Reed, T. editor. 1981. Biomass gasification: principles and technology. Park Ridge, NJ: Noyes Data Corp.
28. Graham, R.; Bergougnou, M.; Mok, L.; De Lass, H. 1985. Fast pyrolysis of biomass using solid heat carriers. In *Fundamentals of Thermochemical Biomass Conversion*. Eds. Overend, R.; Milne, T.; Mudge, L. London: Elsevier Applied Science Publishers LTD.
29. FBT, Inc. 1994. Fluidized bed combustion and gasification: a guide for waste generators. Prepared for the Southeastern Regional Biomass Energy Program.
30. Bain, R.L.; Overend, R.P.; Craig, K.R. 1996. Biomass-fired power generation. Presented at Biomass Usage for Utility and Industrial Power. Snowbird, UT, April 29-May 3, 1996, Engineering Foundation, NY, NY.

31. Gas-Lite Manufacturing Company. 2002. "The history of the gas light," located online at: www.gaslite.com/history.html
32. Heritage Research Center, Ltd. 2002. "Manufactured Gas—the Genie's Legacy," located online at: www.heritageresearch.com/manufactured_gas_A.htm.
33. Hatheway, Allen W. 2002. "History and Chronology of Manufactured Gas," located online at: www.hatheway.net/history.htm.
34. Kaupp, A. 1984. Gasification of Rice Hulls. Braunschweig, Germany: Friedr. Vieweg & Sohn Verlagsgesellschaft mbH.
35. Reed, T.; Das, D. 1988. Handbook of Biomass Downdraft Gasifier Engine Systems. Golden, CO: Biomass Energy Foundation Press.
36. Mansour, M.; Durai-Swamy, K.; Voelker, G. 1995. MTCI/ThermoChem steam reforming process for biomass. In Proceedings of the Second Biomass Conference of the Americas. Golden, CO: National Renewable Energy Laboratory.
37. Paisley, M.A.; Anson, D. 1998. Biomass gasification for gas turbine-based power generation. *Journal of Engineering for Gas Turbines and Power, Transactions of the ASME*, 120(2): 284-288.
38. Paisley, M.A., et al. 1999. Commercial demonstration of the Battelle/FERCO biomass gasification process: startup and initial operating experience. Proceedings of the Fourth Biomass Conference of the Americas, Oakland, CA, pp. 1061-1066.
39. Chase, Malcolm. 1998. JANAF Thermochemical Tables.
40. Incropera, Frank P.; DeWitt, David P. 1996. Fundamentals of Heat and Mass Transfer, 4th ed. New York: John Wiley & Sons.
41. Varlamov, G.B., et al. 1989. Thermophysical and optical properties of fluoride crystals and melts. *High Temperatures—High Pressures* 21: 647-656.

42. Christofedes, Nearchos J.; Brown, Robert C. 1993. Coal burning properties determined from CO₂ profiles. *Combustion and Flame* 94: 449-461.
43. Neeft, J.P.A. et al. 2002. Guideline for sampling and analysis of tar and particles in biomass producer gases. Version 3.1. Energy project EEN5-1999-00507 (Tar protocol).